

# The Impacts of Cement Dust Deposits on Soil Available Micronutrients

Buba M. Wufem  
Chemistry Department  
Plateau State University  
Nigeria Yola, Nigeria

A. Q. Ibrahim  
Chemistry Department  
Police Academy  
Nigeria Wudil,  
Kano Nigeria

Humphrey M. Maina  
Chemistry Department  
Federal University of Technology  
Bokkos, Nigeria

Nangbes, J. Gungsat  
Chemistry Department  
Plateau State University  
Bokkos, Nigeria

Nvau, J. Barnabas  
Chemistry Department  
Plateau State University  
Nigeria Yola, Nigeria

---

**ABSTRACT:** The impact of cement dust deposits on soils micronutrient around Ashaka cement factory, Nigeria was evaluated by determining available micronutrient elements in 68 soil samples and some crop plant stalks using acid extraction and atomic absorption spectrophotometric methods. Soil samples collected in a radius of 6Km from a 0 – 30cm depth and analysed indicated mean concentrations of 215.30gKg<sup>-1</sup> Fe, 7.96 gKg<sup>-1</sup> Zn, 0.33 gKg<sup>-1</sup> Cu, 80.79 gKg<sup>-1</sup> Mn, 2.05 gKg<sup>-1</sup> Ni, and 26.91 gKg<sup>-1</sup> Co. The concentration of each element in the soil varies in a decreasing order with increasing distance away from the cement factory and generally occurring above background levels (Zn, Mn, Ni). The metals in the crop plants were higher than normal levels with sorghum concentrating more metals than millet, suggesting a reflection of the soil metal concentrations and this might be due to the presence of available mobile elements and the slightly acidic nature of the soil outside the factory.

**Keywords:** Micronutrients, cement dust, Contamination, Crops

---

## 1. INTRODUCTION

Dust has been attributed to be one of the major causes of pollution in the environment. It is emitted into the atmosphere from natural and anthropogenic sources such as volcanic eruption, dust storms, road traffic, industrial processes, etc and soil serves as a major sink for its deposition [1,2]. Dust consists of solid matter in such a fine state of subdivision that the particles are small enough to be raised and carried by wind [3]. As a result of its fine particle size it travels over long distances and the total suspended particulate matter in the atmosphere is thus increased. Often industrial processes produce particulate emissions whose depositions may be accompanied with potential impacts caused to human and animal health, vegetations and soil [2]. The emissions of particulate matter to air by cement industries have constituted a major problem in most third world countries mostly due to economic constraints [4]. Recently, efforts have been put in place in most cement industries to suppress dust emission; nevertheless, past activities of cement industries have left farmlands in bad conditions. The main environmental pollutants generated by the company are dust and noise and these could cause dust laden air, cracking of walls of structures as well as soil and water polluted by dust to an extent that farming may be unprofitable [5]. The effects of cement dust on crop seedling emergence, concentration of hexoses in scot spine, radial growth of spruce stands have been documented [6,7,8]. The dust was reported to reduce the uptake of heavy metals in sludge soil by corn [9] (. Cement dust may contain

heavy metals and other chemical compounds that may include F, Mg, Pb, Zn, Cu, Be, H<sub>2</sub>SO<sub>4</sub>, and HCl [10,11,12]. Metals are considered very important to man and plants but some could be highly toxic and can be a source of pollution. Recently, Cu, Ni, and Zn were listed among metals that cause pollution [13] and these may pose risk and hazards to humans and ecosystem through ingestion or contact, food chain, drinking of contaminated ground or surface water, etc. Micronutrient elements (Fe, Cu, Zn, Mo, Mn, Co) are made up of mostly heavy metals of the transition groups that are essential to man, animal and plant nutrition. Heavy metals occur naturally in the soil environment from pedogenic processes of weathering of parent materials at levels that are regarded as trace i.e < 1000mgkg<sup>-1</sup> and is rarely toxic [14,15]. Due to the disturbance and nature's occurring geochemical cycle of metals by man most soils accumulate heavy metals above background levels high enough to cause risks to human health, plants, animals, ecosystems, or other media [16]. Fe, Cu, Zn, Co, and Mn are required for normal growth and metabolism of plants but may be toxic at high concentrations [17,18]. Heavy metals uptake by plants and successive accumulation in human tissues and biomagnifications through food chain causes both human health and environmental concerns [19]. The absorption of heavy metals by plant roots is one of the main ways they enter the food chain and their accumulation in plant tissues depends upon temperature, moisture, organic matter, pH, nutrient availability and plant species [20,21,22]. Moreover the efficiency of different plants in absorbing heavy metals is evaluated by either plant uptake or soil to plant transfer factors

of the metals [21]. The extent of effects of toxic metals on biological and biochemical properties of soil can be influenced by organic matter, clay contents and pH [23], nevertheless, toxic metals in the soil can severely inhibit the biodegradation of organic contaminants [24]. This work was aimed at assessing the influence of cement dust deposits on plant available Iron, Zinc, Manganese, copper, Nickel and Cobalt in cultivated soils around a cement factory.

## 2 EXPERIMENTALS

### 2.1 The study Area

Ashaka Cement Company was established in 1976 with an installed capacity of 500,000 MT [25] to meet the needs of construction works in the Northeastern part of Nigeria. It lies between longitude  $10^{\circ} 45'N$  and  $11^{\circ} 00'N$  and latitude  $11^{\circ} 15'E$  and  $11^{\circ} 30'E$  and is located in the Northern part of Gombe State, Nigeria. The area is cultivated with maize, millet, sorghum beans and groundnut being the most widely planted. Prior to now, a significant amount of dust from the factory was deposited on farmlands, homes and water bodies including the River Gongola that cuts across the area.

### 2.2 Sample Collection

Soil sample was collected from cultivated farmlands around the cement factory covering an area of about 112 Km<sup>2</sup> starting from the factory fence to 6km radius. Soils from 0-30cm depths were sampled at every 2Km distance. Stalks and leaves of millet and Sorghum were also collected at every soil sampled points.

### 2.3 Sample Treatment

Soil and plant samples were dried at 105°C in an oven until constant weight was obtained. Soil sample was ground and sieved through a 2mm screen plastic sieve. The plant sample was washed before drying at 105°C and ground in a ceramic mortar before being stored in plastic bottles.

### 2.4 Reagents and Chemicals

All analyses were performed with Analar grade chemicals and distilled water through out, unless otherwise stated.

### 2.5 pH Determination

pH of soil was determined using Philips pH-meter, model PW 9418 after shaking 5g of the soil with 5cm<sup>3</sup> of water.

### 2.6 Metal Extraction

A mixture of 1g soil and 10cm<sup>3</sup> of 0.1M HCl was shaken for 1hr on a mechanical shaker and the supernatant solution filtered using whatman filter paper No. 44 into a 100cm<sup>3</sup> volumetric flask. (It was repeated twice). The filtrate was made up to 100cm<sup>3</sup> mark with distilled water.

### 2.7 Digestion of plant crops

Ground crop leaves and stalks were weighed (0.5g) into a digestion tube and 100cm<sup>3</sup> of mixture of concentrated nitric acid and perchloric acid (2:1 v/v) was added. The tube was heated at 150°C in a digestion block and later increased to 230°C until the solution became clear. The temperature was reduced to 150°C and 10cm<sup>3</sup> hydrochloric acid was added and heated again for 30 minute before cooling. The content was then transferred quantitatively into a 100cm<sup>3</sup> volumetric flask and made to mark with water before filtering into plastic bottles. (It was repeated twice).

### 2.8 Metal Analysis

The filtrate obtained was analysed for Zn, Cu, Ni, Mn, Fe and Co using a Buck Scientific Atomic Absorption Spectrophotometer model 210 VGP. Air-Acetylene (8:6) flame and hollow cathode lamps for the respective elements were used at their various wavelengths. Calibration standards were obtained by preparing 100µg/cm<sup>3</sup> stock solution of the nitrate salts of the metals and the stock solution diluted to obtain working standards. Triplicate analyses were carried out for each sample.

## 3 RESULTS AND DISCUSSION

The overall mean available metals in cultivated soils as acid extractable metals are shown in Table 1 for 0-30cm.

**Table 1: Mean Available Concentration of Micronutrient Metals in Cultivated Soils (0-30cm) around Ashaka Cement Factory**

Metals	No. of Samples	Concentration (g/Kg)	Standard Deviation	Standard Range (g/Kg)
Fe	62	215.30	228.05	2– 960.10
Zn	62	7.96	5.71	0.00 – 27.76
Cu	62	0.33	0.18	0.09 – 0.95
Mn	62	80.79	32.2	1.40 – 311.43
Ni	62	2.05	3.31	0.00 – 33.95
Co	62	26.91	24.33	0.60 – 100.72

The mean available acid extractable micronutrient metal concentrations in cultivated soils with respect to distance from factory are shown in Table 2, while the overall mean micronutrient metal concentrations in plant crops commonly grown around the cement factory are provided in Table 3. The

concentration factors for the various micronutrient metals for millet and Sorghum were obtained by dividing the plant metal concentrations by the soil metal concentrations and their results are shown in Tables 4 and 5 respectively.

**Table 2: Mean Micronutrient Metal Concentrations (g/Kg) and pH in Cultivated Soils (0 – 30cm) at Distances from Factory**

Distance (Km)	pH	Metals					
		Fe	Zn	Cu	Mn	Ni	Co
0	7.57	316.5	9.86	0.40	108.12	3.35	32.02
2	6.76	272.9	8.59	0.32	65.02	1.82	30.36
4	6.38	116.8	7.50	0.30	45.56	1.51	26.16
6	6.27	95.35	5.05	0.29	52.53	1.13	13.84

**Table 3: Average Concentrations of Micronutrient Metals (g/kg<sup>-1</sup>) in Millet and Sorghum at Factory**

Metals	Millet		Sorghum	
	Conc	Range	Conc	Range
Fe	44.38	15.94 – 149.31	64.35	16.63 – 149.31
Zn	4.11	1.79 – 7.97	10.10	2.17 – 146.83
Cu	35.00	0.09 – 56.0	32.50	0.15 – 49.3
Mn	667.00	48.00 – 1497.9	190.5	34.00 – 363.46
Ni	5.30	1.98 – 11.95	6.05	1.89 – 9.90
Co	11.34	2.01 – 79.86	50.90	2.00 – 139.61

**Table 4: Mean Concentration Factors for Micronutrient Metals in Soil and Millet with Distance.**

Distance (Km)	pH	Metals					
		Fe	Zn	Cu	Mn	Ni	Co
0	7.57	0.191	0.425	0.125	0.032	2.069	0.288
2	6.76	0.128	0.430	0.094	0.097	2.918	0.298
4	6.38	0.299	0.589	0.100	0.059	3.027	0.288
6	6.27	0.424	1.346	0.103	0.144	6.708	0.465

**Table 5: Mean Concentration Factors for Micronutrient Metals in Soil and Sorghum with Distance**

Distance (Km)	pH	Metals					
		Fe	Zn	Cu	Mn	Ni	Co
0	7.57	0.207	20.892	0.100	0.191	3.701	0.191
2	6.76	0.215	19.569	0.094	0.181	5.319	0.137
4	6.38	0.752	34.800	0.133	0.395	11.371	0.201
6	6.27	0.452	26.000	0.069	0.196	9.354	0.321

It has been suggested [26] that concentrations of plant total metals do not adequately reflect the degree of absorption by plants. The extractable metal contents, a more direct indication of the availability of the absorbed metals and the possibility of re-mobilization have been reported [27] not to be a true mirror of plant available metals. Trace element uptake by roots are influenced by both soil and plant factors such as source and chemical form of elements in soil, pH, organic matter, plant species, etc. [28]. Interaction between elements occurring at the root surface and within the plant can affect uptake, as well as translocation and toxicity [29].

### 3.1 Iron in Crop Plants

The mean iron contents of millet and Sorghum are  $44.38\text{gkg}^{-1}$  and  $64.35\text{gkg}^{-1}$  with concentrations varying over wide ranges,  $15.94\text{--}149.31\text{gkg}^{-1}$  and  $16.63\text{--}149.31\text{gkg}^{-1}$  respectively (Table 3). These values are higher than the normal composition of Fe  $150\mu\text{gg}^{-1}$  in plants [30]. These agree with many findings as reported by Voutsas et al. [28] that elevated levels of metals in soils lead to increased plant uptake. Concentration factors for iron from soil to millet and sorghum are given in tables 4 and 5. The factors for the millet and Sorghum for iron are not significantly different and this suggests similar soil factors that control iron absorption in both millet and sorghum crop plants. However, the high absorption of iron at the 4Km distance must have been due to the long iron residence in solution form as a result of the river that cuts through the eastern part of the study area.

### 3.2 Zinc in Crop Plants

The mean zinc concentration in millet and Sorghum are  $4.11\text{gkg}^{-1}$  and  $10.10\text{gkg}^{-1}$  respectively (Table 3). These plant crops have wide distribution of Zinc ranging from  $1.79\text{--}7.97\text{gkg}^{-1}$  and  $2.17\text{--}146.83\text{gkg}^{-1}$  for millet and sorghum respectively. The zinc levels in the crops appear higher than the normal zinc levels in plants [30]. Sorghum showed higher performance for zinc absorption than millet. The zinc levels are too high to be of very much concern as it posed serious potential hazard to the environment. The high level agrees with the report by other researchers that plants growing in a polluted environment can accumulate trace elements at high concentrations that could cause serious risk to human health when plant based food stuff are consumed [31,32,33,34]. Zinc has been reported to be more phytotoxic than other commonly occurring metals with serious implications for human health [35, 36, 37, 38]. Larsen et al. and Harrison and Chirgawi [37, 38] have shown a relationship between atmospheric elements deposition and elevated element concentrations in plants and top soils especially in cities and in the vicinity of emitting factories. Atmospheric elements are deposited on plant surfaces by rain and dust with the airborne sub-micro particles filtered out on plant surfaces. This constitutes a substantial, but unknown, contribution to the atmospheric supply and the large-

scale sustained exposure of soil to both wet and dry deposition of trace elements constituting the indirect effect of air pollutants through the soil [28].

### 3.3 Copper in Crop Plants

Millet and Sorghum mean copper concentrations are  $35.00\text{gkg}^{-1}$  and  $32.50\text{gkg}^{-1}$  with a range of  $0.09\text{--}56.00$  and  $0.15\text{--}49.30\text{gkg}^{-1}$  respectively (Table 3). These levels are higher than the normal mean plant concentrations of  $10\mu\text{gg}^{-1}$  [30]. The concentration factors (Tables 4 and 5) indicated the extractable metals to be less absorbed even though it is supposed to represent an estimate of the plant available levels. However, it has been found that soil metal content does not necessarily mirror the plant metal bioavailability [27]. Copper has been associated with important potential pollutants [39]. Its mobility seems not to be influenced by pH, from soil to plants. The relatively high copper concentration of crop plants suggests that the soils upon which they were grown were contaminated. This spelled danger for the community residing in the vicinity of the factory.

### 3.4 Manganese in Crop Plants

Manganese concentrations in Millet and Sorghum vary over a wide range,  $48.00\text{--}1497.9\text{gkg}^{-1}$  and  $34.00\text{--}363.46\text{gkg}^{-1}$  with mean concentration of  $667.00\text{gkg}^{-1}$  and  $190.50\text{gkg}^{-1}$  respectively (Table 3). The absorption of Manganese by sorghum is less than that by Millet. Normal plant manganese has been put at  $200\mu\text{gg}^{-1}$  [30], which is far less than the Manganese levels found at minimum concentrations in plants. The high absorption reflects the level of contamination of the soils and there seems to be no clear pattern in the absorption of the metals in both plants with changing distances (Tables 4 and 5).

### 3.5 Nickel in Crop Plants

Millet and Sorghum were found to contain mean concentration of nickel of  $5.30\text{gkg}^{-1}$  and  $6.05\text{gkg}^{-1}$  respectively. The distribution of nickel in the plant crops analysed ranges from  $1.98\text{--}11.95\text{gkg}^{-1}$  and  $1.89\text{--}9.90\text{gkg}^{-1}$  for millet and sorghum respectively (Table 3). The average nickel in plants is  $1.5\mu\text{gg}^{-1}$  [30], suggesting nickel in the plant crops studied to be higher than normal. The concentration factors (Tables 4 and 5) increase with distance. The factors are greater than one at each sample point, which is an indication of high mobility from the soil to the plant crops. This means that millet and sorghum grown on this soil stand the possibility of accumulating nickel to a level that it can be dangerous to man. The change in the factor in both millets and sorghum with distance suggests that pH must have played a strong influence on the metal mobility. Metal contamination is often accompanied by high soil acidity [40]. High acidity has been known to increase metal solubility and mobility [41, 42]. It is likely that increased solubility of

nickel led to its increased availability and plant uptake, which may accentuate its toxicity.

### 3.6 Cobalt in Crop Plants

Normal plant content of cobalt is  $0.2\mu\text{gg}^{-1}$  [30], however, millet and sorghum analysed from this study area recorded  $11.34\text{gkg}^{-1}$  and  $50.90\text{gkg}^{-1}$  with wide ranges of  $2.01 - 79.86\text{gkg}^{-1}$  and  $2.00-139.61\text{gkg}^{-1}$  respectively (Table 3). These values are higher than the normal average as such it calls for concern. The concentration factors (Tables 4 and 5) showed that despite the high metal levels in plant crops, there is between 60-90% still unabsorbed in the soil. The likelihood of Cobalt going into the food chain is high; moreover, it has been classified among highly toxic and relatively accessible elements.

### 3.7 Effect of pH on Plant available metals

The mean soil pH was found to be  $6.76 \pm 0.86$  with a wide range of 4.7-9.84. This shows that the pH is slightly acidic even though some samples were strongly acidic. The observed pH is similar to those earlier reported for Savanna soils [43]. Young [44] has reported earlier that most savanna soils are acidic. The pH values suggest that a wide variety of crops can be grown on the soils. Soil acidity is caused by the removal of basic elements through leaching and crop uptake, organic matter decomposition, acid rain, nitrification of ammonium nitrogen, and by natural soil forming processes [45]. Cement factory emissions when they settle on soil could alter soil pH. In another work around a cement factory in turkey, dust emission was reported to have a pH of 6.5 – 8.6 [46]. This is similar to the pH range obtained in this work. The acidic pH values obtained here may have been due to the partial neutralization of the soil by high acidic gas emissions that may have been produced at the plant despite the alkaline cement dust. This was observed by Aslan and Boybay [46] in a work they did in the vicinity of a cement factory. This notwithstanding, the pH decreases with distance away from the factory, while the factory fence soil recorded slight alkalinity (Table II).

The fate and transport of a metal in soil depends significantly on the chemical form and speciation of the metal [47]. The mobility of metals may be hindered by reactions that cause metals to be absorbed or precipitated or chemistry that tends to keep metals associated with the solid phase and prevents them from dissolving. These mechanisms can retard the movement of metals and also provide a long term source of metal contaminants [48]. Metals undergo similar reactions but, the extent and nature of these reactions vary under particular conditions. The degree of sorption of several metal cations and anions onto iron oxide has been shown to be a function of pH for a particular electrolyte composition [49].

Micronutrient cations are mostly soluble and available under acidic conditions. In fact, under acid conditions the concentration of one or more of these elements often is sufficiently high to be toxic to common plants. Low pH increases metal availability since the hydrogen ion has a higher affinity for negative charge on the colloids, thus competing with the metal ions for these sites thereby releasing the metal. The metals become less available as the soil becomes alkaline. Increasing soil acidity induces loss of exchangeable base cations (K, Mg and Ca) [52]. The relationships between the

ratios of acid extractable crop metal to soil metal and soil pH (1:1 H<sub>2</sub>O) is given in Figs 9 – 20. The relationship was obtained by plotting the concentration factors against pH for all the metals hence, the influence of pH on the available metals is very glaring suggesting decreasing ratios of crop to soil metals with increasing pH.

In millets, the metals were mostly absorbed at  $\text{pH} < 6.5$  with the exception of copper (Figs 1 – 6). The absorption of the metals at this pH decreases in the order  $\text{Ni} > \text{Zn} > \text{Co} > \text{Fe} > \text{Mn} > \text{Cu}$ . At pH above 6.7, the absorption seems to rise steadily for Fe and Cu while for Zn the absorption decreases with increasing pH from slightly below pH 6.5. The affinity of Cu for humates increases as pH increases [51]. Copper mobility is decreased by Sorption to mineral surfaces.  $\text{Cu}^{2+}$  sorbs strongly to mineral surfaces over a wide range of pH values [52]. Zinc is one of the most mobile heavy metals in surface and ground waters because it is present as soluble compounds at neutral and acidic pH values. At higher pH values, zinc can form carbonate and hydroxide complexes which control precipitates under reducing conditions and in highly polluted systems when it is present at very high concentrations, and may co-precipitate with hydrous oxides of iron or manganese [27]. Sorption of zinc increases as pH increases and salinity decreases [51]. It has been reported that in calcareous soil of pH above 8.2, increasing  $\text{CO}_2$  increased carbonate ions, depressed  $\text{Ca}^{2+}$  activity and allowed  $\text{Zn}^{2+}$  to be held by chelating agent [53, 54]. Norvell observed that zinc concentrations are relatively high in acidic soil solution and  $\text{Zn}^{2+}$  competes very effectively with  $\text{Al}^{3+}$  and  $\text{Fe}^{3+}$  for chelating agents but at pH 7 the concentration of  $\text{Zn}^{2+}$  is much lower and it competes less effectively with  $\text{Ca}^{2+}$ . Zinc has been found to become mobile below pH 6 and pH 5 respectively [55] and decreased soil pH causes shift from organically complexed forms of metals to the free ionic form [56].

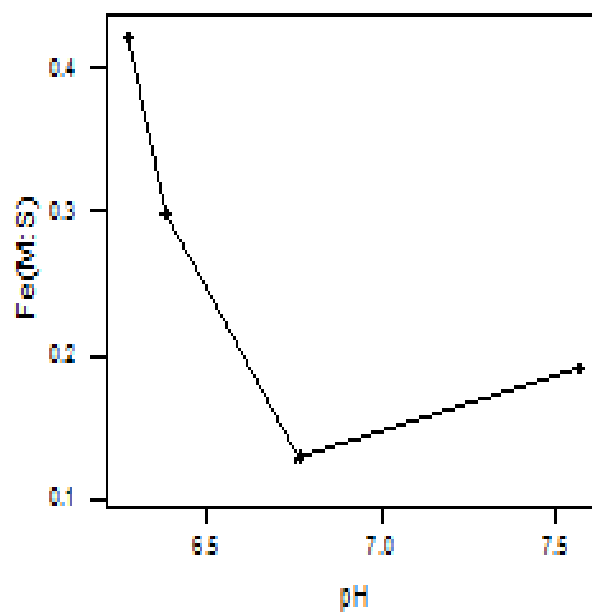


Fig. 1: Relationship of millet/soil iron ratios and soil pH  
(water/soil, 1:1)

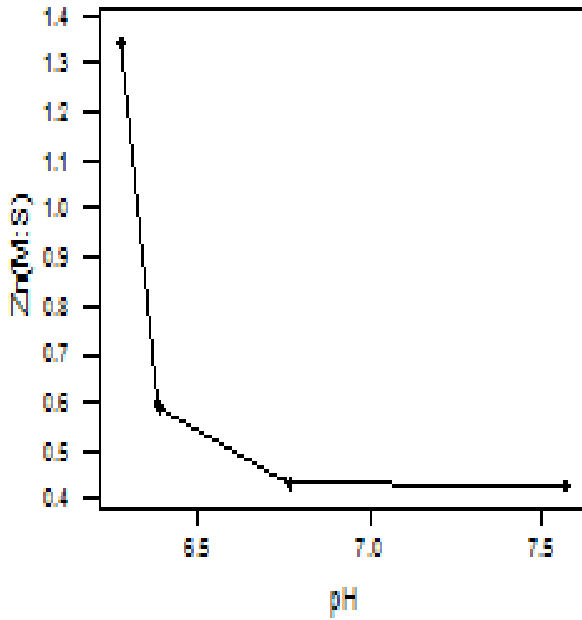


Fig. 2: Relationship of millet/soil zinc ratios and soil pH  
(water/soil, 1:1)

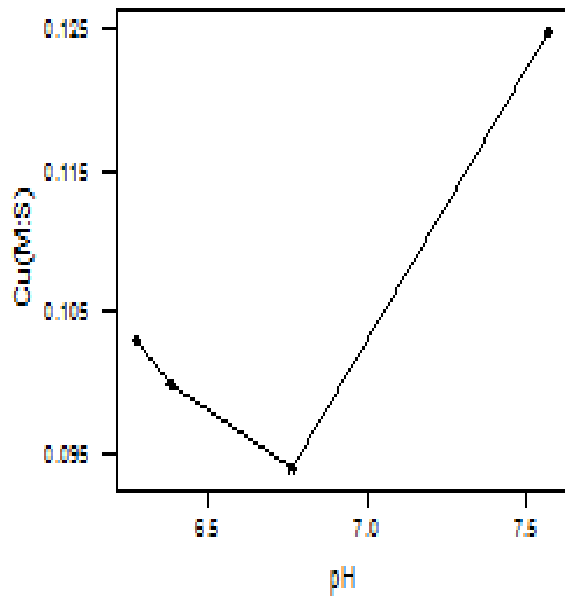


Fig. 3: Relationship of millet/soil copper ratios and soil pH  
(water/soil, 1:1)

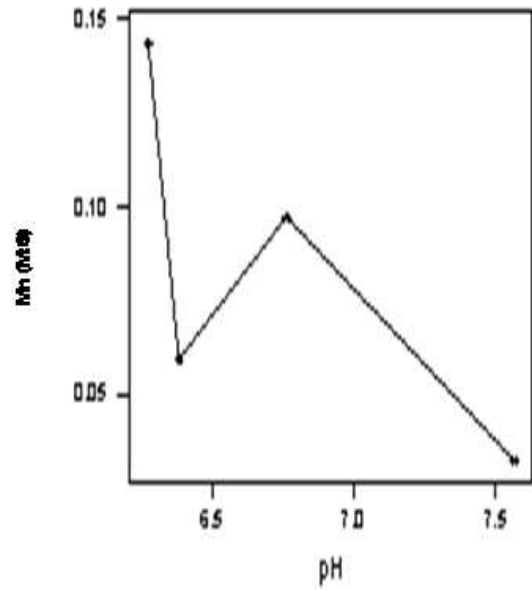


Fig 4. Relationship of Millet/Soil manganese Ratios

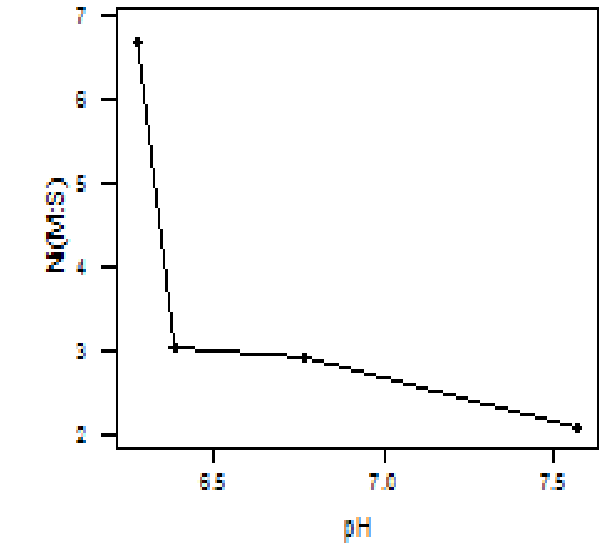
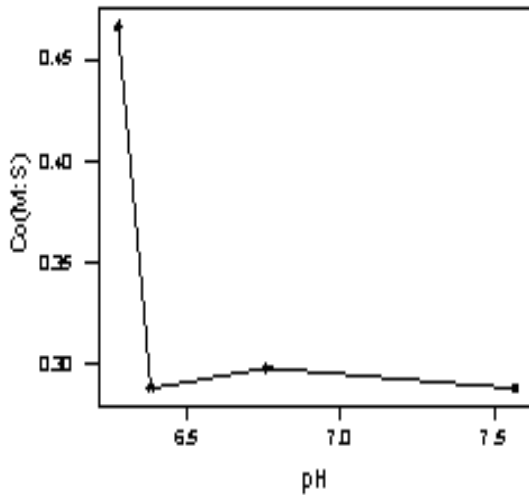
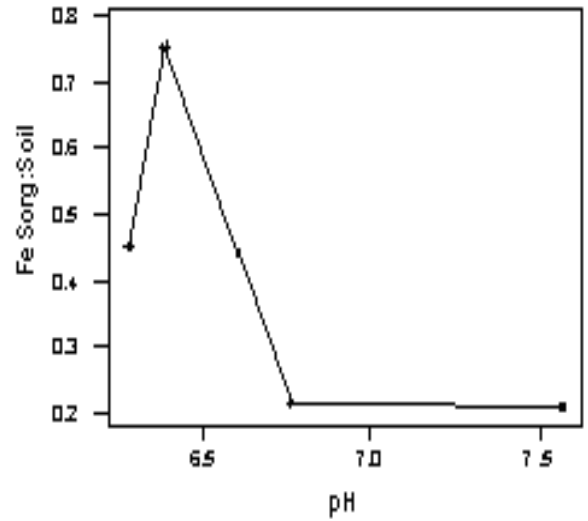


Fig. 5: Relationship of millet/soil nickel ratios and soil pH  
(water/soil, 1:1)



**Fig. 6 Relationship of millet/soil cobalt ratios and soil pH (water, 1:1)**

The Sorghum and soil metal levels do not follow the same pattern for all the metals considered. The Sorghum metal/soil metal ratio plots against pH (Figs 7-12) show higher ratios at low pH for all the metals. At pH less than 6.3 cobalt records its highest ratio which decreases as the pH increases. The trend is such that Fe, Zn, Cu, Mn and Ni Sorghum/soil ratios rise steadily to their highest concentrations above pH 6.3, but fall as the pH increases beyond this pH. Sorghum seems to concentrate maximum metals at pH a little below 6.5 with the exception of Cu. These indicate that availability of metals to plants is critical at pH 6 – 6.5. At pH above 6.5, metal availability is decreased. It has been noted that soil acidification is known to increase the solubility and mobility of metals [41,42]. It is likely that increased solubility of metal leads to increased availability and plant uptake thus accentuating metal toxicity [57]. The absorption of the metals by sorghum decreases in the order Zn>Ni>Fe>Co>Mn>Cu. This order indicates that sorghum shows more preference for Zn than Ni as compared to millet, which shows more preference for Ni than Zn.



**Fig. 7: Relationship of sorghum/soil iron ratios and soil pH (water/soil, 1:1)**

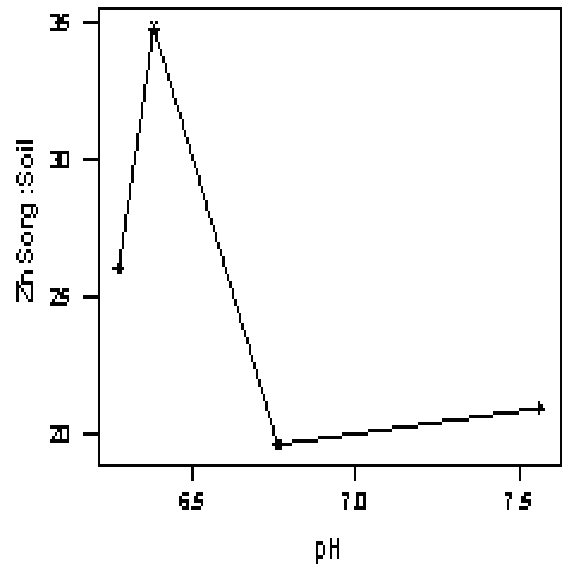


**Fig. 8: Relationship of sorghum/soil zinc ratios and soil pH (water/soil, 1:1)**

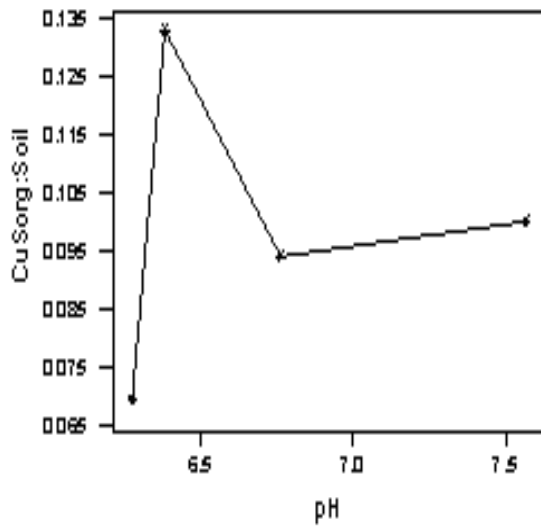


Fig. 9: Relationship of sorghum/soil copper ratios and soil pH (water/soil, 1:1)

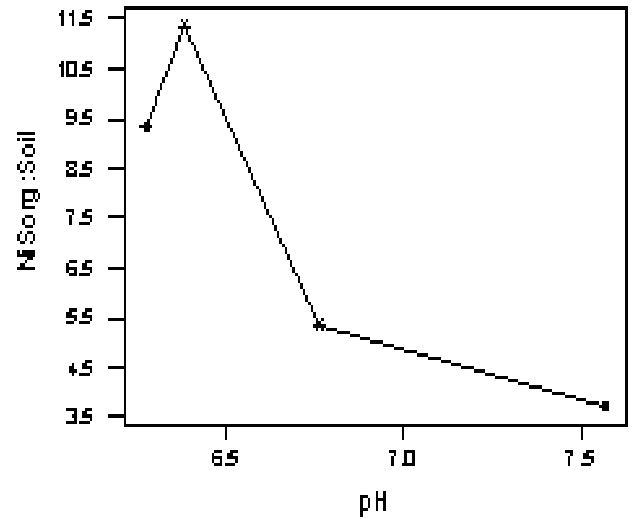


Fig. 11: Relationship of sorghum/soil nickel ratios and soil pH (water/soil, 1:1)

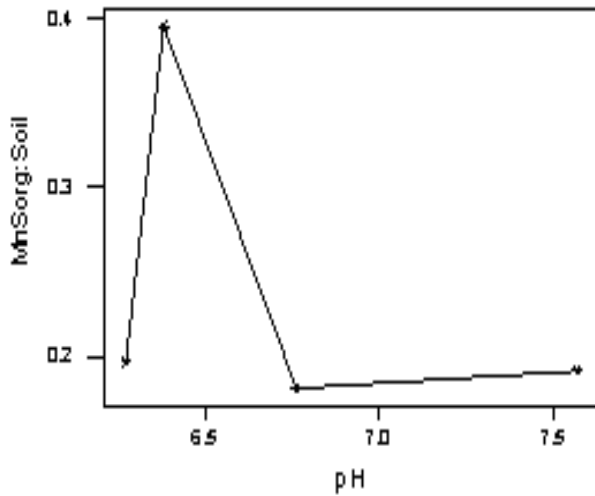


Fig. 10: Relationship of sorghum/soil manganese ratios and soil pH (water/soil, 1:1)

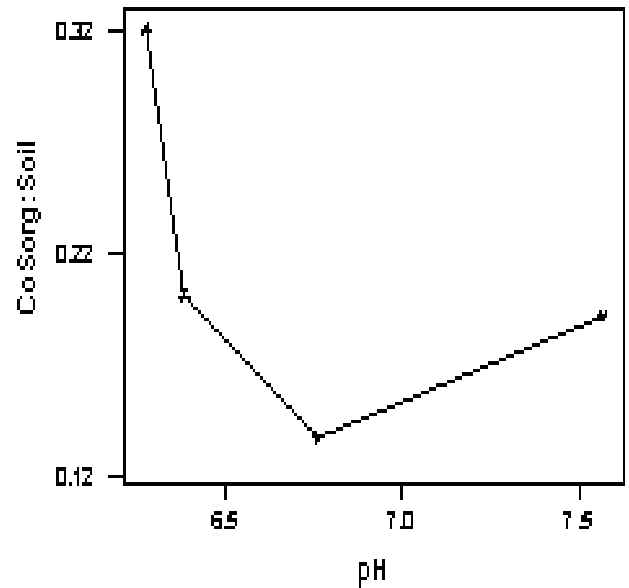


Fig.12: Relationship of sorghum/soil cobalt ratios and soil pH (water, 1:1)

#### 4. CONCLUSION

Cement dust is an environmental hazard since it affects soil properties, plants, man and animals within the vicinity of its deposition. The deposition of cement dust over a long period of time may change soil pH and adds to soil trace metals some of which are toxic to humans, animals and vegetation. Zn, Ni, and Mn, are heavy metals that were found in the environment above their background levels around the cement factory. Their presence in the environment may pose a serious potential

health hazard to the communities scattered around the factory. This can be so when the extractable content of the metals are used as indicators of the quantity of the metals available to plants. To this end there may be need to mitigate the likely effects by planting metal accumulating plants around the factory so as to remove metals from the environment.

## 5.0 REFERENCES

1. Hirano, T., Kiyota, M. T. and Aiga, I., 1995. Physical effects of dust on leaf physiology of Cucumber and kidney bean plants. *J. Environ Poll.* **89** (3); 255 - 261.
2. Wuana, R. A. and Okieimen, F. E., 2011. Heavy Metals in contaminated soils: A Review of sources, chemistry, risks and best available strategies for remediation. *International scholarly Research Network; Ecology*, vol. **2011**
3. Farmer, .A. M., 1993. The effects of Dust on vegetation - A Review. *Environ poll.* **79**, 63 - 75.
4. Huang, N. T., 2007. Cement Production. [www.inive.org/members-area/medias](http://www.inive.org/members-area/medias) (Accessed 30th June, 2007)
5. Tijani, A. A., Ajobo, O. and Akinola, A. A., 2005. Cement production externalities and profitability of crops enterprises in two local government areas of Ogun state. *J. Soc. Sci.* **11**, 43 -48.
6. Oyodele, A. J., Aina, P. O., Oluwale, F. and Asubiojo P. O., 1990. **Preliminary assessment of pollution effects of cement dust on soil and biomass production.** A paper presented at the 18th annual conference of the Nigeria soil science society, held at Maiduguri, Nigeria.
7. Kloseiko, J. and Tilk, M., 2006. Influence of cement clinker dust on carbohydrates in needles of scots pine shortly after the application. *Proc. Estonian Acad. Sci. Biol. Ecol.* **55**(2), 149-159.
8. Parn, H., 2006. Radial growth of conifers in regions of different cement dust loads. *Proc. Estonian Acad. Sci. Biol. Ecol.*, **55**(2), 108-122.
9. Abou Seeda, M. Z., Zaghoul, A. M. and Abdel-Gelil, A., 2005. The role of element dust in chemical remediation of sludge treated soil. *Ass. Univ. Bull. Environ. Res.* **8**(2), 89-106
10. Milford, J. B. and Davidson, C. I., 1985. The sizes of particulate trace elements in the atmosphere - A review. *J. Air poll. Contr. Assoc.* **35**, 124 - 126.
11. Omar, J. M. and Jasim, F., 1990. Some observations on the use of electro thermal atomic absorption spectrophotometry for the determination of chromium and copper in portland cement. *Microchemistry journal*, **41**(3), 348 - 355.
12. Andrej, J., 1987. Bees and their products as indicators of environmental pollution. *Med. Weter.* **43** (6), 353 - 356.
13. Kara, A., Cetin, S. C., Turgay, O. C., and Kizilkaya, R., 2010. Effects of heavy metals on soil enzyme activities. In Sherameti, I. and Varma, A. (ed.) Soil heavy metals, soil biology. Heidelberg 19, Pp237 – 265
14. Kabata-Pendias, A. and Pendias, H., 2001. Trace metals in soils and plants, 2<sup>nd</sup> edition CRC Press, Boca Raton, Fla, USA
15. Pierzynski, G. M., Sims, J. T. and Vance, G. F., 2000. Soil and environmental Quality, 2<sup>nd</sup> edition. CRC Press, London, UK.
16. D'Amore, J. J., Al-Abed, S. R., Scheckel, K. G., and Ryan, J. A., 2005. Methods for speciation of metals in soils: A Review, *Journal of environmental quality*, **34**, (5) pp1707 – 1745.
17. Garrido, S., Campo, G. M. D., Esteller, M. V., Vaca, R., and Lugo, J., 2002. Heavy metals in soils treated with sewage sludge composting; their effect on yield and uptake of broad bean seeds (*vicia faba*). *Water, Air and soil pollution*, **166**, 303-319
18. Rascio, N. and Izzo F. N., 2011. Heavy metal hyperaccumulating plants: How and why do they do it? And what make them so interesting? *Plant Sci.* **180**, 169-181
19. Wong, J. W. C. and Selvam, A., 2006. Speciation of heavy metals during co-composting of sewage sludge with lime, *Chemosphere*, **63**, 980-986
20. Jordao, C. P., Nascentes, C. C., Cecon, P. R., Fontes, R. L. F. and Pereira, J. L., 2006. Heavy metal availability in soil amended with composted urban solid wastes. *Environmental monitoring and assessment*, **112**, 309-326
21. Khan, S., Cao, Q., Zheng, Y. M., Huang, Y. Z. and Zhu, Y. G., 2008. Health risk of heavy metals in contaminated soils and food crops irrigated with waste water in Beijing, China. *Environmental pollution*, **152**, 686-692
22. Singh, J. and Kalamdhad, A. S., 2011. Effects of heavy metals on soil, plants, human health and aquatic life. *International Journal of Research in Chemistry and Environment*, **1**, 15-21
23. Speira, T. W., Kettlesb, H. A., Percivac, H. J. and Parshotam, A., 1999. Is soil acidification the cause of biochemical responses when soils are amended with heavy metal salts? *Soil Biology and Biochemistry*, **31**, 1953-1961
24. Maslin, P. and Maier, R. M., 2000. Rhamnolipid-enhanced mineralization of phenanthrene in organic-metal co-contaminated soils. *Bioremediation Journal*, **4** (4), 295-308
25. Nigeria Stock Exchange, NSE, 2004. Investors guide: The cement industry in Nigeria. <http://www.pangaepartners.com/nigjuly.htm> (accessed, April, 2004).
26. Smith, S. R., 1994. Effect of soil pH on availability to crops of metals in sewage sludge treated soils. 1. Nickel, copper and zinc uptake and toxicity to ryegrass. *Environ. Poll.* **85**, 321 – 327
27. Juste, C. and Tauzin, J., 1992. Comparison de la biodisponibilite du cadmium contenu dans differentes matieres fertilisantes. *C. R. Acad. Agric. Fr.* **79**, 71 - 79.
28. Voutsas, D., Grimanis, A. and Samara, C., 1996. Trace elements in vegetables grown in an industrial area in relation to soil and air particulate matters. *Environ. Poll.* **94**, 325 - 335.
29. Luo, Y. and Rimmer, D. L., 1995. Zinc - copper interactions affecting plant growth on a metal contaminated soil. *Environ. Poll.* **88**, 79 - 83.

30. Markert, B., 1994. Plants as bioindicators - potential advantages and problems. In: Andriano, D. C., Chen. Z. S., and Yang, S. S. (eds.) *Biochemistry of trace elements. Science and Technology letters*, Northwood, New York. Pp 601 - 613.
31. Kabata - pendias, A. and Pendias, H., 1984. Trace elements in soil and plants. CRC press Boca Raton USA
32. Huchabee, J. W., Sanz-Diaz, F., Janzen, S. A and Solomon, J., 1983. Distribution of mercury in vegetation at Almaden, Spain. *Environ. Poll.* **30**, 211 - 224.
33. Hovmand, M. F., Tjell, J. C. and Mosbaek, H., 1983. Plant uptake of airborne cadmium. *Environ. Poll.* **30**, 27 - 38.
34. Alloway, B. J., 1990. Heavy metals in soils. Black Well, London.
35. McGrath, S. P., 1989. Crop yield and composition. In: de Haan, F. A. M. et al (eds.). Commission of the European communities DGXIII XII/523/89.
36. Sanchez - Camazaro, M., Sanchez - martin, M. J. and Lorenzo, L. F., 1994. Lead and cadmium in soils and vegetables from urban gardens of Salamanca (spain). *Sci Total Environ.* **146/147**, 163 - 168.
37. Larsen, E. H., Moseholm, L. and Nielson, M. M., 1992. Atmospheric deposition of trace elements around point sources and human health risk assessment. II. Uptake of arsenic and chromium by vegetables grown near a wood presentation factory. *Sci. Total Environ.* **126**, 263 - 275.
38. Harrison, R. M. and Chirgawi, M. B., 1989. The assessment of air and soil as contributors of some trace metals to vegetable plants I. Use of a filtered air growth cabinet. *Sci. Total Environ.* **83**, 13 - 34.
39. Feigin, A., Ravina, I. and Shalhevet, J., 1991. Irrigation with treated sewage effluent. Springer – verlag, Berlin.
40. Temple, P. J. and Bessessar, S., 1981. Uptake and toxicity of nickel and other metals in crops grown on soil contaminated by nickel refinery. *J. Plant Nutr.* **3**(103), 473 – 482.
41. Lebersli, E. M. and Steinnes, E., 1987. Metal uptake in plant from a birch forest area near copper smelter in Norway. *Water, Air, Soil, Poll.* **37**, 25 - 39.
42. Tyler, G., 1978. Leaching rates of heavy metal ions in forest soils. *Water, Air, Soil Poll.* **9**, 137 - 148.
43. Lombin, G., 1983. Evaluating the micronutrient fertility of Nigeria's semi-arid savanna soils: Zinc. *Soil Science*, **136**, 42 - 47.
44. Young, A., 1976. Tropical soils and soil survey, Cambridge Pp486
45. Mcfarland, M. L., Haby, V. A., Redmon, L. A. and Bade, D. H., 2001 - 2005. Managing soil acidity. Texas Agricultural and experiment station (TAES), SCS 2001 - 2005. <http://www.soilcrop.tamu.edu>.
46. Arslan, M. and Boybay, M., 1990. A study on the characterization of dust fall. *Atmosph. Environ.* **24A**, 2667 - 2671.
47. Allen, J. P. and Torres, I. G., 1991. Physical separation Techniques for contaminated sediments. In: Li, N. N. (ed.). Recent developments in separation sciences. CRC press, West Palm Beach FL Vol. V.
48. N R C, 1994. Alternatives for ground water clean up. National Research Council, National Academy Press, Washington DC.
49. Kinniburgh, D. G., Jackson, M. L. and Syers, J. K., 1976. Adsorption of Alkaline earth, transition and heavy metal cations by hydrous oxide gels of iron and aluminum. *Soil Sci. Soc. Amer. J.* **40**, 796 - 799.
50. Ulrich, B., 1983. Soil acidity and its relation to acid deposition. In, Ulrich, B. and Pankrath, J. (eds.). Effects of accumulation of air pollutants in forest ecosystems. Reidel Publ. Co. Dordrecht. Pp 127 – 146.
51. Evanko, C. R. and Dzombak, D. A., 1997. Remediation of metals contaminated soils and ground water. Technology Evaluation Report GWRTAC E - series TE. 97-01 Pp 1 - 13.
52. Dzombak, D. A. and Morel, F. .M. .M., 1990. Surface complexation modeling: Hydrous ferric oxide. John Wiley and sons New York.
53. Lindsay, W. L., 1972. Inorganic phase equilibria of micronutrient in soils. In: Mortvedt, J. J. Giordano, P. M. and Lindsay, W. L. (eds.). Micronutrients in Agriculture SSSA Madison, Wisconsin USA. Pp 41 - 58.
54. Norvell, W. A., 1972. Equilibria of metal chelates in soil solution. In: Mortvedt, J. J., Giordano, P. M. and Lindsay, W. L. (eds.). Micronutrients in Agriculture SSSA Madison, Wisconsin USA. Pp 115 - 138.
55. Scokart, P. O., Verdinne, K. M. and Borger, R. D., 1983. Mobility of heavy metals in polluted soils near zinc smelters. *Water, Air, Soil Poll.* **20**, 451 - 463.
56. Emmerich, W. E., Lund, L. J., Page, A. L. and Chang, A. C., 1982. Solid phase forms of heavy metals in sewage sludge - treated soil. *J. Environ. Qual.* **11**, 178 - 181.
57. Watmough, S. A. and Dickson, N. M., 1995. Dispersal and mobility of heavy metals in relation to tree survival in an aerially contaminated woodland soil. *Environ. Poll.* **90**, 135 - 142.

# Dielectric and Thermal Characterization of Insulating Organic Varnish Used in Electrical Machines Having Phenolic Chemical Base Filled With Carbon Nanotubes

D. Edison Selvaraj

Department of EEE  
Panimalar Engineering College  
Chennai, India

C. Pugazhendhi Sugumarar

Division of High Voltage  
Engineering  
College of Engineering, Guindy  
Anna University, Chennai,  
India

J.Ganesan

Department of EEE  
Sree Sowdambika College of  
Engineering  
Aruppukotai, India

S.Geethadevi

Department of EEE  
Aurora Technological and  
Research Institute  
Uppal, Hyderabad, India

M.Rajkumar

D.Krishnamoorthy  
Department of EEE  
Dhanalakshmi Srinivasan  
Engineering College of  
Engineering and Technology  
Mamallapuram, Chennai, India

S. Dinesh Kumar

Research Scholar  
Department of EEE  
St. Peter's University  
Avadi, Chennai, India

---

**Abstract:** In recent days, a lot of attention was being drawn towards the polymer nanocomposites for use in electrical applications due to encouraging results obtained for their dielectric properties. Polymer nanocomposites were commonly defined as a combination of polymer matrix and additives that have at least one dimension in the nanometer range scale. Carbon nanotubes were of a special interest as the possible organic component in such a composite coating. The carbon atoms were arranged in a hexagonal network and then rolled up to form a seamless cylinder which measures several nanometers across, but can be thousands of nanometers long. There were many different types, but the two main categories are single-walled nanotubes (SWNTs) and multi-walled nanotubes (MWNTs), which are made from multiple layers of graphite. Carbon nanotubes were an example of a nanostructure varying in size from 1-100 nanometers (the scale of atoms and molecules). Nano composites were one of the fastest growing fields in nanotechnology. Extensive literature survey has been done on the nanocomposites, synthesis and preparation of nano filler. The following objectives were set based on the literature survey and understanding the technology.

- Complete study of Organic varnish and CNT
- Chemical properties
- Electrical properties
- Thermal properties
- Mechanical properties
- Synthesis and characterization of carbon nanotubes
- Preparation of polymer nanocomposites
- Study of characteristics of the nanocomposite insulation

Dimensioning an insulation system requires exact knowledge of the type, magnitude and duration of the electric stress while simultaneously considering the ambient conditions. But, on the other hand, properties of the insulating materials in question must also be known, so that in addition to the proper material, the optimum, e.g. the most economical design of the insulation system must be chosen.

**Keywords:** Varnish, CNT, SEM, X-ray diffraction, TGA

---

## 1. INTRODUCTION

The important properties of insulating materials were physical, chemical, thermal, electrical, mechanical and optical

properties. These properties were necessary for the selection of insulation materials.

### 1.1 Chemical properties

When impurities diffuse into insulating materials, this can cause chemical change. Only inorganic materials such as glass and densely fired ceramic materials are practically impermeable. In synthetic organic materials diffusion can take place within the molecular framework of the polymer. The diffusion velocity depends upon the material structure and the affinity of the base material. For example, all organic insulating materials absorb moisture by diffusion. The dielectric and electrical properties deteriorate as a result. Dissolved salts produced by hydrolysis or from impurities increase the conductivity and cause a poorer dissipation factor and break-down field strength [1]. The high dielectric constant of water modifies the dielectric constant of the material and causes a change in the voltage distribution during alternating voltage stressing [2]. In addition, the absorbed water can lead to changes in dimension and corrosion of the electrodes. Insulating materials for outdoor application should have poorly wettable surfaces so that closed water paths, which reduce the strength, are avoided. Inorganic materials show resistance to alkalis and acids [3]. Organic materials are attacked by strongly oxidizing acids, by alkalis as well as by hydrocarbons specific to the materials. In outdoor application of insulating materials, wet pollution layers can be decomposed by the electric stress and the heat so generated to form aggressive chemicals: these with the additional influence of light, oxygen, ozone, heat and UV radiation attack the insulating material.

## 1.2 Electrical properties

### 1.2.1 Breakdown field strength

The breakdown field strength is an extraordinary important material property for dimensioning an insulation system. Although it does not represent a constant specific to the material, what is more, it depends more or less strongly upon several influencing parameters as radius of curvature and surface finish of the electrodes, layer thickness, type of voltage, stress duration, pressure, temperature, frequency and humidity [4]. For solid insulating materials, certain criteria are available from measurement of the breakdown voltage or the breakdown field strength on plate-like samples in a homogeneous or weakly inhomogeneous field [5]. A standardized testing arrangement for the determination of the breakdown field strength of plates or foils up to sample thickness of 3mm. in order to prevent gliding discharges along the surface of the insulating plate, the entire arrangement is embedded in an insulating liquid with an appropriate dielectric constant. The breakdown test is conducted with an alternating voltage, which should be increased from zero to the breakdown value within 10-20 s. The median value of the breakdown voltage is determined from five samples; if any value lies more than 15% of the median value, 5 additional samples must be tested and the median value then determined from 10 samples. The breakdown field strength can be evaluated from the breakdown voltage and the smallest electrode spacing.

### 1.2.2 Insulation resistance

Practical insulation systems frequently comprise many dielectrics which are stressed in parallel. Thus, for example, the insulation resistance of a support insulator consists of the combination in parallel of surface resistance and volume resistance. While the volume resistance, commonly expressed as specific resistance in  $\Omega$  cm, is often independent of surrounding medium, the surface resistance is appreciably influenced by ambient conditions such as pressure,

temperature, humidity, dust etc. An arrangement for the measurement of the volume resistance of plate-type insulating material samples is discussed. In this arrangement, the live electrode, which also supports the plate-type sample, is arranged opposite a measuring electrode. The volume resistance is calculated from the direct voltage applied (100 V or 1000 V) and the current taken by the measuring electrode. A guard arranged concentrically around the measuring electrode with a 1 mm gap prevents erroneous measurements caused by surface currents. Special testing arrangements are available for tube-shaped insulating material samples, for insulating compounds which can be melted and for liquid insulating materials [6]. Common insulating materials exhibit a specific volume resistance of  $10^{12}$  to  $10^{13}$   $\Omega$  cm, whereas superior materials can reach resistance values up to  $10^{17}$   $\Omega$  cm or even higher. To measure the surface resistance metallic knife-edges are used, set up at a gap spacing of 1 cm over a length of 10 cm on the surface of the insulating material under test and direct voltage is applied. From the voltage and current, the surface resistance, expressed in ohms, is determined.

### 1.2.3 Tracking strength

When an insulation system was electrically stressed a current which was determined by the surface resistance flows on its surface and was referred to as leakage or creepage current. It was easy to understand that the ambient conditions temperature, pressure, humidity and pollution essentially determine the magnitude of this leakage current, i.e. no, or only limited, deterioration of the surface properties shall occur. Leakage currents result in thermal, and due to the by-products, also chemical stressing of the surface. The visible effects of overstressing are tracks resulting from material decomposition; these can appear in the form of a conducting path making further electric stressing of the material impossible, or as erosion, without leaving a conducting track behind [7]. Although the insulating properties are adversely affected by erosion, e.g. by the ease of dust deposition, yet further electric stressability was not precluded. Erosion occurs either in plates or as pits. Tracking is not restricted to insulating surfaces of outdoor arrangements but can also occur, under unfavorable circumstances, indoor applications or even in the interior of equipment. It is influenced for instance by the material properties, by the form and finish of the electrodes and surfaces, and also by the external conditions. Due to merging of several localized tracks, a complete flashover can be facilitated or initiated. Testing of insulating materials for their tracking strength is undertaken according to prescribed methods. In the method, VDE electrodes are placed on insulating material sample of at least 3 mm thickness and 380 V alternating voltages as applied to the electrode arrangement as per IEC publication 112 (1979). A pipette provides one drop of the testing solution of prescribed conductivity every 30 s; this wets the surface of the insulating material between the electrodes and causes leakage currents. As test result either the number of drops up to the time of automatic switch-off of the test circuit is evaluated, or the greatest pitting depth is measured.

### 1.2.4 Arcing resistance

Flashovers along the surfaces of insulating materials, with a subsequent power-arc, are indeed very rare, but basically unavoidable faults in technical insulation systems. Insulating materials exposed to the influence of the arc must therefore experience no, or only minimal, variations in their electrical and mechanical properties, viz. be arc resistant. Due to the

high arc temperature and as a consequence of incomplete burning of the insulating material, conducting tracks can remain which no longer permit further electric stressing. To determine the arcing resistance, carbon electrodes supplied with 220 V direct voltages are set up on the insulating plate. With an arc struck on the surface of the insulating, the electrodes are moved apart at a velocity of 1 mm/s up to a maximum separation of 20 mm. Six levels of arcing resistance, L1 to L6, defined according to the destruction caused by the arc, are used to judge the materials.

### 1.2.5 Dielectric constant and dissipation factor

For practical insulating materials, apart from the deformation polarization (electronic, ionic, lattice polarization), the orientation polarization is of particular significance since many insulating materials have permanent dipoles in their molecular structure. This is major cause of polarization losses and is responsible for the frequency dependence of  $\epsilon_r$  and  $\tan\delta$ , which is important for technical applications. The different relaxation times result in frequency limits beyond which the respective mechanisms no longer exist, because the corresponding dipole movement does not occur. This is why the dielectric constant must also decrease. The occurrence of polarization losses, as well as the increase of losses due to ionic conduction are recognized from the curve  $\tan \delta = f(\nu)$ . Measurement of  $\tan \delta$  and the determination of  $\epsilon_r$  were done using bridge circuits.

## 1.3 Thermal properties

In equipment and installations for the supply of electricity, heat is generated by ohmic losses in conductors, through dielectric losses in insulating materials and through magnetization and eddy-current losses in the iron [8]. Since, by comparison with metals, insulating materials have only a very low thermal stability, the permissible temperature rise of the insulating material often restricts the use of the equipment. Knowledge of the thermal properties of the insulating materials is, therefore, important for the construction and design of equipment and setups.

### 1.3.1 Specific heat

Due to the inertia of thermal transport, an insulating material must be in a position to absorb short-duration thermal pulses; caused by rapid load variations, via its thermal capacitance by an increase in temperature.

$$\Delta T = W / c * m \quad (1)$$

Where

c is the specific heat of insulating material,  
m is the mass and  
W is the supplied energy.

### 1.3.2 Heat transport

During continuous stressing under static operating conditions, the heat generated as a result of loss must be dissipated through the surroundings. Transport mechanisms are thermal conduction, convection and radiation. In thermal conduction, the thermal current flowing between flat plates was expressed by

$$P = A * \lambda * (T_1 - T_2) / s \quad (2)$$

Where

A is the area of the plate,  
s is the plate thickness and  
(T1- T2) is the temperature difference.

The proportionality factor  $\lambda$  is the thermal conductivity which can be assumed to be assumed constant in the technically interesting temperature range. For rapid removal of loss heat from electrical equipment good thermal conductivity is desirable. This requirement is satisfied best by crystalline insulating materials because the regular arrangement of atomic movement. In contrast, amorphous materials have distinctly poorer thermal conduction.

### 1.3.4 Linear thermal expansion

Insulating materials are construction materials which are frequently employed in contact with metals. On account of the larger thermal expansion of organic insulating materials, the danger of mechanical overstressing exists and this could result in the development of cracks or electrode arrangement. For inorganic insulating materials, the linear thermal expansion is lower than for metals; so an improvement is effected by filling organic materials with inorganic substances. Partly crystalline materials very often have a greater thermal expansion than amorphous materials.

### 1.3.5 Thermal stability

An important property of insulating materials is the shape retention on heating. There are two methods to determine this. The warm shape retention according to Martens is determined for a standard testing rod of 10 x 15 mm<sup>2</sup> cross-section and 120 mm length, which is stressed uniformly over the entire length with a bending stress of 500 N/cm<sup>2</sup>. At the same time the temperature of the surrounding air is increased at the rate of 50°C/h. The temperature at which the rod reaches a specific bending denotes the warm shape retention according to Martens. For thermoplastic materials the Vicat method is also applied. The Vicat temperature is that temperature at which a blunt needle of 1 mm<sup>2</sup> cross-section under a force of 10 N or 50 N penetrates to a depth of  $1 \pm 0.1$  mm into the insulating material. A high value for shape retention under heat is a decisive advantage of inorganic insulating materials over the inorganic kind.

## 1.4 Mechanical properties

The mechanical requirements are a consequence of the fact that most of the insulating materials are simultaneously construction materials with load-bearing properties. Depending upon the application, important properties are: Tensile strength, Bending strength, pressure strength, Bursting-pressure withstand strength, Modulus of elasticity, Hardness and Impact resistance [9]. The choice of an insulating material for a particular purpose often makes it necessary to find a compromise between the diverse requirements and the properties which satisfy them only incompletely. In addition, cost is also a major consideration for the insulation.

## 1.5 Properties of the Organic Varnish

The important electrical, chemical, physical and thermal properties of the organic varnish were given in Table 1.

Table 1 Properties of the organic varnish

Properties	Quantity
Density	1430 kg/m <sup>3</sup>
Young's modulus	3200 MPa
Tensile strength	75-90 MPa
Elongation	4-8 kJ/m
Glass temperature	>400 °C
Vicat softening point	220 °C

Thermal conductivity	0.52 W/(m·K)
Coefficient of thermal expansion	$5.5 \times 10^{-5}$ /K
Specific heat capacity	1.15 kJ/(kg·K)
Water absorption	0.32
Dielectric constant at 1 MHz	3.5

		grams	ate grams		
A	0.16:1:16	2.0995	0.8062	9.09	25
B	0.32:1:16	4.199	0.8062	9.09	25
C	0.32:2:16	4.199	1.6124	9.09	25
D	0.48:2:16	6.2985	1.6124	9.09	50

## 1.6 Properties of Carbon Nanotubes

Carbon nanotubes have several unique properties. Carbon nanotubes are among the strongest and stiffest materials yet produced owing to their extremely high strength-to-weight ratio. It has unique electrical, thermal and optical properties which make them highly conductive to electricity and heat. It also has a distinctive flexible and kinetic property. The different properties of the carbon nanotubes were given in Table 2.

Table 2 Properties of carbon nanotubes

Properties	Quantity
Tensile strength	63 Gpa
Density	1.3 to 1.4 g·cm <sup>-3</sup>
Specific strength	48,000 kN·m·kg <sup>-1</sup>
Current density	$4 \times 10^9$ A/cm <sup>2</sup>
Temperature stability in air	750 °C
Temperature stability in vacuum	2800 °C
Thermal conductivity	$385 \text{ W} \cdot \text{m}^{-1} \cdot \text{K}^{-1}$

## 2. SYNTHESIS AND CHARACTERIZATION OF CARBON NANOTUBES

### 2.1 Synthesis of Carbon Nanotubes

It was observed that most of the research work was carried out with single metal catalysts and a very little amount of research work was carried out on the synthesis of carbon nanotubes using bimetallic catalysts [10]. Hence it was decided to take up research on synthesis of carbon nanotubes using bimetallic catalyst. The synthesis of CNT involves three stages:

- (1) Preparation of catalysts for CNT
- (2) Preparation of CNT
- (3) Purification of CNT

#### 2.1.1 Preparation of Catalysts for carbon nanotubes

Catalysts with different Mo: Fe: Al<sub>2</sub>O<sub>3</sub> molar ratios were prepared by adding calculated amount of Ammonium hexamolybdate tetra hydrate and ferrous sulphate heptahydrate into a suspension of alumina powder in methanol. The solvent was evaporated under nitrogen gas flowing in a water bath and the resultant material was heated to 100 – 200° C for 3 hours. The fine powders were then calcined for 1 hour at 500° C and then heat treated with Argon gas flowing for 30 min at 820° C and reground before loading into CVD apparatus. The different concentrations of catalysts prepared were illustrated in the Table 3.

Table 3 Different catalyst concentrations

S. No	Molar ratio of Mo:Fe:Al <sub>2</sub> O <sub>3</sub>	Weight of Ammonium hexamolybdate	Weight of ferrous sulphate	weight of alumina grams	Volume of methanol (ml)

#### 2.1.2 Preparation of carbon nanotubes

The experimental setup consists of a horizontal reaction furnace, Quartz tube, PID controller, Flow meters, Control valves, Gas sources and Thermocouple. CVD apparatus consists of a horizontal reaction furnace with a heating capacity of up to 1500° C. The length of the furnace is 1m and has an inner diameter of 10cm. The quartz tube used to carry out the deposition has a length of 1.2m with outer diameter of 8cm and inner diameter of 7.5cm. The quartz tube is placed inside the horizontal reaction furnace. The heating coils go around the quartz tube and heat it uniformly [11]. The quartz tube is fixed on either side of furnace with supports. A proportional integral differential (PID) controller is provided in the furnace to control the temperature, time and heating rate of the reaction. The PID programming and current control is done manually. The controller displays the set and current temperature and the current is automatically adjusted by the controller to maintain the set temperature [12]. The controller also compensates the heat loss due to the gas flow. Three cylinders of pure Nitrogen (N<sub>2</sub>), Acetylene (C<sub>2</sub>H<sub>2</sub>) and Argon (Ar) were connected to the quartz tube through control valve and flow meter. The flow meter shows the rate of carbon source and nitrogen, which enters the reaction tube. Control valves are used to control the flow rate of gases passed in to the furnace. Rubber hoses are used to connect the cylinders with flow meter and valves [13]. Approximately 200mg of catalyst powder is spread uniformly into the quartz boat (Figure 3.4) and was placed in the central region of a horizontal 100 cm long quartz tube furnace having an inner diameter of 4.5cm. The furnace was flushed with argon gas while it was heated at a rate of 5° C/min till it attained 800° C. After the attainment of the desired temperature, H<sub>2</sub> gas was introduced into the furnace at a flow rate of 100 cc/min for 60 minutes so as to generate active metallic(Fe, Mo) or bimetallic (Fe-Mo) nano particles on Alumina support. Subsequently, C<sub>2</sub>H<sub>2</sub> gas in different quantities varying from 10 to 50 cc/min was also introduced into the furnace for 1 hour maintaining the flow of H<sub>2</sub> gas constant. After that it is allowed to cool at a rate of 5° C/min. and removed from the quartz tube for purification.

#### 2.1.3 Purification of Carbon Nanotubes

After synthesis the raw products were treated with a solution of KOH (1M) at 80° C in order to remove the alumina support and molybdenum will be evaporated at this temperature. The resulting material is washed several times with distilled water and then treated with a solution of HCL (1M) in order to remove the remaining iron particles. It was then washed with distilled water before being dried at 200° C.

## 2.2 Characterization of Carbon Nanotubes

The particle size of CNT was augmented by the scanning electron microscope and x ray diffraction.

#### 2.2.1 Scanning Electron Microscope

The scanning electron microscope (SEM) was a type of electron microscope that creates various images by focusing a high energy beam of electrons onto the surface of a sample

and detecting signals from the interaction of the incident electrons with the sample's surface. The SEM was capable of producing high-resolution images of a sample surface in its primary use mode, secondary electron imaging. Due to the manner in which this image was created, SEM images have great depth of field yielding a characteristic three-dimensional appearance useful for understanding the surface structure of a sample. Here the image was built up by using an electron probe of very small diameter which scans the specimen surface in parallel straight lines. When the electron probe scans the specimen, secondary electrons were emitted and these were collected, the current was amplified and the image was formed on the screen. The magnification was about 300,000. The SEM analysis was done for the carbon nanotubes at 10 kV, 10  $\mu\text{m}$  and 25 kV, 1  $\mu\text{m}$ . The result was given in Figure 1 and 2. SEM result was used to augment the particle size of carbon nanotubes.

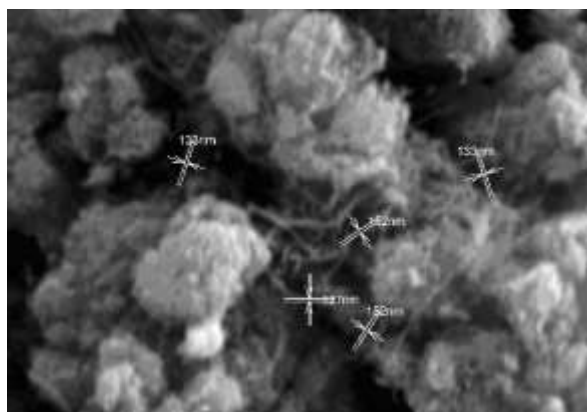


Figure 1 SEM analysis for carbon nanotubes at 10 kV, 10  $\mu\text{m}$

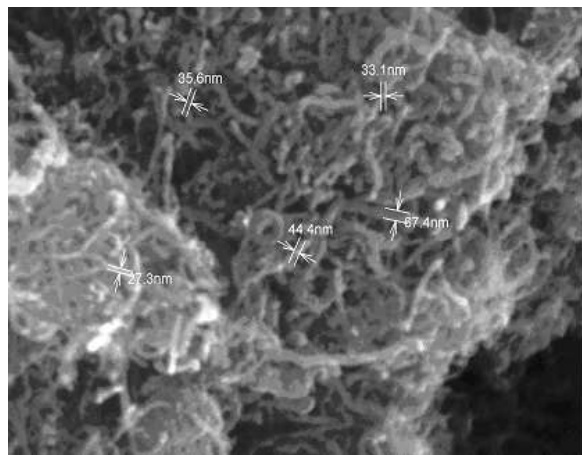


Figure 2 SEM analysis for carbon nanotubes at 25 kV, 1  $\mu\text{m}$

### 2.2.2 X-ray diffraction

X-ray diffraction (XRD) is a versatile, non-destructive technique that reveals detailed information about the chemical composition and crystallographic structure of natural and manufactured materials. The X-ray diffraction pattern of a pure substance is like a fingerprint of the substance. The powder diffraction method is thus ideally suited for characterization and identification of polycrystalline phases. The XRD result for the carbon nanotubes was shown in Figure 3. The micrometer size of the carbon particles is found using XRD. From the graph, it is clear that the value of  $2\theta$  should lie between  $30^\circ$  to  $40^\circ$ .

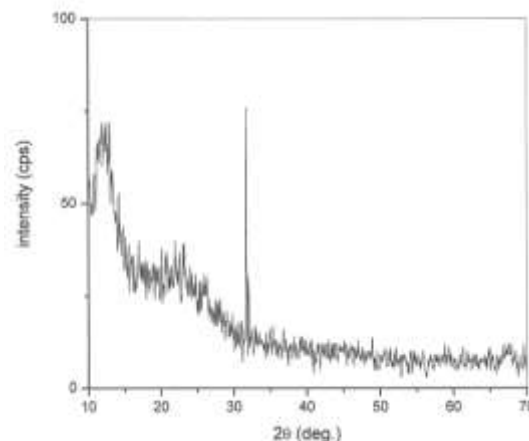


Figure 3 XRD pattern for carbon nanotubes

## 2.3 Sample Preparation

The process of converting liquid state organic varnish into solid state sample was called as curing.

### 2.3.1 Types of curing

There were two different types of curing. They were

- (1) Thermal curing - The oligomer which was having a repeat unit (1 to 10) was converted into polymer by using thermal curing.
- (2) Radical initiator curing - In this method, curing agents such as amines, anhydrates and acids are used as curing agents.

### 2.3.2 Curing of organic varnish

The curing method used for organic varnish having phenolic base was radical initiator curing. In this process DDM was used as curing agent. The procedure used in this curing process was as follows:

80% of enamel and 20% of epoxy resin was taken.

DDM was taken in proportion to epoxy resin. For 1gm of resin 0.27 gm of DDM was added.

DDM was melted at  $60-80^\circ\text{C}$  for 10 minutes.

Organic varnish having phenolic base, resin and melted DDM was mixed in a beaker.

The mixture was poured into the die which was coated by a Teflon sheet.

The die was heated at  $120^\circ\text{C}$  for 2 hours and  $130^\circ\text{C}$  for 3 hours.

The die was cooled and the solid sample was taken.

### 2.3.3 Mixing of the organic varnish with carbon nanotubes

The enamel and the synthesized carbon nanotubes were mixed with the help of an ultrasonic vibrator. Rotary or linear motion was used in Ultrasonic vibrators to provide consistent vibration for laboratory and industrial shakers, screeners and classifiers, and bins and hoppers. They were powered by an electric motor, pneumatic pistons, or hydraulic fluid. The varnish and the carbon nanotubes taken in 1 wt%, 3 wt% and 5 wt% were completely mixed by the ultrasonic vibrations produced by the ultrasonic vibrators. Ultrasonic vibrations would refer to sound waves that have a frequency higher than human hearing. The vibration themselves would be the physical vibration of the molecules in the medium in which

the sound is traveling. Frequency Range= 20 kHz to 60 kHz (that would be above 20 kHz, or 20,000 cycles per second).

## 2.4 Curing of the Carbon Nanotubes Filled Enamel

The carbon nanotubes filled enamel so far obtained was in the liquid state. For the various analysis (DSA, TGA and breakdown strength measurements) solid form of the carbon nanotubes filled enamel would be very much effective. So the liquid state carbon nanotubes filled enamel was converted to solid state carbon nanotubes filled enamel. The process of converting the liquid state carbon nanotubes filled enamel into solid state is called as curing. Radical initiator curing method was used and DDM was used as a curing agent.

## 3. DIELECTRIC ANALYSIS

The various dielectric properties of the carbon nanotubes filled organic varnish such as breakdown electric strength, surface resistance, dielectric loss factor, quality factor, phase angle, heat generated, dielectric loss and dielectric conductivity were found.

### 3.1 Partial Discharge Measurement

Partial discharges are in general a consequence of local electrical stress concentrations in the insulation or on the surface of the insulation. Generally such discharges appear as pulses of duration of much less than 1s. The partial discharge includes a wide group of discharge phenomena such as internal discharges occurring in voids or cavities within solid or liquid dielectrics, surface discharges appearing at the boundary of different insulation materials, corona discharges occurring in gaseous dielectrics in the presence of inhomogeneous fields and continuous impact of discharges in solid dielectrics forming discharge channels (treeing). Every discharge event causes a deterioration of the material by the energy impact of high energy electrons or accelerated ions, causing chemical transformations of many types. The number of discharge events during a closed interval of time is strongly dependent on the kind of voltage applied and will be largest for a.c. voltages. The actual deterioration is dependent upon the material used. It was still the aim of many investigations to relate partial discharges to the life time of specified materials. The detection and measurement of discharges is based on the exchange of energy taking place during the discharge. These exchanges are manifested as electrical pulse currents, dielectric losses, e.m. radiation, sound, increased gas pressure and chemical reactions.

Partial discharge (PD) current pulses are very sharp pulses having a width of the order of nanoseconds. The IEC 60270 PD detectors are approximated the measured PD pulses as an impulse (less than 500kHz bandwidth). Auto transformer takes an input of 220 V, 50Hz, single phase and gives an output varies from 0 to 220V, 50Hz, single phase. The rating of high voltage transformer is 220/100kV, 50Hz, single phase. By varying the input from 0 to 220V the output varies from 0 to 100kV in proportion. Core made of iron type. The coupling capacitor shall be mounted insulated or other measures shall be taken to ensure that ground foil can be connected to the insulated terminal of the measuring impedance AKVD. Discharge free coupling capacitor is used in this setup. The coupling capacitor should preferably be high ( $C_c=1000\text{pF}$ ). AKVD is the measuring impedance, an inductor in parallel with a capacitor. The measuring impedance unit ( $Z_m$ ) was located physically close to the high

voltage coupling circuit and serves two main purposes: It attenuates the test voltage present on the high voltage coupling circuit to the safe value for the measurement of the partial discharge signals. It matches the amplifier to the high voltage coupling circuit in insuring a flat frequency response across the full measurement band width. The measuring impedance unit ( $Z_m$ ) should be configured in such a way as to permit test voltage level monitoring and to observe the phase relationship between the test voltage and the partial discharge pulses; this technique helps to identify the nature of the discharges. Agilent oscilloscope 54621A is used for the display of the waveforms. The DSO is connected to the DTM at the backend. The oscilloscope displays the phase position of the partial discharge pulses with respect to the AC test voltage. The phase position of the partial discharge pulses with respect to the AC test voltage allows conclusions about the location of the partial discharges in the test object.

The arrangement of electrodes and experimental set up used for partial discharge measurements is shown in the Figure 4.

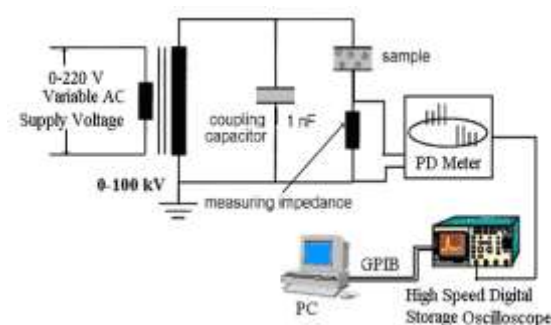


Figure 4 Circuit arrangements for Partial Discharge Measurement

Sample thickness : 3 mm

Diameter of upper electrode : 25mm

Diameter of lower electrode : 75mm

The entire arrangement in an insulating liquid with an appropriate dielectric constant (Ex: Insulating oil).

Before starting the experiment on the test specimen PD meter should be calibrated. The calibrator comprises a pulse generator in series with small capacitor of known value. The generator and the capacitor may be placed in the small box or may be connected together via a properly terminated coaxial cable of sufficient length to permit a calibration from the control room. The pulse generator should either have a known calibrated output level or its output level should be monitored. A suitable output level adjustment in the form of a calibrated potentiometer or a calibrated step attenuator should be provided. The following three methods specify the test procedure for PD measurements, the first verifies that test object is free from significant partial discharges up to a specified test voltages; second is used to determine the discharge inception and extinction voltages; and the third is used for measurement of discharge level at a voltage or voltages in range between the inception voltage and the maximum dielectric voltage. A voltage, well below the specified discharge free voltage, is applied to the test object, gradually increased to the specified voltage, and maintained for the specified time; there after it is decreased and switched off. The object is considered to have passed the test if the discharges do not exceed a specified level. A voltage well below the inception value is applied to the test object and gradually increased until discharge exceeds a specified level.

The test voltage at this discharge limit is recorded. The voltage is then increased by 10% and there after reduced to a value at which the discharge ceases or become less than a specified level. The voltage corresponding to this limit is recorded. For some insulation systems, the extinction and inception values may be influenced by the length of the time that the test voltage is maintained above the inception level. The PDG pulse generator is connected in parallel with the test object and normally operated on position "500pC". The effective PD of the PDG simulates a known partial discharge intensity of the object. With the measuring range selector 'E' of the DTM set on the respective position, the display is also set to 500pC with the potentiometer 'G' "CORR". For a defined test arrangement and with identical test objects, the correction factor has to be determined only once and holds good for all the measurements in the setup. The time domain data was collected after a stabilization period of 5 minutes. 25 cycles of data has taken with each discharge source. The period of 25 sampling with 2M data points was 500ms. The period of one sampling with 80k data points was 20ms. The discharge signal is captured on along with the superimposed sinusoidal signal for 25 cycles for the five types of discharges considered. The Partial discharge inception and extinction voltage values of the organic varnish and the organic varnish filled with the different (1 wt %, 3 wt% and 5 wt%) proportions of carbon nanotubes filled organic varnish and it was shown in the Table 4.

**Table 4 Partial discharge inception and extinction voltage of the organic varnish and the organic varnish with different (1 wt %, 3 wt% and 5 wt%) proportions of carbon nanotubes**

% wt of carbon Nano tubes	Inception voltage (kV)	p C	Extinction voltage (kV)	p C	% Decrease in Inception voltage	% Decrease in Extinction voltage
0	4.74	55	4.10	1.3	-	-
1	3.27	64	2.19	1.4	31.01	46.58
3	4.01	65	3.53	1.2	15.40	13.90
5	4.21	66	3.63	1.3	11.18	11.46

### 3.2 Breakdown voltage and electric strength

The breakdown voltage of an insulation system is that of the voltage with a certain time dependence for which the dielectric either temporarily or permanently loses its insulating property by the way of a discharge process. The intensity of the electric field at which breakdown occurs was called as dielectric strength or breakdown strength. Breakdown strength = Breakdown voltage / Thickness of the dielectric. It was measured in kV/mm or kV/cm. The electric breakdown strength of insulating material depends on a variety of parameters, such as pressure, temperature, humidity, field configurations, nature of applied voltage, imperfections in dielectric materials, material of electrodes, and surface conditions of electrodes, layer thickness, types of voltage, stress duration and frequency. The breakdown voltage shows an increasing dependence on the nature and smoothness of the electrode material. The breakdown strength reduces considerably due to the presence of impurities. The

breakdown field strength is an extraordinary important material property for dimensioning an insulation system.

For solid insulating materials, certain criteria are available from measurement of the breakdown voltage or the breakdown field strength on plate-like samples in a homogeneous or weakly inhomogeneous field. A standardized testing arrangement for the determination of the breakdown field strength of plates or foils up to sample thickness of 3mm as per IEC 60243 – 1 was as shown in Figure 5. AC breakdown tests were carried out at power frequencies (50 -60 Hz) using a step-up transformer supplied from a variable sinusoidal low voltage source. If tests were performed at different frequencies, the low voltage source may be a power amplifier controller by a low frequency generator. However, that in such circumstances the maximum test frequency should be considerably below the value at which dielectric losses within the material may become significant to precipitate failure due to thermal instability. The rate of voltage increase may be controlled by the use of a motor driven auto transformer. Alternatively an induction regulator may be employed. A controlled voltage rate of increase was necessary for the performance of the short-time and slow rate of rise breakdown tests. A step by step test would require only a manual voltage control. It was so popular before constant rate of rise sets became commonplace. A current limiting resistor was used to limit the current at breakdown. Its value should not be too large, since it may give rise to an unduly large voltage drop with the higher currents preceding breakdown. A value of 106 Ω / kV appears to be convenient in most cases.

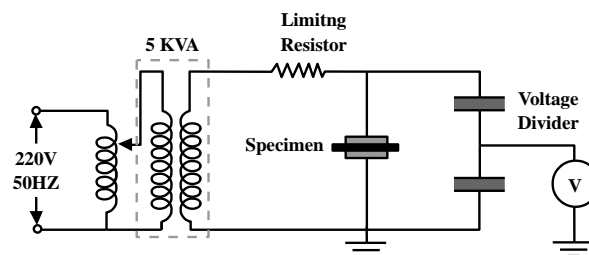


Figure 5 Circuit arrangements for AC Breakdown voltage test

The breakdown test was conducted with alternating voltage, which should be increased from zero to the breakdown voltage within 10-20 s. The median value of the breakdown voltage was determined from five samples; if any value lies more than 15% of the median value, 5 additional samples must be tested and the median value then determined from 10 samples. The breakdown field strength can be evaluated from the breakdown voltage and the smallest electrode spacing. The AC breakdown voltage values of pure organic varnish and the organic varnish filled with the different (1 wt %, 3 wt% and 5 wt %) proportions of carbon nanotubes filled organic varnish was shown in the Table 5.

**Table 5 AC breakdown voltage values of pure organic varnish and the organic varnish filled with different (1 wt %, 3 wt% and 5 wt %) proportions of carbon nanotubes**

% wt of carbon Nano tubes	Breakdown Voltage (kV)
0	7.7
1	5.54
3	6.22
5	6.55

The breakdown strength values of pure organic varnish and the organic varnish filled with the different (1 wt %, 3 wt% and 5 wt%) proportions of carbon nanotubes filled enamel was shown in the Table 6.

**Table 6 Breakdown strength of pure organic varnish and the organic varnish filled with different (1 wt %, 3 wt% and 5 wt%) proportions of carbon nanotubes**

% wt of carbon Nano tubes	Breakdown strength (kV/mm)	% Decrease
0	2.56	-
1	1.85	27.73
3	2.07	19.14
5	2.18	14.84

### 3.3 Surface resistance measurement

Practical insulation systems frequently comprise many dielectrics which were stressed in parallel. Thus, for example, the insulation resistance of a support insulator consists of the combination in parallel of surface resistance and volume resistance. While the volume resistance, commonly expressed as specific resistance in  $\Omega$  cm, was often independent of surrounding medium, the surface resistance was appreciably influenced by ambient conditions such as pressure, temperature, humidity, dust etc. An arrangement for the measurement of the volume resistance of plate-type insulating material samples was discussed. In this arrangement, the live electrode, which also supports the plate-type sample, was arranged opposite a measuring electrode. The volume resistance was calculated from the direct voltage applied (100 V or 1000 V) and the current taken by the measuring electrode. A guard arranged concentrically around the measuring electrode with a 1 mm gap prevents erroneous measurements caused by surface currents. Special testing arrangements were available for tube-shaped insulating material samples, for insulating compounds which can be melted and for liquid insulating materials. Common insulating materials exhibit a specific volume resistance of 1012 to 1013  $\Omega$  cm, whereas superior materials can reach resistance values up to 1017  $\Omega$  cm or even higher. To measure the surface resistance metallic knife-edges are used, set up at a gap spacing of 1 cm over a length of 10 cm on the surface of the insulating material under test and direct voltage is applied. From the voltage and current, the surface resistance, expressed in ohms, is determined. The surface resistance and surface resistivity of the organic varnish and the organic varnish filled with different (1 wt %, 3 wt% and 5 wt%) proportions of carbon nanotubes filled organic varnish and was presented in the Table 7.

**Table 7 Surface resistance and surface resistivity of the organic varnish and the organic varnish filled with different (1 wt %, 3 wt% and 5 wt %) proportions of carbon nanotubes**

% wt of carbon Nano tubes	$R_s$ ( $\Omega$ )	$\rho_s$ ( $\Omega$ cm)	% Increase in $R_s$	% Decrease in $R_s$	% Increase in $\rho_s$	% Decrease in $\rho_s$
0	7.09 x 10 <sup>8</sup>	1.36 x 10 <sup>9</sup>	-	-	-	-
1	6.21 x 10 <sup>8</sup>	1.16 x 10 <sup>9</sup>	-	12.41	-	14.7

3	5.15 x 10 <sup>8</sup>	1.01 x 10 <sup>9</sup>	-	27.36	-	25.73
5	12.6 x 10 <sup>8</sup>	2.62 x 10 <sup>9</sup>	77.71	-	92.64	-

### 3.4 Calculation of relative permittivity, dielectric conductivity and dielectric losses

Dielectric spectroscopy was used to find the loss factor, quality factor and phase angle of the dielectric material. From these factors, dielectric constant, dielectric conductivity, dielectric loss and heat generated under AC fields were found. Dielectric spectroscopy [LCR HITESTER 3532-50] also known as Electrochemical Impedance Spectroscopy, measures the dielectric properties of a medium as a function of frequency. It is based on the interaction of an external field with the electric dipole moment of the sample, often expressed by permittivity. It is also an experimental method of characterizing electrochemical systems. This technique measures the impedance of a system over a range of frequencies, and therefore the frequency response of the system, including the energy storage and dissipation properties, is revealed. Often, data obtained by EIS is expressed graphically in a Bode plot or a Nyquist plot. Real and Imaginary part of Relative Permittivity of the organic varnish was calculated from the following equations which was used to calculate the dielectric loss.

$$\text{Loss factor } \tan \delta = \frac{\epsilon_r''}{\epsilon_r'} \quad (3)$$

$$\text{Real part of relative permittivity } \epsilon_r' = \left( \frac{t * C_p}{A * \epsilon_0} \right) \quad (4)$$

Imaginary part of relative permittivity

$$\epsilon_r'' = \left( \frac{t}{\omega * R_p * A * \epsilon_0} \right) \quad (5)$$

$$\text{Dielectric conductivity } \sigma = \omega * \epsilon'' \quad (6)$$

$$\text{Dielectric losses } P = 2\pi * f * C * V^2 * \tan \delta \quad (7)$$

$$\text{The heat generated under AC field } W_{ac} = E^2 * f * \epsilon_r * \tan \delta / 1.8 * 10^{12} \text{ W / cm}^3 \quad (8)$$

Where

f is the frequency in Hz,

$\delta$  is the loss angle of the dielectric material and E is the applied electric field.

$C_p$  is the equivalent parallel capacitance [F]

$R_p$  is the equivalent parallel Resistance [ $\Omega$ ]

D is the dissipation factor (measured value)

$t_m$  is the average thickness [m]

A is the guarded electrode's surface area [m<sup>2</sup>]

D is the guarded electrode's diameter [m]

$\epsilon_0$  is the permittivity of free space = 8.854 x 10<sup>-12</sup> [F/m]

V is the applied voltage [V]

$\tan \delta$  is the dielectric loss tangent

The different dielectric properties like dissipation factor, quality factor and phase angle were found with the help of the Dielectric Spectroscopy. Dielectric constant, dielectric losses, dielectric conductivity and heat generated under AC fields were analyzed for various frequencies and the values were shown in Table 8 to 14.

**Table 8 Dissipation Factor**

Frequency in HZ	Pure Varnish	1 Wt % CNT mixed Varnish	3 Wt % CNT mixed Varnish	5 Wt % CNT mixed Varnish
50	8.865	2.793	2.98	3.83
100	6.496	1.194	1.590	1.663
1000	2.537	0.74	0.831	1.52
10000	1.508	0.29	0.8	1.229
100000	0.97	0.072	0.37	0.063
1000000	0.121	0.03	0.07	0.093
5000000	0.0627	0.003	0.063	0.028

Figure 6 shows Comparison of Dissipation Factor Vs Frequency for various samples at 90° C

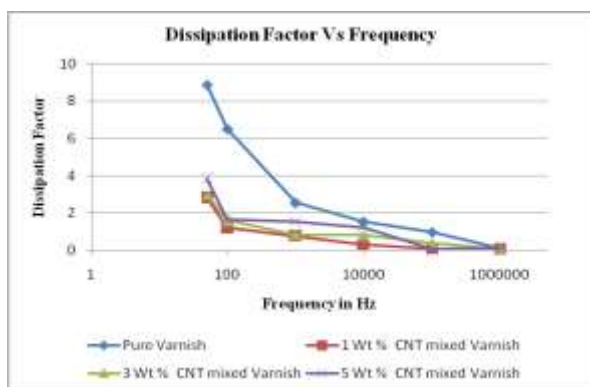


Figure 6 Comparison of Dissipation Factor Vs Frequency for various samples at 90° C

**Table 9 Quality Factor**

Frequency in HZ	Pure Varnish	1 Wt % CNT mixed Varnish	3 Wt % CNT mixed Varnish	5 Wt % CNT mixed Varnish
50	0.3	1.6	1.2	0.72
100	0.8	1.8	1.9	1.31
1000	1.65	4.65	3.1	2.6
10000	2.97	9.72	3.58	4.2
100000	6.26	14.97	9.3	15.43
1000000	9.64	15.8	11.9	13.84
5000000	18.95	10.5	15.72	9.8

Figure 7 shows Comparison of Quality factor Vs Frequency for various samples at 90° C

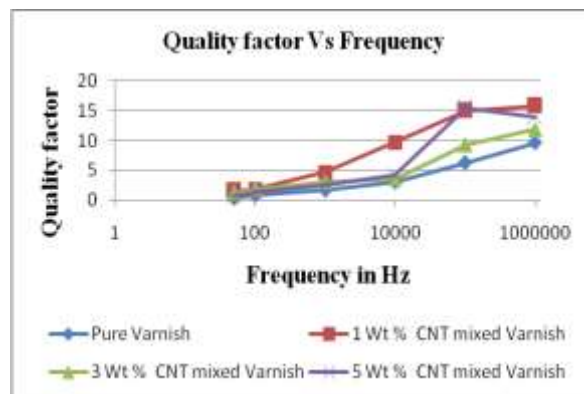


Figure 7 Comparison of Quality factor Vs Frequency for various samples at 90° C

**Table 10 Dielectric Constant**

Frequency in HZ	Pure Varnish	1 Wt % CNT mixed Varnish	3 Wt % CNT mixed Varnish	5 Wt % CNT mixed Varnish
50	227.35	58.37	102.9	100.37
100	165.47	54.85	99.24	96.41
1000	78.054	39.66	73.26	56.3
10000	49.51	27.66	39.29	25.36
100000	38.43	23.81	32.03	23.23
1000000	26.96	22.5	25.95	22.23
5000000	20.39	19.81	23.33	20.16

Figure 8 shows Comparison of Constant Vs Frequency for various samples at 90° C

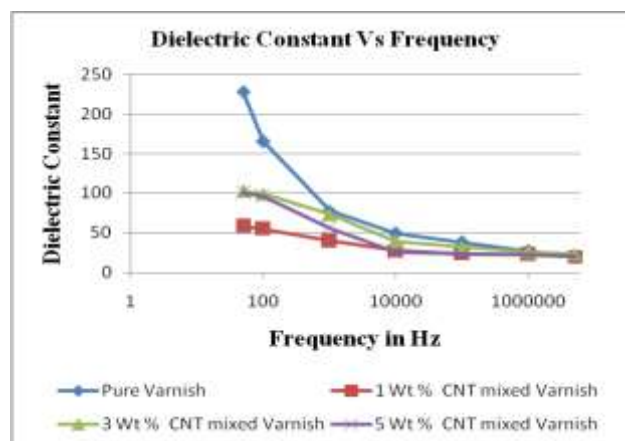


Figure 8 Comparison of Constant Vs Frequency for various samples at 90° C

**Table 11 Dielectric losses (μW)**

Frequency in HZ	Pure Varnish	1 Wt % CNT mixed Varnish	3 Wt % CNT mixed Varnish	5 Wt % CNT mixed Varnish
50	6.78	0.6	0.64	0.47
100	6.3	0.2	0.4	0.4
1000	8.5	0.97	1.53	1.9
10000	19.11	2.32	12.6	3.9

100000	49.01	18.22	25.53	12.2
1000000	259.76	107.79	178.24	172.26
5000000	589.63	667.35	557.68	1197.58

Figure 9 shows Comparison of Dielectric losses Vs Frequency for various samples at 90° C

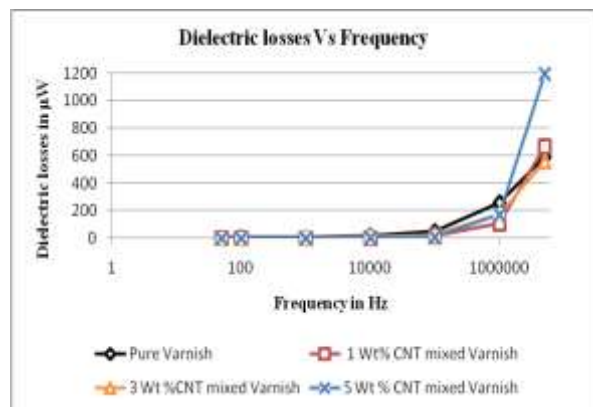


Figure 9 Comparison of Dielectric losses Vs Frequency for various samples at 90° C

Table 12 Dielectric conductivity (S)

Frequency in HZ	Pure Varnish	1 Wt % CNT mixed Varnish	3 Wt % CNT mixed Varnish	5 Wt % CNT mixed Varnish
50	4.82 x 10 <sup>-6</sup>	1.67 x 10 <sup>-12</sup>	9.61 x 10 <sup>-14</sup>	2.28 x 10 <sup>-13</sup>
100	4.9 x 10 <sup>-9</sup>	4.5 x 10 <sup>-12</sup>	2.81 x 10 <sup>-13</sup>	5.81 x 10 <sup>-3</sup>
1000	6.2 x 10 <sup>-6</sup>	1.22 x 10 <sup>-10</sup>	3.63 x 10 <sup>-11</sup>	1.77 x 10 <sup>-10</sup>
10000	1.57 x 10 <sup>-8</sup>	1.38 x 10 <sup>-8</sup>	8.94 x 10 <sup>-9</sup>	1.62 x 10 <sup>-8</sup>
100000	3.8 x 10 <sup>-8</sup>	1.44 x 10 <sup>-9</sup>	1.22 x 10 <sup>-6</sup>	1.17 x 10 <sup>-6</sup>
1000000	1.58 x 10 <sup>-4</sup>	8.66 x 10 <sup>-10</sup>	5.86 x 10 <sup>-4</sup>	9.81 x 10 <sup>-4</sup>
5000000	4.6 x 10 <sup>-4</sup>	5.2 x 10 <sup>-11</sup>	57.91 x 10 <sup>-3</sup>	103.32 x 10 <sup>-3</sup>

Table 13 Phase Angle

Frequency in HZ	Pure Varnish	1 Wt % CNT mixed Varnish	3 Wt % CNT mixed Varnish	5 Wt % CNT mixed Varnish
50	-7.05	-52.55	-44.62	-41.53
100	-10.21	-58.29	-58.44	-57.56
1000	-33.14	-75.66	-73.18	-63.25
10000	-63.36	-83.62	-69.78	-77.65
100000	-76.52	-86.91	-83.26	-86.32
1000000	-82.89	-87.38	-85.68	-85.63
5000000	-87.51	-94.76	-92.12	-81.29

Table 14 Heat Generated (W/cm<sup>3</sup>)

Frequency	Pure	1 Wt %	3 Wt %	5 Wt %
-----------	------	--------	--------	--------

in HZ	Varnish	CNT mixed Varnish	CNT mixed Varnish	CNT mixed Varnish
50	32.24	1.465	1.86	1.74
100	33.34	2.632	2.77	2.04
1000	43.61	2.23	9.13	8.9
10000	82.35	9.64	49.24	25.77
100000	242.31	36.9	137.76	53.38
1000000	1279.79	324.01	729.21	773.15
5000000	3128.76	1834.05	2488.81	5185.01

Figure 10 shows Comparison of Heat Generated Vs Frequency for various samples at 90° C

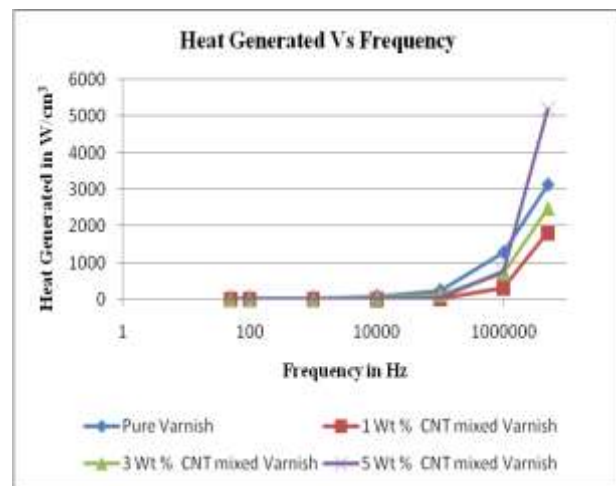


Figure 10 Comparison of Heat Generated Vs Frequency for various samples at 90° C

#### 4. THERMAL ANALYSIS

A generally accepted definition of thermal analysis is “A group of techniques in which a physical property of a substance and/or its reaction products is measured as a function of temperature whilst the substance is subjected to controlled temperature program”. It is based upon the detection of changes in the heat content (enthalpy) or the specific heat of a sample with temperature (Skoog 2003). Such enthalpy changes may be detected by thermal analysis and related to the processes occurring in the sample. Thermal analysis can be done by different methods such as the measurement of heating curves, dynamic adiabatic calorimetry, differential thermal analysis (DTA), differential scanning calorimetry (DSC), thermo gravimetry (TG), thermal mechanical analysis (TMA) and dynamic mechanical thermal analysis (DMTA). Thermo Gravimetric Analysis (TGA) is a simple analytical technique that measures the weight loss (or weight gain) of a material as a function of temperature. Thermo gravimetry (TG) was a material characterization technique, where the mass of a sample in a controlled atmosphere is recorded continuously as a function of temperature or time as the temperature of the sample is increased (usually linearly with time). In TG, the sample and reference are both maintained at the temperature predetermined by the program even during a thermal event in the sample. The typical arrangement for the components of a TGA instrument is revealed in Figure 11.

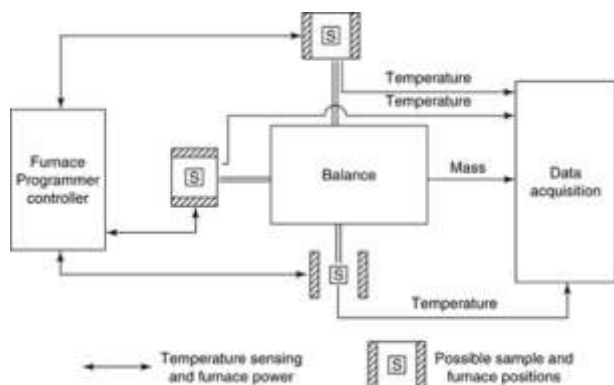


Figure 11 Typical arrangements for the components of a TGA instrument

In the Diamond TG/DTA 6000 Instrument system the sampling size can be analyzed from 0.1mg to 10g and the heating rate of 0.1-50°C/min for the temperature range from 50°C to 900°C and it maintain consistent heating rate and gas flow. This instrument measures sampling purity, reaction rate, identification, activation energy and heat of reactions. TG result of the organic varnish was shown in the Figure 12 and the 1 wt%, 3 wt% and 5 wt% of carbon nanotubes mixed with the organic varnish was shown in the Figure 13, 14 and 15. The test result was a graph of the TGA signal (actual weight loss or gain converted to percent weight loss) on the Y-axis plotted versus the sample temperature in °C on the X-axis. TG analysis was used to record and study the dependences of the mass of the sample on the ageing time or on a gradually increasing temperature and evaluate the heat of exothermic and endothermic reactions in the material. TG analysis was also used to determine the thermo elasticity and the thermo stability.

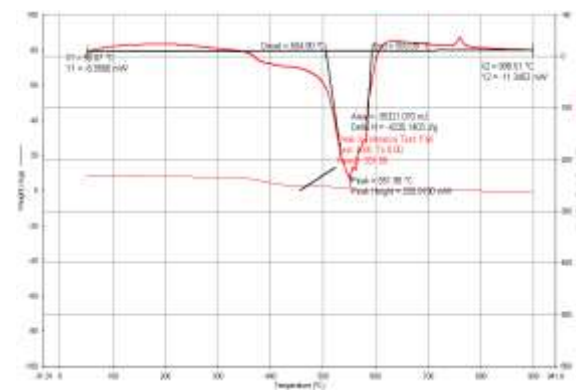


Figure 12 TG Analysis of the pure organic varnish

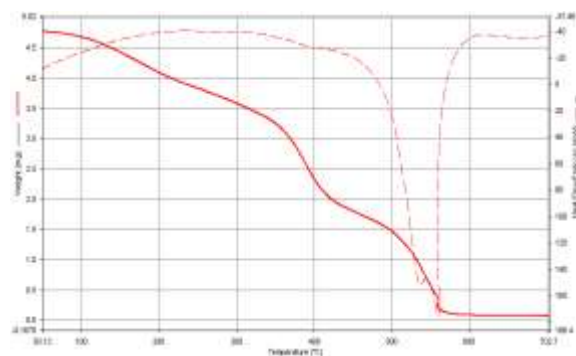


Figure 13 TG Analysis of the organic varnish mixed with 1 wt% of carbon nanotubes

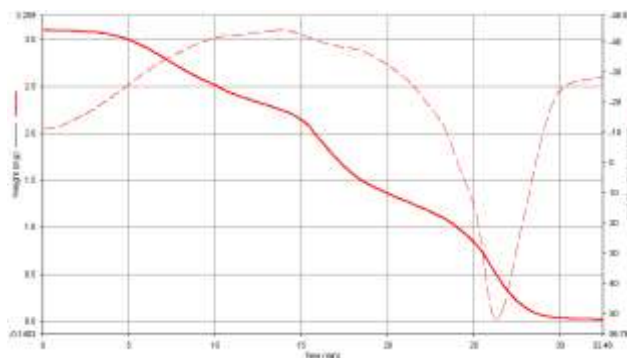


Figure 14 TG Analysis of the organic varnish mixed with 3 wt% of carbon nanotubes

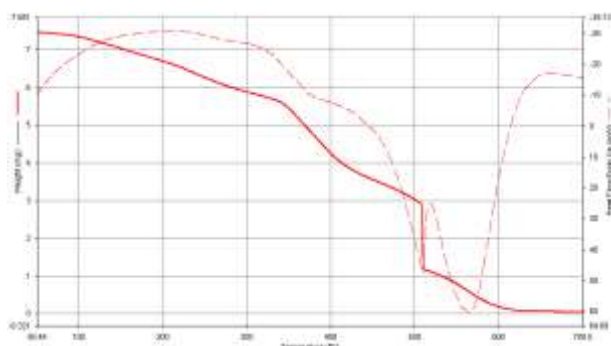


Figure 15 TG Analysis of the organic varnish mixed with 5 wt% of carbon nanotubes

From the above TG graphs, the onset temperature, the peak temperature and the end temperature of the organic varnish and the nano carbon filled enamel with various (1%, 3% and 5%) wt proportions were found and the readings were given in the Table 15.

**Table 15 the onset temperature, the peak temperature and the end temperature of the organic varnish and the carbon nanotubes filled organic varnish with various (1%, 3% and 5%) wt proportions**

Sample	On set temp (°C)	Peak temp(°C)	End temp (°C)	% Increase in On set temp	% Increase in Peak temp	% Increase in End temp
Pure	504.90	551.98	593.09	-	-	-
1%	517.76	569.59	595.16	2.54	3.19	0.34
3%	519.76	589.79	600.26	2.94	6.84	1.20
5%	531.26	595.63	609.30	5.22	7.90	2.73

## 5. CONCLUSION

It was observed from the table the PD inception voltage decreased with 32.49 %, 11.18 % and 9.07 % for 1 wt%, 3 wt% and 5 wt% carbon nanotubes filled enamel respectively from the PD inception

voltage of the enamel. Also the PD extinction voltage decreased in 44.15 %, 9.02 % and 9.02 % for 1 wt%, 3 wt% and 5 wt% carbon nanotubes filled enamel respectively from the PD extinction voltage of the enamel. Similarly it was also noted that the breakdown strength decreased by 25.39 %, 8.66 % and 7.48 % for 1 wt%, 3 wt% and 5 wt% carbon nanotubes filled enamel respectively from the breakdown strength of the enamel. From the thermal analysis the on set temperature was increased by 2.55 %, 2.94 % and 5.22 % for 1 wt%, 3 wt% and 5 wt% carbon nanotubes filled enamel respectively from the on set temperature of the enamel. Also it was observed that the peak temperature was increased by 3.19 %, 6.85 % and 7.91% for 1 wt%, 3 wt% and 5 wt% carbon nanotubes filled enamel respectively from the peak temperature of the enamel. Also it was noted that the peak temperature was increased by 0.35 %, 1.21 % and 2.73% for 1 wt%, 3 wt% and 5 wt% carbon nanotubes filled enamel respectively from the end temperature of the enamel.

## 6. ACKNOWLEDGMENT

We express our sincere thanks to the Ultimate God, the creator of this universe, our parents, brothers, sisters, friends, relatives, college management, colleagues, students, technicians, various authors, Indian Government, Tamil Nadu Government, IIT Bombay, IIT Madras, IIT Delhi, College of Engineering, Guindy, Mepco Schlenk Engineering College, Panimalar Engineering College, Sakthi Mariamman Engineering College, Dhanalakshmi Srinivasan College of Engineering and Technology, Loyola College, AC Tech, Madras University, Aurora Technological and Research Institute, Kamaraj College of Engineering and Technology, Sree Sowdambika College of Engineering, Anna University of Technology, Tirunelveli, National Engineering College and all the persons who have helped us directly and indirectly for our research work.

## 7. REFERENCES

- [1] Biro L.P., Z.E.Horvath, A.A.Koos, Z.Osvath, Z.Vertesy and L.Tapazto, (2003) "Direct synthesis of multi-walled and single walled carbon nanotubes by spray-pyrolysis", *Journal of Optoelectronics and advanced materials*, Vol.5, issue 3, pp 661- 666.
- [2] Couteau E., J.W. Seo , L Thien-Nga , Cs. Mik , R.Gaal, L.Forro, (2003) "CVD synthesis of high-purity multiwalled carbon nanotubes using CaCO<sub>3</sub> catalyst support for large-scale production" *Chemical Physics Letters* 378, pp 9-17.
- [3] Engel-Herbert R. a, H. Pforte b, T. Hesjedal, (2007) "CVD synthesis and purification of single-walled carbon nanotubes using silica-supported metal catalyst" *Materials Letters* 61, pp 2589-2593.
- [4] Giuseppe Gulino, Ricardo Vieira, Julien Amadou, Patrick Nguyen, Marc J. Ledoux, Signorino Galvagno, Gabriele Centi, Cuong Pham-Huu,(2005) "C<sub>2</sub>H<sub>6</sub> as an active carbon source for a large scale synthesis of carbon nanotubes by chemical vapour deposition" *Applied Catalysis A:General* 279, pp 89-97.
- [5] Guo. P.S. Z. Sun, Y.W. Chen, Z.H. Zheng (2006) "A novel approach to mass synthesis of raw CNTs for printed field emission cathodes by chemical vapour deposition" *Materials Letter*, Vol.60, pp 966-969.
- [6] Edison Selvaraj, D., C. Pugazhendhi Sugumaran, and A.Sivaprakash."Characterization of Electrical and Thermal Properties of Enamel Filled with Carbon Nanotubes." *Proceedings of the Third International Conference on Trends in Information, Telecommunication and Computing*. Springer New York, 2013.
- [7] Selvaraj, D. Edison. "Partial discharge characteristics of enamel filled with micro and nano composite of siO<sub>2</sub> and TiO<sub>2</sub>." *International Journal of Science and Engineering Applications* 1.2 (2012): 95-101.
- [8] Selvaraj, D. Edison. "Characterization of dielectric properties of the enamel filled with carbon nano tubes for the frequency range of 50 Hz-5 MHz" *International Journal of Science and Engineering Applications* 1.2 (2012): 102-106.
- [9] Selvaraj, D. Edison, and C. Pugazhendhi Sugumaran. "Comparative Analysis of Dielectric Properties of Enamel Filled with Various Nanofillers such as ZrO<sub>2</sub>, Al<sub>2</sub>O<sub>3</sub>, CNT and ZnO." *International Journal of Science and Engineering Applications* 1.1 (2012): 51-55.
- [10] Babu, B. Gurukarthik, D. Edison Selvaraj, R. Srinivas, B. Guru Prakash, and R. Vishnu. "Analysis of Relative Permittivity and Tan Delta Characteristics of Silicone Rubber Based Nano-composites." *International Journal of Scientific Engineering and Technology*, pp.2201-206, 2012.
- [11] Edison Selvaraj. D, Pugazhendhi Sugumaran. C, Lieutenant Ganesan. J, Ramathilagam. J, "Analysis of Dielectric and Thermal Properties of Polyamide Enamel Filled with Carbon Nanotubes" *International Journal of Nano science*, Vol.12, Issue 3, June 2013.
- [12] Lieutenant Ganesan. J, Edison Selvaraj. D, and Ramathilagam. J,"Experimental analysis of Thermal conductivity of enamel filled with micro and nano composite of SiO<sub>2</sub> and TiO<sub>2</sub>" *International journal of Advanced Research in Electrical, Electronics and Instrumentation Engineering*, Vol.2, Issue 7,pp. 2907-2912 , 2013.
- [13] Lieutenant Ganesan. J, and Edison Selvaraj. D, "Analysis of Thermal and Electrical Properties of Enamel Filled with Various Nano fillers such as ZrO<sub>2</sub>, Al<sub>2</sub>O<sub>3</sub> and CNT", *International Journal of Engineering Research*, Vol.2, Issue 2, pp. 182-186, 2013.

# Palmpoint and Handgeometry Recognition using FAST features and Region properties

Swapnali G. Garud<sup>1</sup>

Department of CS and IT,  
Dr. Babasaheb Ambedkar Marathwada  
University, Aurangabad, (M.S.), India.

K.V. Kale<sup>2</sup>

Department of CS and IT,  
Dr. Babasaheb Ambedkar Marathwada  
University, Aurangabad, (M.S.), India.

---

**Abstract:** Biometrics recognition system is more reliable and popular. In this paper we describe a palmpoint and handgeometry based person identification consisting of three main steps - preprocessing techniques such as morphological operations. The feature extraction techniques such as FAST feature algorithm and region properties is used to independently extract palmpoint and handgeometry features. Feature matching with euclidean distance classifier. These techniques are more reliable and faster than traditional techniques used. We finally conclude that the proposed methodology has better performance. This is supported by our experiments which are able to achieve recognition rate for palmpoint 100 % and for handgeometry 93.75 %.

**Keywords:** Multimodal, FAST features, Region properties, Euclidean

---

## 1. INTRODUCTION

In real life effective access control system is challenging task. The biometric authentication system becomes very popular because it uses behavioral and physiological characteristics to uniquely identify the individual [1]. Biometrics authentication system useful in various applications such as physical access control, security, monitoring which is more secured than traditional password based security systems because it is not proper practice each time to remember long passwords hence password based authentication system is referred as the weak authentication mode and the Biometrics can be employed on various traits like fingerprint, palmpoint, handgeometry, iris, face, voice, signature, etc which are unique for every individual hence are referred as strong authentication mode [2]. Biometrics system has two types i.e. verification systems and identification systems [3]. Many comparisons are required for this system. Biometrics is of three modes i.e. unimodal biometrics which can identify individual by using single trait. Second is bimodal biometrics in which identification is done with fusion of two modalities and the other is multimodal biometrics which uses combination of multiple traits for identification purpose of human. A unimodal biometric may fails to be accurate enough for the identification of a user population and there is one more possibility of failure if physical characteristics of a person for the selected biometric is not available. The chance of any two people having the same characteristic will be optimized by highly unique features [4]. By combining information from different biometrics modalities we can achieve higher and more consistent performance levels [5]. A multimodal biometric system requires an integration scheme to fuse information obtained from the individual modalities. Biometrics system performance depends on quality of image [6]. There are different level of fusion available in biometrics. Amongst that feature extraction level is widely used because many observers prove that this level fusion produces better

results. Usually, the performance of the biometric system is given by the accuracy of the system

In this paper new method is provided for personal authentication using palmpoint and handgeometry that are simultaneously acquired from a single hand image. The database contains images of subjects for left and right hand. Each of these palmpoint images are used to extract specific features. Thus the palmpoint and hand geometry features of an individual are obtained from the same hand image.

The palm is the inner surface of a hand between the wrist and the fingers. The palm has unique features and provides a larger area so the more distinctive features can be generated to improve the performance of recognition system. There are different features that exists on a palm such as principle line, wrinkle line, delta point. The feature of palmpoint is quite stable and specific because there is a little change in a long time. They can only be generated from a high resolution image, hard to be faked.

Hand Geometry gives the geometric structure of the hand. Hand geometry is suitable for integration with other biometrics. Hand Geometry is a biometric key with medium level of individualization. There are different features that can be extracted and used as key such as finger width and length, hand height, width, palm height, palm width, etc [7]. The feature of hand geometry is relatively simple and easy to use but it is not invariant due to a period of time.

The rest of the paper is organized as follows - Section II gives background of related work in literature. Section III gives proposed method which contains image acquisition, preprocessing, feature extraction techniques. Section IV discussed the experiments and results. Section V summarily devoted to conclusion. Section VI gives acknowledgement.

## 2. RELATED WORK

Slobodan Ribaric, et al [1] gives a bimodal biometric verification system for physical access control based on the features of the palmprint and the face, palm matching is based on the adapted HYPER method. And for face the K-L transform is used for matching. bimodal system can achieve an EER (equal error rate) of 3.08% for  $T=0.748$  and the minimum TER (total error rate) = 5.94% for  $T = 0.8$ . Antonia Azzini, et al [2] given idea about using a fuzzy control system to manage a multi-modal authentication system, checking the identity of a user during the entire session. The first biometric acquisition takes matching score 0.725 and the second biometric acquisition takes score 0.4860. Teddy Ko, [3] gives various scenarios in multimodal biometric systems using fingerprint, face and iris recognition, the levels of fusion that are possible and the integration strategies that can be adopted to fuse information and improve overall system accuracy. How the image quality of traits will affect the overall identification accuracy and the need of staffing for the secondary human validation. V. C. Subbarayudu, et al [4] proposed general working of multimodal biometrics system with Iris and Palmprint and fusion is done at the matching score level by Sum Rule technique with recognition rate is 96.6%. Andrew Teoh, et al [5] introduced k-Nearest Neighbourhood (k-NN) based classifiers are adopted in the decision fusion module for the face and speech experts with Recognition rate is 80.33%. Anil K. Jain, et al [6] described an automated fingerprint recognition system and listed key challenges and research opportunities in the field. The recognition rate is 95%. Fan Yang, et al [7] fingerprint, palm-print and hand-geometry are combined for person identity verification. Wavelet transform to extract the features from fingerprint and palm-print is used and hand-geometry feature (such as width and length) is extracted after the pre-processing phase. Feature level fusion and match score fusion together for identity. The weight values are calculated based on total minimum error. i.e. For  $weight_1 = 0.75, weight_2 = 0.25$ . X. Wu., et al [8] proposed a palm print recognition system by extracting features using Sobel operators and using Hidden Markov Models (HMM) as classifiers. Ajay Kumar, et al [9] attempts to improve the performance of palmprint-based verification system by integrating hand geometry features. These features are then examined for their individual and combined performances. The recognition rate is 98.3%.

Harpreet Singh, et al [10] have given iterative fuzzy approach for obtaining fused images Entropy values are provided in result as for Fuzzy algorithm entropy is 5.30 and for neuro fuzzy algorithm 4.89. Chun Wai Lau, et al [11] presents a multi-biometric verification system that combines speaker verification, fingerprint verification with face identification and equal error rates (EER) are 4.3%, 5.1% and the range of (5.1% to 11.5%) for matched conditions in facial image capture respectively. K. Ito, et al [12] suggested Multi-scale wavelet decomposition of palmprint images and using mean of each wavelet sub-block has been suggested.

M. Wang, et al [13] proposed 2D PCA and 2D LDA over conventional PCA have been reported to be better for palmprint recognition. V. Conti, et al [14] have proposed multimodal biometric system using two different fingerprints. The matching module integrates fuzzy logic methods for matching score fusion. Both decision level fusion and matching score level fusion were performed.

Kornelije Rabuzin, et al [15] had suggested active rules in fuzzy logic are used for effective decision making in person identification. The recognition rate is 97%.

Gawande, et al [16] used log Gabor filter can be used to extract the feature vectors from both Iris and Fingerprint and then they are concatenated. The phase data from 1 D log Gabor filters is extracted and quantized to four levels to encode the unique pattern

of Iris and Fingerprint into bitwise biometric template. Hamming distance (HD) is used to generate a final match score. Yong Jian Chin, et al [17] proposed a multimodal biometrics system in which 2D gabor filter is used to extract features. The recognition rate is 98%. Cheng Lu, et al [18] suggested idea which utilizes two or more individual modalities, like face, ear, and fingerprint, to improve the recognition accuracy by new dimensionality reduction method called Dimension Reduce Projection (DRP). The recognition rate is 95.8%. Nicolas Tsapatsoulis, et al [19] presented an identification and authentication system based on hand geometry which used POLYBIO hand database. The recognition rate is 95%.

Anil K. Jain, et al [20] given an overview of biometrics, emerging biometric technologies and their limitations, and examines future challenges. Mohammad Imran, et al [21] proposed a new hybrid approach to verification aspect of a multibiometrics system, comparative analysis with traditional approaches such as multialgorithmic and multimodal versions of the same. The average EER of hybrid approach from different levels of fusion is 3.87% which shows that hybrid approach yields lower average EER. Mohamed K. Shahin, et al [22] introduced a multimodal biometric system (MMBS) based on fusion of whole dorsal hand geometry and fingerprints that acquires right and left (Rt/Lt) near-infra-red (NIR) dorsal hand geometry (HG) shape and (Rt/Lt) index and ring fingerprints (FP). Accuracy rate is 99.71%. S. Palanikumar, et al [23] presented approach for enhancing palmprint image. The enhancement is based on curvelet which preserves the fine features without noise. The result gives high PSNR (Peak Signal-to-Noise Ratio) value for the Curvelet method. i.e. 38.1047.

Feifei CUI, et al. [24] proposed multimodal biometrics recognition based on score level fusion of fingerprint and finger vein. Recognition rate is 98.74%. Romaiissaa Mazouni, et al [25] proposed a comparative study of several advanced artificial intelligence techniques (e.g. Particle Swarm Optimization, Genetic Algorithm, Adaptive Neuro Fuzzy Systems, etc.) as to fuse matching scores in a multimodal biometric system is provided. The fusion was performed under three data conditions: clean, varied and degraded. Some normalization techniques are also performed prior fusion so to enhance verification performance. The population based techniques (PSO, GA) gave very good results. Nishant Singh, et al [26] presents an efficient multimodal biometric system based on 4 slap fingerprint images. The system utilizes 4 slap fingerprint scanner to simultaneously collect fingerprints of multiple fingers on a hand in one image. Decision threshold is 0.9869 and FAR is 5.08%. Ashutosh Kumar, et al [27] suggested the new approach where the palmprint images are mapped to Eigen-space and a robust code signature is generated from different camera snapshots of the same palm to incorporate tonal and lighting variations. To enable real-time identification, the signature is represented by a low dimensional feature vector to reduce computational overheads. P.U. Lahane, et al [28] given the comparison of data base template and the input data is done with the help of hamming-distance matching algorithm. If the templates are matched we can allow the person to access the system. Gabor filter is used for fingerprint.

Krishneswari, et al [29] proposed to investigate the performance of multimodal biometrics using palm print and fingerprint. Features are extracted using Discrete Cosine Transform (DCT) and attributes selected using Information Gain (IG). Results shows an average improvement of 8.52%. D. Y. Lilianna, et al [30] studied about biometrics of palm for identification system using block-based line detection for palm print feature extraction process, and chain code solved the hand geometric feature extraction. We combined those two respective features and recognized it using Dynamic Time Warping (DTW) method which was able to measure the distance between two different features. The accuracy rate is 89%. Gawande, et al [31] gives use of the log Gabor filter to extract

the feature vectors from both Iris and Fingerprint and then they are concatenated. Finally the phase data from 1 D log Gabor filters is extracted and quantised to four levels to encode the unique pattern of Iris and Fingerprint into bitwise biometric template. Hamming distance (HD) is used to generate a final match score. Experimental results was verified on database of 50 users accounting to FAR = 0% and FRR = 4.3%. M. Dale, et al [32] presented palm texture using transform features and hand geometry features are represented as distances between different boundary points. The final decision is made by fusion at decision level. S. Rao, et al [33] suggests image fusion using fuzzy and neuro fuzzy logic approaches utilized to fuse images from different sensors, for enhancing visualization. Mohammad Abdolahi, et al [34] proposed two biometric traits such as iris and fingerprint which uses Decision level fusion and Fuzzy logic as technic for the effect of each biometric result combination. Recognition rate is 71%.

There are many challenges in traditional system such as they requires more time for recognition. This research tried to overcome this problem by suggesting new algorithm for finding the features of palm which is very much faster with higher recognition rate.

### 3. PROPOSED METHOD

The proposed method includes various steps such as image acquisition from sensor, preprocessing operation to enhance the quality of image and feature extraction process to identify the features of an image. Finally, matching is done on the basis of specific features with database image and decision is made for identification.

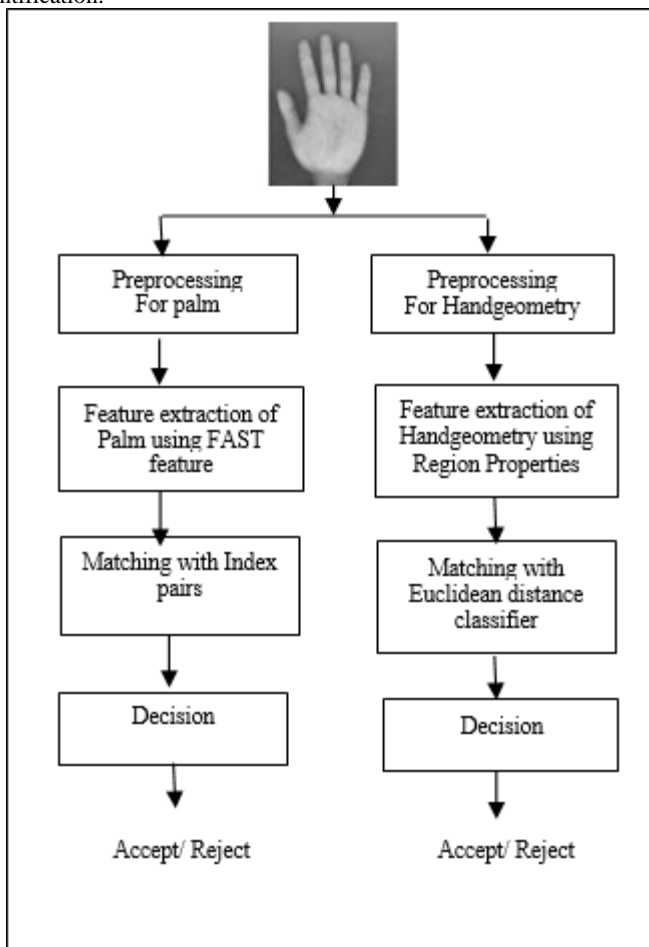


Figure 1. Block diagram of proposed system

The figure 1 shows the block diagram of proposed biometrics identification system.

### 3.1 Image Acquisition

We used KVCR Multimodal Biometrics database<sup>#</sup> This database contains images of different modalities such as palm , handgeometry, fingerprint, iris, face, voice, signature, HRV, knuckle, etc. of 150 subjects which belongs to age group of 20 to 30 years old . Out of which data for 7 subjects is used in this experiment. From this total 112 images for palmprint and 112 images for handgeometry of 7 subjects.

For extraction of palmprint images whole handgeometry images are employed. Palmprint images are acquired from the center of rectangle that can enclose the whole area of interest in palm. These center coordinates are used to extract a square palmprint region of fixed size. Out of these total 112 images of palmprint from database 8 images for left and right hand i.e. 16 images of every subject.

For extraction of handgeometry images we used Laserjet scanner and they are of JPEG format. The users were only requested with two preconditions first is their fingers do not touch each other and second is most of their hand touches the scanner surface. Handgeometry database is collected. We used total 112 images of handgeometry from database 8 images for left and right hand. i.e. 16 images for each subject.

### 3.2 Preprocessing techniques

For palmprint images we used center region of handgeometry images of specific size. These images are also colored images and we convert them firstly into grayscale images. Then specific threshold value is set for images for further processing.

For handgeometry images we used color hand images and they are firstly converted into grayscale format. Then we used morphological opening to estimate the background illumination. The opening operation has the effect of removing objects that cannot completely contain the structuring element. Then grayscale image converted into a binary image by using thresholding. After that background noise is removed. Then we found all the connected components in the binary image. The size of the objects has major concern in the accuracy of results.

### 3.3 Feature extraction techniques

For palmprint we extracted features such as corners points in grayscale images with the Features from Accelerated Segment Test (FAST) algorithm to find feature points. From these corner points interest point descriptors are extracted. These corner points are common for both images in the form of *Index Pair*. This algorithm also gives value of total number of Index pairs in images. Greater the value of index pair indicates that the images belongs to same subject and smaller value of index pair shows that the images belongs to different subject. The descriptors are extracted feature vectors and their corresponding locations, from a binary or intensity image. The function derives the descriptors from pixels surrounding an interest point. These pixels describe and match features specified by a single-point location. Each single- point specifies the center location of a neighborhood. The method used for descriptor extraction depends on the class of the input points such as SURFpoints, MSERobjects, corner points. FASTfeatures technique uses parameters as image, name and its scalar threshold value in the range (0,1). Name is MinContrast . It gives minimum intensity difference between corner and surrounding region, specified as the

comma-separated pair consisting of MinContrast. The minimum intensity represents a fraction of the maximum value of the image class. Increasing the value reduces the number of detected corners. The default value is 0.2. A standard threshold value used in this experiment is 0.031 because at this particular threshold value we get maximum number of matching index pairs in images.

**Table 1. Feature matrix palmprint palmprint images for Left hand**

Sub	Index Pair1	Index Pair2	Index Pair3	Index Pair4	Index Pair5	Index Pair6	Index Pair7
Sub1	31.6	33	31	29.4	24.14	29.6	27.4
Sub2	16.9	31	33.8	26.3	41.12	41.4	31.6
Sub3	18.6	17.37	65	69.6	7	18.8	17.8
Sub4	15.5	15.12	5.12	5.5	11.25	10.8	56.5
Sub6	2.62	4.87	3.25	3.25	3.62	3.25	4
Sub7	1.5	1.25	1.63	1.75	1.12	2	2.37

**Table 2. Feature matrix palmprint palmprint images for Right hand**

Sub	Index Pair1	Index Pair2	Index Pair3	Index Pair4	Index Pair5	Index Pair6	Index Pair7
Sub1	23.38	25.50	90.50	11.50	33.13	28.00	7.88
Sub2	16.88	31.00	33.75	26.25	41.13	41.38	31.63
Sub3	5.13	5.00	8.25	7.50	8.38	9.88	9.63
Sub4	23.63	21.25	14.25	15.75	12.75	15.25	24.25
Sub5	9.88	15.00	19.63	14.75	20.25	16.25	15.00
Sub6	10.88	12.75	14.63	12.63	15.75	13.88	14.50
Sub7	3.25	3.25	2.63	3.25	4.38	1.38	0.63

For handgeometry we extracted features by using the region properties which measures properties of image regions. In this experiment we extracted features such as area, boundingbox, height of hand, perimeter, majoraxislength, minoraxislength by using the region properties of connected component of binary image of hand. The connected component gives the number of pixels. The area feature gives the actual number of pixels in the region. The perimeter gives distance around the boundary of the region. The Boundingbox gives smallest rectangle containing the region. It also gives the height of region. The majoraxislength specifies the length of the major axis of the ellipse that has the same normalized second central moments as the region and minoraxislength gives the length of the minor axis of the ellipse that has the same normalized second central moments as the region. By all these region properties we can easily discriminate the features of different images. First 6 samples were considered as training samples and mean is taken for those samples for all images for each subject. And remaining 2 samples of all features of each subject is considered as testing sample. In table 3 and 4 F1– F6 shows feature 1 to feature 6.

**Table 3. Feature matrix handgeometry images for Left hand**

Sub	Area	Perimeter	Bounding Box	height	Major Axis length	Minor Axis length
	F1	F2	F3	F4	F5	F6
Sub1	737798.83	11950.85	1413.83	1405.67	1341.01	934.16
Sub2	450250.50	7575.32	1137.17	1126.33	1057.40	770.87
Sub3	395181.33	6495.84	1031.83	1031.83	982.47	690.55
Sub4	459746.50	7010.65	1109.33	1109.33	1084.23	758.53
Sub5	409272.83	7206.35	1117.83	1055.33	980.00	774.93
Sub6	447932.83	6273.44	1114.33	1114.33	1062.16	703.51
Sub7	432571.67	8010.98	1020.00	1020.00	1022.54	766.52

**Table 4. Feature matrix handgeometry images for Right hand**

Sub	Area	Perimeter	Bounding Box	height	Major Axis length	Minor Axis length
	F1	F2	F3	F4	F5	F6
Sub1	746972.50	12162.86	1420.25	1412.67	1338.32	981.31
Sub2	460402.17	7306.92	1116.75	1114.83	1074.19	782.85
Sub3	402758.67	6349.36	1008.00	1008.00	982.88	728.61
Sub4	445831.17	6822.90	1156.67	1086.67	1038.19	811.78
Sub5	403517.67	6064.52	1015.50	1015.50	952.13	752.21
Sub6	444826.33	6331.65	1109.33	1109.33	1063.97	709.75
Sub7	457211.83	7846.00	1068.67	1068.00	1064.75	788.66

## 4. EXPERIMENT AND RESULT ANALYSIS

### 4.1 Palmprint Recognition

In palmprint we used 112 images for 7 subject of both left and right hand. From 112 we used 98 for training and remaining 14 for testing matrix. We test at least two images at a time for palm. By comparing results of these two images we can easily recognize the particular subject. If the image sample belongs to same person then the both image contains maximum no of matching corner points in common called as index pair. If the images doesn't belongs to same person then they have no matching points in common or negligible matching points in common. We can compare the test image against no of images at the same time with this process. The resultant matrix contains total no of index pairs for each pair of tested image samples. This test gives appropriate idea about the test sample belongs to which subject. Afterwards this matrix for further analysis and ease of use is reduced to the classification matrix which contains the total no of samples correctly classified in particular class for each subject. And 'x' entry indicates that no match in corresponding class. The table 14 shows classification matrix for palmprint samples.

**Table 5. Classification matrix for palmprint samples**

Test Sample	Sub1	Sub2	Sub3	Sub4	Sub5	Sub6	Sub7
	Class-1	Class-2	Class-3	Class-4	Class-5	Class-6	Class-7
Sub1-8	8	x	x	x	x	x	x
Sub2-8	x	8	x	x	x	x	x
Sub3-8	x	x	8	x	x	x	x
Sub4-8	x	x	x	8	x	x	x
Sub5-8	x	x	x	x	8	x	x
Sub6-8	x	x	x	x	x	8	x
Sub7-8	x	x	x	x	x	x	8

**Table 6. Recognition rate for palmprint samples**

Sub	Total no of sample tested	Correct classified	Miss Classified	RR
Sub1	8	8	0	100%
Sub2	8	8	0	
Sub3	8	8	0	
Sub4	8	8	0	
Sub5	8	8	0	
Sub6	8	8	0	
Sub7	8	8	0	

From table 6 it is observed that all samples of palmprint are classified into corresponding classes correctly. So the recognition rate achieved for palmprint images is 100 %.

## 4.2 Handgeometry Recognition

In Handgeometry we used 112 images for 7 subjects of both left and right hand. From 112 we used mean of 6 samples of each subject for every feature and remaining 14 images for testing matrix. First we calculate the feature matrix then the pairwise Euclidean distance between training matrix and testing matrix is calculated. Mean of each sample is tested with 7 and 8<sup>th</sup> sample of each image. The resulting distance matrix for left hand as shown in table 7.

**Table 7. Distance matrix for handgeometry images of Left hand**

Sub	Sub1	Sub2	Sub3	Sub4	Sub5	Sub6	Sub7
S1 7	3237.69	284436.30	339515.14	274949.03	325415.50	286773.03	302109.23
S1 8	17642.45	269940.60	325020.00	260454.83	310919.47	272280.03	287612.29
S2 7	288754.75	1172.74	53907.36	10682.52	39806.82	1721.05	16513.26
S2 8	289191.26	1609.56	53471.03	11120.40	39370.11	1491.84	16075.74
S3 7	339392.12	51818.33	3499.28	61318.70	10856.12	49523.31	34139.46
S3 8	337535.79	49961.16	5259.06	59461.28	8999.66	47665.82	32282.82
S4 7	292207.52	4688.19	50465.13	14187.68	36358.05	3059.86	13046.86
S4 8	276100.54	11538.08	66569.02	2038.75	52480.42	13822.00	29211.19
S5 7	335803.32	48226.07	6876.59	57706.79	7308.97	45886.49	30583.64
S5 8	335730.56	48152.09	6942.57	57634.28	7224.00	45815.24	30506.56
S6 7	289863.07	2610.67	52811.37	11778.10	38730.75	59.76	15519.36
S6 8	291362.45	3974.38	51311.28	13274.46	37230.76	1440.89	14027.66
S7 7	301822.19	14271.89	40858.93	23784.26	26749.88	12110.10	3442.39
S7 8	300478.63	12928.42	42200.41	22440.85	28091.65	10782.82	4780.39

The resulting distance matrix for Right hand as shown in table 8.

**Table 8. Distance matrix for handgeometry images of Right hand**

	Sub1	Sub2	Sub3	Sub4	Sub5	Sub6	sub7
s1 7	2827.65	289439.45	347091.15	304016.61	346337.18	305030.39	292620.94
s1 8	6749.81	293344.99	350996.60	307922.52	350243.05	308937.07	296525.46
s2 7	281275.92	5336.18	62987.84	19914.99	62234.53	20939.23	8536.34
s2 8	280999.01	5613.05	63264.75	20191.78	62511.40	21215.72	8813.11
s3 7	351933.35	65321.54	7670.70	50745.85	8434.56	49738.64	62142.12
s3 8	353353.04	66741.43	9091.93	52166.19	9857.04	51159.67	63561.14
s4 7	299450.68	12840.31	44813.59	1791.90	44061.72	2899.73	9666.54
s4 8	299450.68	12840.31	44813.59	1791.90	44061.72	2899.73	9666.54
s5 7	349192.71	62581.19	4936.45	48003.67	5683.09	46992.86	59405.81
s5 8	346047.70	59436.10	1800.04	44858.69	2538.74	43848.39	56260.68
s6 7	302660.69	16069.11	41612.90	1589.54	40853.96	472.40	12945.52
s6 8	303024.01	16432.60	41249.96	1934.73	40490.88	831.17	13308.07
s7 7	288547.06	2152.80	55725.87	12699.12	54977.75	13757.05	1295.92
s7 8	283429.18	3458.70	60852.15	17833.70	60105.59	18888.69	6411.07

In table 7 and table 8 highlighted cells indicate the correctly classified values and highlighted values indicates the misclassified values.

Total 32 samples are tested for handgeometry. Out of which 30 are correctly classified and 2 are misclassified. The reason for miss-classification is the poor quality of images.

**Table 9. Recognition rate for Handgeometry**

Test	Total no of sample tested	Correct classified	Miss classified	RR
Left hand	16	15	1	93.75 %
Right Hand	16	15	1	93.75 %
Total	32	30	2	93.75 %

**Table 10. Overall Recognition rate for palmprint and handgeometry**

Test	Total no of sample tested	Correct classified	Miss classified	RR
Palm	56	56	0	100 %
Hand	32	30	2	93.75%

Figure 2 shows the Receiver Operating Characteristic curve for palmprint images and Figure 3 ROC curve for handgeometry images. The ROC is based on observed frequency and cumulative frequency. Performance True positive rate and false positive rates are analyzed with the ROC.

ROC Curve for  $y = 0.01\ln(x) + 1$   
 Area under curve = 0.9902

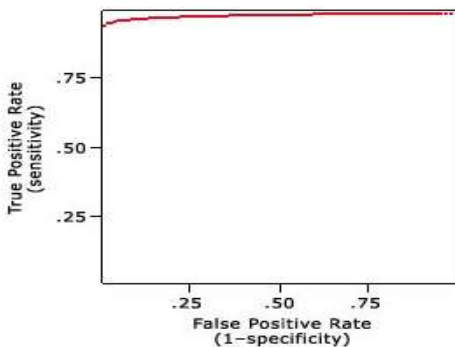


Figure 2. ROC curve for palmprint

ROC Curve for  $y = 0.01\ln(x) + 1$   
 Area under curve = 0.9902

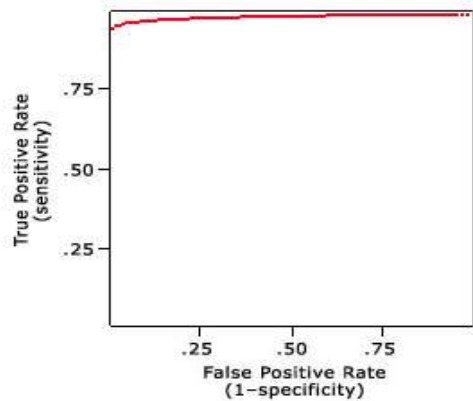


Figure 3. ROC curve for handgeometry

## 5. CONCLUSION

This paper presents palm and handgeometry recognition based on FAST features and region properties. The results clearly indicates the significance of the method used in this research work. For palmprint recognition the FAST features were utilized for classification for palm into appropriate classes. The observed classification success is 100%. The results of handgeometry recognition was improved and achieved 93.75 % recognition. These two methods can be collectively used for development of multimodal biometric recognition system in very effective way.

This work is more reliable because it gives faster results as compare to traditional biometric techniques. For palmprint recognition the new approach FAST feature algorithm reduces number of comparisons and provides easy recognition rate because it gives direct discrimination between image samples.

## 6. ACKNOWLEDGEMENT

We would like to acknowledge and thanks to University Grants Commission (UGC), India for providing facility UGC SAP (II) DRS Phase – I F. No. 3-42/2009 Biometrics: Multimodal System Development Laboratory.

## 7. REFERENCES

- [1] Slobodan Ribaric, Ivan Fratric, and Kristina K. 2007 **A Biometric Verification System Based on the Fusion of Palmprint and Face Features**. Department of Electrical Engineering and Computing, University of Zagreb, Croatia.
- [2] Antonia Azzini, Ernesto Damiani, Stefania Marrara, 2007 **Ensuring the identity of a user in time: a multi-modal fuzzy approach**. IEEE International Conference on

Computational Intelligence for Measurement Systems and Applications Ostuni, Italy,

- [3] Teddy Ko 2005 **Multimodal Biometric Identification for Large User Population Using Fingerprint, Face and Iris Recognition**. **IEEE transaction** Proceedings of the 34th Applied Imagery and Pattern Recognition Workshop.
- [4] V C Subbarayudu, Munaga V, N K Prasad, 2008 **Multimodal biometrics system**. Proceeding IEEE transactions.
- [5] Andrew Teoh, S. A. Samad and A. Hussain, 2004 **Nearest Neighbourhood Classifiers in a Bimodal Biometric Verification System Fusion Decision Scheme**. Journal of Research and Practice in Information Technology, 36 (1).
- [6] Anil K. Jain, Jianjiang Feng, Karthik Nandakumar, 2010 **Biometrics : Fingerpoint Matching**. Published by the IEEE Computer Society 0018-9162 .
- [7] Fan Yang, Baofeng Ma. 2007 **A New Mixed-Mode Biometrics Information Fusion Based-on Fingerprint, Hand-geometry and Palm-print**. IEEE transactions Fourth International Conference on Image and Graphics.
- [8] X. Wu, K. Wang, Zhang D. 2004 **HMMs based palmprint identification** LNCS 3072, pp. 775-781.
- [9] Ajay Kumar, David C. M. Wong, Helen C. Shen, Anil K. Jain. 2004 **Personal verification using Palmprint and Hand Geometry Biometric**. Department of Computer Science, Hong Kong University of Science and Technology, Clear Water Bay, Hong Kong.
- [10] Harpreet Singh, Jyoti Raj Gulsheen Kaur , Thomas Meitzler 2004 **Image Fusion using Fuzzy Logic and Applications**. Proceeding IEEE transactions.
- [11] Chun Wai Lau, Bin Ma, Helen M. Meng, Y.S. Moon and Yeung Yam 2005 **Fuzzy Logic Decision Fusion in a Multimodal Biometric System** The Chinese University of Hong Kong, Hong Kong SAR, China.
- [12] K. Ito, T. Aoki, H. Nakajima, K. Kobayashi, T. Higuchi 2006 **A palmprint recognition algorithm using phase based image matching**. Proceedings of the ICIP, pp. 2669-2672.
- [13] M. Wang, Q. Ruan. 2006 **Palmprint recognition based on two dimensional methods**. Proceedings of ICSP.
- [14] Conti, G. Milici, P. Ribino, F. Sorbello and S. Vitabile 2007 **Fuzzy Fusion in Multimodal Biometric Systems**. university of 90127 Palermo, Italy.
- [15] Kornelije Rabuzin, Miroslav Ba., Markus Schatten, 2008 **Fuzzy Active Rules in Mutimodal Biometric Systems**. Proceedings of the ITI 2008 30th Int. Conf. on Information Technology Interfaces.
- [16] Gawande U., Sreejith R Nair, Harsha Balani, Nikhil Pawar & Manjiri Kotpalliwar 2009 **High Speed Frequency Multimodal Biometric System Using Iris and fingerprint**. Proceeding Springer.
- [17] Yong Jian Chin, Thian Song Ong, Michael K.O. Goh and Bee Yan Hiew 2009 **Integrating Palmprint and Fingerprint for Identity Verification**. IEEE Third International Conference on Network and System Security.
- [18] Cheng Lu, Di Liu\*, Jisong Wang, Shuyan Wang 2009 **Multimodal Biometrics Recognition by Dimensionality Reduction Method**. Second International Symposium on Electronic Commerce and Security.
- [19] Nicolas Tsapatsoulis and Constantinos Pattichis 2009 **Palm geometry biometrics : A score-based fusion Approach**. Proceedings workshop AIAI.
- [20] Anil K. Jain, Ajay Kumar 2010 **Biometrics of Next Generation: An Overview**. proceedings SECOND GENERATION BIOMETRICS' SPRINGER
- [21] Mohammad Imran , Ashok Rao , Hemantha Kumar G. 2011 **A New Hybrid approach for Information Fusion in Multibiometric Systems**. Proceedings IEEE transactions .
- [22] Mohamed K. Shahin, Ahmed M. Badawi, and Mohamed E. M. Rasmy 2011 **Multimodal Biometric System Based on Near-Infra-Red Dorsal Hand Geometry and Fingerprints for Single and Whole Hands**. World Academy of Science, Engineering and Technology 56.
- [23] S. Palanikumar, M. Sasikumar and J. Rajesh 2011 **Palmprint Enhancement Using Discrete Curvelet Transform**. International Journal of Computer Science Issues, 8(4), No 2.
- [24] Feifei CUI, Gongping Yang 2011 **Level Fusion of Fingerprint and Finger Vein Recognition**. Journal of Computational Information Systems, 7(16) pp. 5723-5731.
- [25] Romaisaa Mazouni, Abdellatif Rahmoun 2011 **On Comparing Verification Performances of Multimodal Biometrics Fusion Techniques**. International Journal of Computer Applications (0975 – 8887), 33(7).
- [26] Nishant Singh, Kamlesh Tiwari, Aditya Nigam and Phalguni Gupta 2012 **Fusion of 4-Slap Fingerprint Images with Their Qualities for Human Recognition**. IEEE transactions IEEE .
- [27] Ashutosh Kumar, Ranjan Parekh 2012 **Palmprint Recognition in Eigen-space**. International Journal on Computer Science and Engineering (IJCSE) ISSN : 0975-3397, 4(1).
- [28] P.U. Lahane, Prof. S.R. Ganorkar 2012 **Efficient Iris and Fingerprint Fusion for Person identification**. International Journal of Computer Applications (0975 – 8887), 50(17).
- [29] Krishneswari, K. and S. Arumugam 2012 **Multimodal Biometrics using Feature Fusion**. Journal of Computer Science, 8 (3), 431-435.
- [30] D. Y. Liliana, Eries Tri Utaminingsih 2012 **The combination of palm print and hand geometry for**

**biometrics palm recognition.** International Journal of Video & Image Processing and Network Security IJVIPNS-IJENS, 12(1).

- [31] Gawande U. , Sreejith R Nair, Harsha Balani, Nikhil Pawar & Manjiri Kotpalliwar 2012 **A High Speed Frequency Multimodal Biometric System Using Iris and fingerprint.** International Journal on Advanced Computer Engineering and Communication Technology (IJACECT) ISSN : 2278-5140, 1(2).
- [32] M. P. Dale, M. A. Joshi, H. J. Galiyawala 2012 **A Single Sensor Hand Geometry and Palm Texture Fusion for Person Identification.** International Journal of Computer Applications (0975 – 8887), 42(7).
- [33] Srinivasa Rao D, Seetha M, Krishna Prasad MHM **Comparison Of Fuzzy And Neuro Fuzzy Image Fusion Techniques And Its Applications.** International Journal of Computer Applications (0975 – 8887), 43(20).
- [34] Mohamad Abdolahi, Majid Mohamadi, Mehdi Jafari, 2013 **Multimodal Biometric system Fusion Using Fingerprint and Iris with Fuzzy Logic.** International Journal of Soft Computing and Engineering (IJSCE) ISSN: 2231-2307, 2(6).
- [35] Swapnali G. Garud, Apurva D. Dhawale, Mazhar Kazi, Y.S.Rode, S.B.Dabhade, K.V.Kale, 2014 **Fingerprint and Palmprint Recognition using neighborhood operation and FAST features.** International Journal of Computer Application (IJCA) ISBN: 973-93-80882-12-4, 95(12).

## 8. ANNEXURE

The KVCR Multimodal Biometrics database is designed by research team from Biometrics Research Lab situated in Dept. of Computer Science and IT, Dr. B.A. M. Univeristy, Aurangabad, (M.S.) , India . under the guidance of Prof. Dr. K.V. Kale, Head, Dept of Computer Science and IT, Dr. B. A. M. University, Aurangabad. The author is one member of these research team.

# How is Mortgage Lending Influencing the Economic Growth in Albania

Iris Shahini  
Alpha Bank  
Tirane, Albania

**Abstract**— Banks in Albania have been playing an important role in providing credit to the households especially to the housing sector and thereby contributing to the aggregate demand in the sector. Moreover, Albanian banks also extend various types of loans against the individuals and corporate before the financial crisis. After the crisis the banks become more restricted due to increase of non-performing loans as well as the macroeconomic volatility which is higher in emerging economies like Albania. In my study I will focus on the influence of mortgage loans and nonperforming loans in the country economic growth during the interval 2008-2013 that corresponds with the after crisis period.

**Keywords** — economic growth, housing loans, housing market, nonperforming loans, GDP

## 1. INTRODUCTION

Banking system stability is important for the development of a country. The bank's role can be said to be a catalyst for economic growth. The activity and performance of the banking industry is an indicator of financial stability. The rate at which banks finance public productive activities accelerates economic growth and ensures long-term sustainability. First of all, mortgage loans represent the main part of retail loans. Secondly, the default in payments of mortgage loans do not impact only the owners of the properties but also banks that use these properties as collaterals. Moreover, through the second market products as MBS, risk is spread all over the economy. During the last years the impact of financial crisis shrink the willingness of banks to lend and made them more conservative in terms of credit standards. Up to the year 2008, banks especially the Greek once, were much more aggressive in lending of housing loans mainly in foreign currency. The financial crisis lead to the depreciation of Albanian currency towards EUR and Albanian banks started to orient the customers to have the loan in the same currency as their incomes in order to avoid the exchange rate risk. On 2009 the loan in euro composed 72% of the total loan portfolio. As per constructors, there are the banks that supply the economy with money and the decrease in selling of properties is a consequence of loan supply from banks side considering that the individuals that buy an apartment in cash are very few in number. The aim of this study centered on how the mortgage loans and nonperforming loans influence the economic growth in Albania. The period under consideration is the one corresponding with the financial crisis 2008-2013.

## 2. LITERATURE REVIEW

As personal income rises or the burden of debt declines, the demand for mortgage funds should increase. In the models on credit demand, real GDP, prices and interest rates are commonly the explanatory variables, although there is no "standard" model which would be widely used. However, modeling and estimation techniques in this area are complicated due to difficulties with separating demand side effects from supply side effects (see e.g. Rajan 1994). Empirically, the relationship between credit and current

economic activity is well founded in Hofmann (2001) documents in 16 industrialized countries. The annual rate of change in real credit is closely related to that of real GDP. Erjona Suljoti and Gent Hashorva (2011) studied the impact of mortgage loans in the residential prices, GDP per capita and interest rate in the demand for mortgage loans. The correlation between the independent variables and the depended one was very strong for the period 1998-2010. GDP per capita and residential prices are positively correlated with the demand of housing loans from individuals and interest rate is negatively correlated. Festic, Kavkler, Repina (2011) confirmed that changes in macroeconomic conditions are translated into changes in the quality of bank loan portfolios.

### 2.1 Mortgage market and mortgage lending in Albania

The dwelling market as well as the housing loan market in Albania has experienced many changes. The developments in these two markets can be divided in two time periods. During the first period 2000-2007 a very fast development of dwelling market and mortgage loans market has occurred. Meanwhile during the period 2008-2012 the increase in both markets has slowed down due to the global financial crisis and the slow-down of economic activity in Albania( see table 1 and 2).

**Table 1. Economic growth in Albania (annual %)**

2007	2008	2009	2010	2011	2012	2013
5.9	7.5	3.3	3.8	3.1	1.62	0.4

Source: INSTAT

**Table 2: GDP/Capita in PPS**

2007	2008	2009	2010	2011	2012	2013
23	26	28	27	30	30	30

Source: Eurostat

Even though it was not expected to be so fast, the crisis in the real estate market had started based on the official data of Bank of Albania and real estate agencies which were not satisfied with the transactions of last period in the real estate market in 2008. Based on the statistic that these agencies published in the "Albania" newspaper it was obvious that the demand for house purchase from emigrants has been considerably decreased. Such evidence has been confirmed also from the Bank of Albania. The decrease for housing purchase from individuals has started since 2008 due to the difficult financial situation and low remittances from emigrants. Another factor influencing in the tendency of individuals to purchase a house is the loan financing. In 2008 banks started to be more restricted in lending mainly due to the increase of non-performing loans. The difficulty in having a loan will influence the market considering that the construction sector and industry absorb 77% of the total loan portfolio which is used to finance the investments in real estate. While the increase in house price was justified with the increase of construction materials as per BOA report. The macroeconomic environment, business difficulties as well as the restrictive decisions of BOA towards the second level banks have influenced in the decrease of loan supply. In Albania the individuals buy a house for living purpose rather than investment one so the decrease demand is much lower than in Europe or USA. Almost 70% of purchases are done through bank financing and only 30% are done in cash.

## 2.2 The trend of housing loans in Albania

During the period 2004-2007 the mortgage loans portfolio has experienced a high increase with an average annual increase of 65%. Such a positive trend has been sustained from the banking system development and economic growth of the period. It was created a stratum with average income having the possibility to meet the monthly obligations towards banks. On the same time the privatization of ex Saving Bank occurred, the biggest bank in Albania, named Raiffeissen Bank which gave liquidity to the market and stimulated banks to announce a new product, the "mortgage Loan". On the supply side of mortgage loans, banks used to gain market share by offering very convenience products. Many banks used the mortgage loan to diversify their loan portfolio in terms of quality and cost of funds. The willingness of banks to develop this market segment went along with the increase of individuals demand to be financed. Such an increase was due to the increase of housing prices during the years 2004-2007 which was not affordable to be paid in cash from the buyers. During this period the housing price were about 50% higher than in 2004. The mortgage loan portfolio for individuals composes almost 20% of the banking system loans portfolio. The product for housing financing may have a fix interest rate or a floating one. The interest rates also differ as per product currency. In general, most of the loans financing are in euro with floating interest rates. In any case some hybrid products have resulted to be successful in the market by having a fix interest rate for the first 2-5 years and floating for the remaining period. Banks in Albania finance up to 80% of the collateral market value and the tenor vary from 5 to 30 years. The demand for housing loans on 2007 and beginning of 2008 was higher than the demand of individuals for consumer

loans. Despite the necessity of individuals to be financed for house purchase other factors that have positively contributed in the demand for housing loans were: the developments in real estate market, consumer's confidence and credit policies applied from banks. Credit policies standards have been somehow tighten on the fourth quarter of 2009 through increasing the spread for the high risk loans, following the same trend as European banks. The demand in the same time decreased although the new buildings constructed were 1,021 in total. New disbursements during the year 2009 suffered a considerable decrease from 35,948 million ALL in 2008 to 15,146 million ALL. Although 2010 the credit policy standards in general were tightened, for housing loans they became more soothing compared with the year 2009. Two main factors that make banks to be conservative in lending are the non performing loans and low income of individuals

## 2.3 Nonperforming loans in the banking system

The increase of nonperforming loans in the banking system has been an important factor in the restriction of loan procedures for individuals and even for businesses.

Credit risk dominates the risk profile regardless the careful credit process of banks. The credit risk originating from the loan portfolio of banks remains the main risk with a direct effect on the financial stability of the banking sector. Regardless the contraction in crediting and the recent tendencies of the banks to deploy a great amount of their funds in safe actives, the credit risk remains dominant in the risks profile of the banking sector even during the second half of year 2013. During the second half of year 2012, nonperforming loans in the banking sector increased in 130 billion ALL, from 121 billion ALL in the first half and 160 billion ALL in the second half of 2011. Nevertheless, the pace of growth of nonperforming loans has slowed down from quarter to quarter. There was a slight improvement in the loans stock in the last quarter of the year with 0.95%. The deceleration of nonperforming loans reflects the increase of the bank's efforts to collect money. At the end of 2012, the ratio of nonperforming loans to the total loans increased from 21.1% to 22.5% in the first half of 2012 and from 18.8% in the same period of the previous year. The highest amount of nonperforming loans was on the second quarter of 2013 with a rate of 24.34% in the third quarter and 23.22% in the last quarter of 2013.

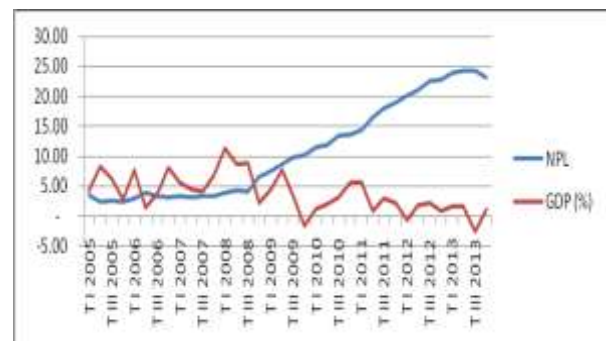


Figure 1: The trend of NPL and GDP ( in %)

### 3. METHODOLOGY AND DATA

The purpose of this paper is to describe the relation between the mortgage loans and nonperforming loans as a dependent variable and the economic growth as in depended variable. The period taken in consideration is 2008 up to 2013 corresponding with the beginning of the financial crisis. The data have been taken from different sources as Bank of Albania , Ministry of Finance, Albanian Association of banks etc. The time series of these data are on quarterly basis.



Figure 2: Mortgage loans in million ALL

The Assessed Model

$$YNS = c + b_1 \log(YD) + b_2 NPLN$$

Where:

YNS- is the economic growth

YD –new mortgage loans

NPLN-the rate of nonperforming loans

$$YNS = -0.37 + 0.05 \log(YD) - 0.002 NPLN$$

Variable	Coefficient	Std. Error	t-Statistic	Prob.
C	-0.374677	0.154648	-2.422773	0.0245
LOG(YD)	0.051494	0.017470	2.947488	0.0077
NPLN	-0.002080	0.000779	-2.669971	0.0143
R-squared	0.613071	Mean dependent var		0.031250
Adjusted R-squared	0.576221	S.D. dependent var		0.034302
S.E. of regression	0.022330	Akaike info criterion		-4.649298
Sum squared resid	0.010471	Schwarz criterion		-4.502042
Log likelihood	58.79158	Hannan-Quinn criter.		-4.610231
F-statistic	16.63679	Durbin-Watson stat		1.888561
Prob(F-statistic)	0.000047			

Table 3: Results of the assessed model (author calculations)

Based on the above calculations we conclude that the regression coefficients b1 and b2 are statistically important considering that the probabilities are lower than 0.05.

b1 shows that when mortgage loans increase by 1% the economic growth increase by 0.0005% by having constant the NPLN.

b2 shows that when NPLN increase by one unit the economic growth decrease by 0.002 units by having constant the new mortgage loans.

The  $r^2$  value of 0.57 means approximately 57 percent of the variation in the YNS is explained by variation in the YD and NPLN

Hypothesis testing:

To test the significance of the model we will rise the hypothesis based in the Fisher index with the level of significance  $\alpha=0.05$  and  $(k-1), (n-k)$  df , it is often called the critical F value at  $\alpha/2$  level of significance.

If  $F_f > F_{kr}$  then the hypothesis (H0) is rejected, and the assets model is statistically significant

For our model we postulate that :

H0: The assessed model is not statistically significant

Ha: The assessed model is statistically significant

Performing the calculations with E-Views we reach to the conclusion that factice value of Fisher (Ff) is 16.63 while the critic value for  $F(n-k)(k-1) = 4.3$  ( 5% significance) We concluding that the assessed model is statistically significant thus the Ho hypothesis is rejected.

Autocorrelation

To test the presence of the autocorrelation we will use the Durbin Watson test.

$$d = \frac{\sum_{t=2}^n (\hat{u}_t - \hat{u}_{t-1})^2}{\sum_{t=1}^n \hat{u}_t^2}$$

In our model the d value 1.88 is around 2, which would suggest that there is no autocorrelation in such model. Another test performed is the LM test for the serial correlation. Based on the below table we can conclude that there is no presence of the serial correlation in our model

Breusch-Godfrey Serial Correlation LM Test:

F-statistic	1.835905	Prob. F(2,19)	0.1867
Obs*R-squared	3.886917	Prob. Chi-Square(2)	0.1432

Table 4. Results of the LM test (author calculations)

#### Heteroscedasticity Test

An important assumption of the classical linear regression model is that the disturbances term  $u_i$  appearing in the population regression function are homoscedastic; that is, they all have the same variance. Symbolically:

$$E(u_i^2) = \sigma^2 \quad i = 1, 2, \dots, n$$

For our model we postulate that

**Ho: No presence of heteroscedasticity**

**Ha: Presence of heteroscedasticity**

Based of the Arch's heteroscedasticity Test below the estimated model is insignificant and also the coefficients of the model considering the respective probabilities higher than 0.05. We conclude that in our model the heteroscedasticity is not present.

Heteroskedasticity Test: ARCH

F-statistic	2.613473	Prob. F(1,21)	0.1209
Obs*R-squared	2.545576	Prob. Chi-Square(1)	0.1106

Table 5: The results of heteroskedasticity test (author calculations)

**Jarque–Bera (JB) Test of Normality**

The JB test of normality is based on the OLS residuals.

$$JB = n \left[ \frac{S^2}{6} + \frac{(K - 3)^2}{24} \right]$$

where n = sample size, S = skewness coefficient, and K = kurtosis coefficient. For a normally distributed variable, S = 0 and K = 3. Therefore, the JB test of normality is a test of the joint hypothesis that S and K are 0 and 3, respectively. In that case the value of the JB statistic is expected to be 0. If the computed p value of the JB statistic in an application is sufficiently low, which will happen if the value of the statistic is very different from 0, one can reject the hypothesis that the residuals are normally distributed. But if the p value is reasonably high, which will happen if the value of the statistic is close to zero, we do not reject the normality assumption.

Application of the Jarque–Bera test shows that the JB statistic is about 0.273405, and the probability of obtaining such a statistic under the normality assumption is about 87 %. Therefore, we do not reject the hypothesis that the error terms are normally distributed.

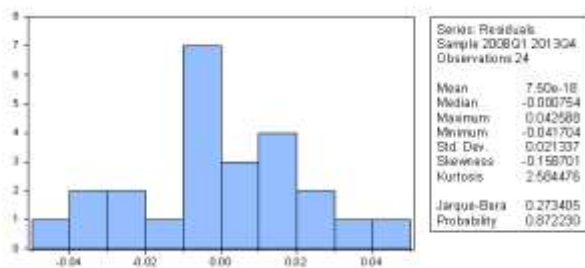


Figure 3: Normality test of residuals series (author calculations)

**4. CONCLUSIONS**

The purpose of this study is to analyze how is housing loans and NPL influencing the economic growth of Albania. The analyze has taken in consideration two factors the new mortgage disbursements and NPL rate as the independent variable and the economic growth as the dependent variable. To treat the problem empirically it was used the lin-log regression model. For the period taken into consideration 2008-2013 corresponding with the financial crises, we reached in the conclusion that the new housing loans has a strong positive relation with the economic growth and the rate of NPL has negative relation with the economic growth. In the last years the demand for housing loans in Albania, decreased in parallel with the decrease of the supply form banks side corresponding to the increase in the non performing loans. On the other hand the prices suffered a low decrease even though the stock of unsold properties increases. The slowdown in loans reflects decrease in the demand side from individuals. Credit Standards and Loan demand in Albania followed almost the same trend as those of Eurozone during this period.

**5. ACKNOWLEDGMENTS**

This paper is part of my PhD thesis which for I would like to thanks all my colleagues and my professors who advised and helped me to progress in my research.

**6. REFERENCES**

- [1] Berger, Allen N. & Humphry De Young, “Problem Loans and Commercial Banks”, Journal of Banking and Finance, Vol. 21, 1997
- [2] Boleat, M. (2008) – Housing Development and Housing Finance in Britain – Some lessons for emerging markets, Housing Finance International March 2008, Vol. 22 Issue 3, pp 53-58
- [3] Diamond, D.B. and M. Lea (1993) – The Efficiency of Housing Finance Systems: An international comparison, Housing Finance International September 1993, Vol.8 Issue 1, pp 36-43.
- [4] Ergungor, O.E. (2008) – Covered Bonds: A new way to fund Residential Mortgages, Federal Reserve Bank of Cleveland Economic Commentary, July 2008.
- [5] Favara, G. (2003) – An Empirical Reassessment of the Relationship between Finance and Growth, IMF Working Paper WP/03/123.
- [6] Fischer, S. (2004) – IMF Essays from a time of Crisis: The International Financial System, *Stabilization and Development*, Cambridge, MA: MIT Press, 2004.
- [7] Veronica C. Warnock Francis E. Warnock (2007) markets and housing finance ( NEBER Paper No.13081)
- [8] Albanian Association of Banks, Credit to the Economy by purpose statistical data 2008-2013 <http://www.aab.al>
- [9] Instat statistics <http://www.instat.gov.al>

# Cu and Ni Mop up from Spent Lubrication Oil Using Disposed Plastic Materials

D. T. Kukwa  
Department of Chemistry,  
Benue State University  
Makurdi, Nigeria

R. E. Ikyereve  
Department of Chemistry,  
Loughborough University,  
Loughborough, UK

E.O. Agbo  
Department of Chemistry,  
Benue State University  
Makurdi, Nigeria

**Abstract:** Spent lubrication oil from a serviceable, functional motor vehicle was cleaned of Cu and Ni using five different types of waste plastic materials (plastic water bottles, vegetable oil gallons and engine oil gallons) in batch adsorption processes. Atomic Absorption spectral (AAS) analysis of the spent oil before cleaning showed that Copper (Cu) was present at 18.2 mgL<sup>-1</sup> and nickel (Ni) at 26.1 mgL<sup>-1</sup> levels. After treatment with the waste plastics, final product plastic (FPP), Goshen water plastic (GWP), water-first plastic (WFP), engine oil waste plastic gallon (EOG) and vegetable oil waste plastic gallon (VOG), the engine oil was observed to contain reduced levels of Cu to as low as 2.3, 3.2, 2.7, 2.4 and 2.9 mgL<sup>-1</sup> respectively while Ni reduced to 10.6, 11.1, 10.7, 10.1 and 10.3 mgL<sup>-1</sup> respectively at equilibrium. The Gibbs free energy of adsorption for the plastic bottles and gallons was determined using standard methods and fell in the range of -0.516 and -4.972kJmol<sup>-1</sup>, which indicates that the process was exclusively physical adsorption. The modified Arrhenius type equation described the metals adsorption pattern onto the plastic materials.

**Keywords:** Spent lubrication oil, adsorbents, heavy metals, thermodynamic parameters, adsorption, Gibbs free energy, activation energy.

## 1. INTRODUCTION

Environmental pollution is currently one of the issues of concern worldwide. Heavy metals found in engine oils is one of the most worrying pollution sources, as it poses a disposal issue to the environment. The effects of these metals on life could be particularly serious in both plants and animals including man through the bioaccumulation in food chain [1]. Nickel and copper along with mercury and arsenic ions are among the cations of high toxicity for both plants and animals including microorganisms [2-4]. These metals, unfortunately, are found in the environment including water bodies which are a source of drinking water at concentrations beyond their permissible levels. For example, around 1.4 mg/day and 0.05 mg/day respectively are found in soft and hard water sources when the guideline for maximum acceptable copper concentration in drinking water is less than 300 µg/dm<sup>3</sup> [5-7]. These metals could be traced to sources like waste-oils and other industrial wastes in the form of leachates from landfills [8-10] among other sources. Removal of these metals from solution is usually achieved using methods such as; precipitations, ion exchange, adsorption, reverse osmosis, electrodialysis, solvent extraction etc. [11-13]. Adsorption is one of the most preferred methods since it is cheaper, economical and presents little or no disposal issues. A number of investigations have been focused on the use of low-cost adsorbents in order to minimize processing costs for wastewater treatment [14-19]. Low-cost adsorbents, like waste ashes and PET, agricultural wastes, waste cobs and husks, activated carbon, chitosan and zeolites have been explored in recent years and shown to be effective at removing metal ions from wastewaters and oils [14, 16, 18-22]. A more recent investigation showed that waste-plastic materials can be used as adsorbents for the removal of Cr and Pb from spent engine oil [23]. The present paper however, seeks to investigate the efficacy of the waste plastics in the removal of Ni and Cu from waste engine oil.

## 2. MATERIALS AND METHODS

### 2.1 Materials

Five waste-plastic samples namely; water-first plastic (WFP\*), final product plastic (FPP\*\*), Goshen-water plastic

(GWP\*\*\*), vegetable oil gallon (VOG\*\*\*\*) and engine oil gallon (EOG\*\*\*\*\*) were collected from waste bins while the spent engine oil was obtained from a marked four-cylinder vehicle after covering a distance of about 1350 kilometers from an automobile workshop in Makurdi town, Nigeria. The labels on the waste-plastic materials were removed and the plastics were cut, thoroughly washed with water and air-dried. They were shredded into smaller sizes, pounded into chips, sieved with a 2mm sieve to obtain a powder with good and uniform particle distribution and stored in polyethene bags for subsequent analyses and application.

### 2.2 Physicochemical characterization of the adsorbents

The adsorbents pH, bulk density and porosity were determined as described by Itodo and coworkers [17]. The adsorbent pH was determined by adding 1.0 g of the sample into 100 mL of distilled water and stirred for 1 h at regular interval. The mixture was then filtered and the pH of the filtrate was determined using pH meter. The bulk density expressed in g/mL was determined using the tapping method. The adsorbent porosity was determined using the saturation method by adding 3.0 g of sample into 100 mL distilled water and allowed to stand for 48 h. The mixture was then filtered and the filtrate volume measured. The iodine adsorption ratio (IAR) was determined as described by Malik and coworkers [24]. Portions of the adsorbent (1.0 g) were slurred in excess (25 mL, 0.05 M) iodine solution in a beaker. The mixture was then stirred vigorously for 10 min and filtered through a funnel impregnated with glass wool. 20 mL of the filtrate was back-titrated with 0.1 M sodium thiosulphate solution. The iodine ratio was calculated as moles of iodine adsorbed per gram of adsorbent. The adsorbent attrition factor (AF) was determined using the procedure described earlier [25], which is based on the measurement of the percentage of the adsorbent retained in a 2 mm sieve after 1.0 g was stirred with magnetic stirrer in 100 mL acetate buffer of pH 4.0 for 4 h, which was calculated based on the weight loss of the adsorbent after the stirring and reported as percentage attrition. Cation exchange capacity (CEC) was obtained

according to the method described by Kandah [26]. The Adsorbent (2.0 g) was left for 4 h in an excess of 33 mL of 1.0 M sodium acetate solution after which it was filtered and washed with 33mL isopropyl alcohol. The procedure was repeated thrice but without washing with the alcohol at the last round. Thereafter, the filtered adsorbent was washed with 33 mL of 1.0 M ammonium acetate solution and the concentration of the displaced Na in the filtrate determined using a Jenway flame photometer model PFP 7.

\*; \*\*, \*\*\* = water first (WF), final product (FP), Goshen water (GW): Company name of water supplies

\*\*\*\*; \*\*\*\*\* = vegetable oil gallon (VOG) and engine oil gallon (EOG): Type of oil plastic

## 2.3 Adsorption Studies

The method by Jabar and coworkers [27] was adopted in which the initial concentrations of Cu and Ni in the spent lubrication oil were determined by measuring 100 mL of untreated spent lubrication oil into five different beakers; the first beaker was kept at room temperature of 305 K while the rest (one at a time) had their temperatures raised to 315, 325, 335, and 345 K respectively in a warm water bath. A one in ten dilution of the oil with kerosene was done in a labeled specimen bottle in preparation for AAS analysis. The same procedure was carried out for 100 mL of the spent lubrication oil after treatment with 5.0 g of the adsorbent and stirred for 30 min (while the temperature was being raised) and filtered. The equilibrium concentrations of the metals were then determined using a Buck Scientific Atomic Absorption Spectrophotometer model VGP 210.

## 2.4 Adsorption Thermodynamics

The thermodynamic properties of the adsorbents were determined using the Van't Hoff's equation (Venkatraman and coworkers) [22] as expressed in equation (1).

$$\ln K_{ad} = -\frac{\Delta H^\circ}{RT} + \frac{\Delta S^\circ}{R} \quad (1)$$

$$K_{ad} = \frac{C_{ad}}{C_e} \quad (2)$$

$$\Delta G^\circ = -RT \ln K_{ad} \quad (3)$$

Where;

$\Delta H^\circ$  is enthalpy ( $\text{kJmol}^{-1}$ ),  $\Delta S^\circ$  is entropy ( $\text{Jmol}^{-1}\text{K}^{-1}$ ),  $\Delta G^\circ$  is Gibb's free energy ( $\text{kJmol}^{-1}$ ), R is the gas constant ( $8.314 \text{ Jmol}^{-1}\text{K}^{-1}$ ), T is temperature in Kelvin,  $K_{ad}$  is the adsorption equilibrium constant,  $C_{ad}$  is the amount of metal adsorbed onto the adsorbent per litre of the analyte solution at equilibrium in  $\text{mgL}^{-1}$  and  $C_e$  is the equilibrium concentration ( $\text{mgL}^{-1}$ ) of metal left unadsorbed in the analyte solution.

## 3. RESULTS AND DISCUSSION

### 3.1 Physicochemical characterization of the adsorbents

Results for Physicochemical Characterization of the adsorbents (FPP, WFP, GWP, EOG and VOG) are shown in Table 1.

The pH of adsorbents influences the species and extent of adsorption. VOG has the highest pH value of 7.78 followed by EOG with pH of 7.53, GWP with pH 7.28, WFP with pH 6.80 and FPP with pH 6.71. Three of the adsorbents, VOG,

EOG and GWP each had a slightly alkaline pH value while the rest two, WFP and FPP had slightly acidic pH values.

The bulk density (BD) of adsorbents indicates the mass of the adsorbent that can be contained in a filter of a given capacity during the design of an adsorption column and the quantity of the treated liquid retained. The bulk density of the adsorbents increases in the order  $\text{EOG} < \text{VOG} < \text{WFP} < \text{FPP} < \text{GWP}$  with values 0.1702 g/mL, 0.1951 g/mL, 0.3200 g/mL, 0.3478 g/mL and 0.4211 g/mL respectively as shown in Table 1. Porosity indicates the efficiency of an adsorbent during adsorption process. The porosity of the adsorbents decreases in the order  $\text{EOG} > \text{VOG} > \text{FPP} > \text{WFP} > \text{GWP}$  with values 12 mL, 10 mL, 9.5 mL, 9 mL and 8 mL respectively.

Iodine adsorption ratio (IAR) also measures the adsorptive performance of an adsorbent. These plastic adsorbents show increase in IAR in the order  $\text{WFP} < \text{GWP} < \text{FPP} < \text{VOG} < \text{EOG}$  with values 0.0205, 0.0455, 0.0550, 0.0890 and 0.0915 mol/g respectively. Attrition factor (AF) is the measure of the resistance of an adsorbent to mechanical abrasion and indicates the mechanical strength of that adsorbent during transportation, handling and regeneration. The AF of the adsorbents increases in the order  $\text{EOG} < \text{VOG} < \text{FPP} < \text{WFP} < \text{GWP}$  with values 1, 3, 8, 11 and 17% respectively. Cation exchange capacity (CEC) measures the quantity of adsorptive sites the adsorbent possesses. The CEC of the adsorbents under investigation increases in the order  $\text{GWP} < \text{WFP} < \text{FPP} < \text{VOG} < \text{EOG}$  with values 2.50, 3.50, 3.75, 6.25 and 7.50 mg/L respectively.

### 3.2 Adsorption Studies

The adsorption of the metals by the adsorbents at equilibrium is shown in Table 2. From the generated data,

VOG with a slightly alkaline pH of 7.78 has Ni metal preferentially adsorbed at all the experimental temperatures than Cu although the amount adsorbed decreases as the temperature increases from 305 K to 345 K. The trend of adsorption was thus;  $\text{Ni} (15.8 \text{ mgL}^{-1}) > \text{Cu} (15.3 \text{ mgL}^{-1})$ . At the pH of 7.53, the adsorption for EOG was such that  $\text{Ni} (16.0 \text{ mgL}^{-1}) > \text{Cu} (15.3 \text{ mgL}^{-1})$ . For GWP with the pH of 7.28, both Cu and Ni were adsorbed equally ( $15.0 \text{ mgL}^{-1}$ ) but as the temperature increased, more Cu was adsorbed than Ni. At the pH of 6.80 and 305 K temperature, WFP favours the adsorption of Cu ( $15.5 \text{ mgL}^{-1}$ )  $>$  Ni ( $15.4 \text{ mgL}^{-1}$ ). FPP with the pH of 6.71 and at 305 K adsorbed Cu ( $15.9 \text{ mgL}^{-1}$ )  $>$  Ni ( $15.5 \text{ mgL}^{-1}$ ). It was observed that the adsorption was most favoured at neutral pH.

The bulk density of the adsorbents increases in the order  $\text{EOG} < \text{VOG} < \text{WFP} < \text{FPP} < \text{GWP}$  while the amount of metal species adsorbed decreased in somewhat the same order. The general observation could be explained based on the difference in bulk densities of the various adsorbents, the higher the bulk density of the adsorbent, the lower the pore size volume, hence the adsorption of metal ions will be reduced. The adsorption capacity of the adsorbents decreases as their porosity values decreases in the order  $\text{EOG} < \text{VOG} < \text{FPP} < \text{WFP} < \text{GWP}$ . The porosity as well as the CEC also explains the observed behavior of the adsorbents. The porosity of adsorbents plays an important role in the adsorption of metal ions. Adsorbents with high porosity have high adsorption capacity. The porosity and CEC of the adsorbents were observed to decrease in the order  $\text{EOG} > \text{VOG} > \text{WFP} > \text{FPP} > \text{GWP}$ .

The adsorptive performance of the adsorbents decreases as their IAR decreases in the order  $\text{EOG} > \text{VOG} > \text{FPP} > \text{GWP}$

> WFP except that GWP with a little higher IAR value of 0.0455 mol/g adsorbed lesser amount of metals than WFP with lower IAR value of 0.0205 mol/g.

The adsorbents increase in attrition factor (AF) values in the order EOG < VOG < FPP < WFP < GWP but decrease in adsorption performance in the same order implying that an increase in the AF leads to low adsorption capacity or vice versa. The adsorption capacity of the adsorbents decreases in the order EOG > VOG > FPP > WFP > GWP as the effect of CEC follows the same order.

### 3.3 Adsorption Thermodynamics

Using equation (1), the plots of  $\ln K_{ad}$  against  $1/T$  for each of the metals, gave straight lines with a slope equal to  $(\Delta H^{\circ})/R$  and intercepts equal to  $(\Delta S^{\circ})/R$ .  $K_{ad}$  and  $\Delta G^{\circ}$  were calculated from equations 2 and 3. The values of  $K_{ad}$  are presented in Table 2 while those of  $\Delta H^{\circ}$ ,  $\Delta S^{\circ}$  and  $\Delta G^{\circ}$  are presented in Table 3. The plots of  $\ln K_{ad}$  vs  $T$  in figures 1 and 2 show the dependence of equilibrium constants on temperature. The negative slopes of these plots show that metals uptake by these plastic adsorbents is exothermic in nature [28]. The Van't Hoff plots for Cu adsorption are as presented in figure 3 while those for Ni adsorption are presented in figure 4. The values of  $\Delta H^{\circ}$  for the adsorption of the metals onto all the adsorbents were negative and in the range of -2.203 to -5.316  $\text{kJmol}^{-1}$ . These negative values confirm the exothermic nature of the adsorption process. The positive value of  $\Delta S^{\circ}$  (0.988  $\text{Jmol}^{-1}\text{K}^{-1}$ ) for the adsorption of Cu by FPP indicates that

though there are electrostatic attractions, the metal is still mobile and is loosely adsorbed onto the adsorbent surface during the process. The value of  $\Delta S^{\circ}$  for the metals adsorbed onto all other adsorbents is negative indicative of decrease disorder and randomness at the adsorbent-analyte interface. The values of  $\Delta G^{\circ}$  for the metals were negative at all the temperatures considered. The negative values of  $\Delta G^{\circ}$  show the spontaneous nature of adsorption of the metals onto the adsorbents.  $\Delta G^{\circ}$  values which are less than or more negative than -20.0  $\text{kJmol}^{-1}$  are consistent with electrostatic interactions between the adsorption sites and the metal showing physical adsorption while  $\Delta G^{\circ}$  values more negative than -40.0  $\text{kJmol}^{-1}$  involve charge sharing or transfer from the adsorbent surface to the metal ion to form a coordinate bond, indicating chemical adsorption [29]. The  $\Delta G^{\circ}$  values obtained in this study for the metals are less than -4.972  $\text{kJmol}^{-1}$ , indicating that adsorption occurred by physical process.

To further strengthen the asserted adsorption mechanism, activation energy,  $E_a$ , and sticking probability,  $S^*$ , were estimated from the experimental data. They were calculated using a modified Arrhenius equation (equation 4) related to surface coverage of adsorbed species ( $\theta$ ) [30].

$$S^* = (1-\theta) \exp(-E_a/RT) \quad (4)$$

$$\theta = (1 - C_e/C_0) \quad (5)$$

Equation (4) is rearranged as in equation (6).

$$\ln(1-\theta) = \ln S^* + (E_a/RT) \quad (6)$$

## 4. TABLES AND FIGURES/CAPTIONS

Table 1: Physicochemical Properties of the Plastic Adsorbents

Property	FPP	WFP	GWP	EOG	VOG
pH	6.71	6.80	7.28	7.53	7.78
Bulk density (g/mL)	0.3478	0.3200	0.4211	0.1702	0.1951
Porosity (mL)	9.5	9.0	8.0	12.0	10.0
IAR (mol/g)	0.0550	0.0205	0.0455	0.0915	0.0890
AF (%)	8.0	11.0	17.0	1.0	3.0
CEC (mg/L)	3.75	3.50	2.50	7.50	6.25

Table 2: Adsorption of Cu and Ni onto Plastic Adsorbents

Adsorbent	T (K)	Cu			Ni		
		C <sub>o</sub> (mg/L)	C <sub>e</sub> (mg/L)	K <sub>ad</sub> (Cu)	C <sub>o</sub> (mg/L)	C <sub>e</sub> (mg/L)	K <sub>ad</sub> (Ni)
VOG	305	18.2	2.9	5.2759	26.1	10.3	1.5340
	315	18.3	3.1	4.9032	26.2	10.5	1.4952
	325	18.3	3.2	4.7188	26.3	10.7	1.4579
	335	18.4	3.4	4.4118	26.4	10.9	1.4220
	345	18.4	3.5	4.2571	26.6	11.2	1.3750
WFP	305	18.2	2.7	5.7407	26.1	10.7	1.4393
	315	18.3	2.9	5.3103	26.2	10.9	1.4037
	325	18.3	3.0	5.1000	26.3	11.1	1.3694
	335	18.4	3.2	4.7500	26.4	11.3	1.3363
	345	18.4	3.3	4.5758	26.6	11.6	1.2931
FPP	305	18.2	2.3	6.9130	26.1	10.6	1.4623
	315	18.3	2.4	6.6250	26.2	10.8	1.4259
	325	18.3	2.5	6.3200	26.3	11.0	1.3909
	335	18.4	2.7	5.8148	26.4	11.2	1.3571
	345	18.4	2.8	5.5714	26.6	11.5	1.3130
GWP	305	18.2	3.2	4.6875	26.1	11.1	1.3514
	315	18.3	3.4	4.3824	26.2	11.4	1.2982
	325	18.3	3.5	4.2286	26.3	11.6	1.2672
	335	18.4	3.7	3.9730	26.4	11.9	1.2185
	345	18.4	3.8	3.8421	26.6	12.1	1.1983
EOG	305	18.2	2.4	6.5833	26.1	10.1	1.5842
	315	18.3	2.6	6.0385	26.2	10.3	1.5437
	325	18.3	2.7	5.7778	26.3	10.5	1.5048
	335	18.4	2.9	5.3448	26.4	10.7	1.4673
	345	18.4	3.0	5.1333	26.6	11.0	1.4182

Table 3 Thermodynamic Parameters for the Adsorption of Cu and Ni onto Various Plastic Adsorbents

Metal	Adsorbent	$-\Delta H^\circ$ (kJ/mol)	$\Delta S^\circ$ (J/mol/K)	$-\Delta G^\circ$ (kJ/mol)				
				305 K	315 K	325 K	335 K	345 K
Cu	VOG	4.510	-0.935	4.209	4.164	4.188	4.122	4.159
	WFP	4.504	-0.416	4.438	4.374	4.404	4.345	4.360
	FPP	4.610	0.988	4.894	4.950	4.972	4.902	4.934
	GWP	4.483	-2.079	3.905	3.876	3.891	3.844	3.872
	EOG	4.612	0.312	4.767	4.714	4.729	4.679	4.704
Ni	VOG	2.156	-3.492	1.090	1.048	1.027	0.975	0.918
	WFP	2.140	-4.053	0.913	0.890	0.838	0.808	0.746
	FPP	2.113	-3.741	0.964	0.917	0.892	0.863	0.774
	GWP	2.184	-4.781	0.761	0.681	0.648	0.557	0.516
	EOG	2.079	-3.076	1.166	1.126	1.108	1.058	1.004

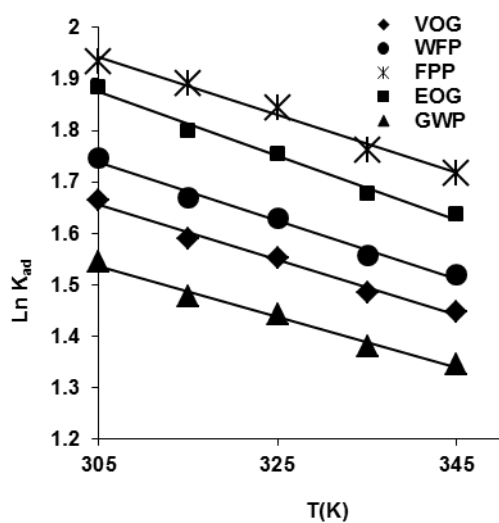


Figure 1 Variation of  $\ln K_{ad}$  with  $T$  for Cu adsorption

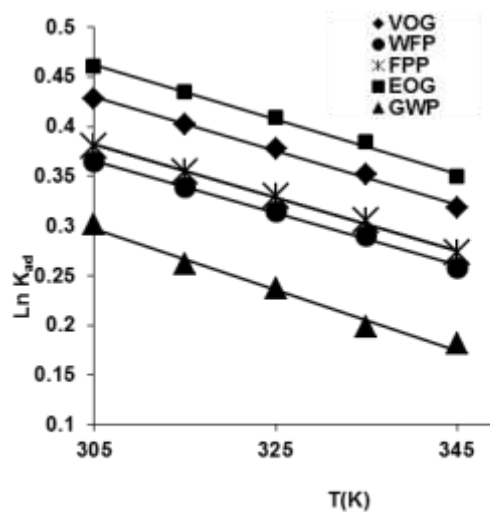


Figure 2 Variation of  $\ln K_{ad}$  with  $T$  for Ni adsorption

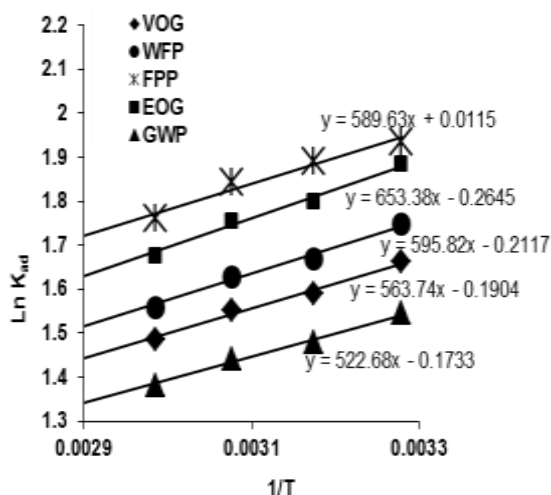


Figure 3 Plots of  $\ln K_{ad}$  vs  $1/T$  for Cu adsorption

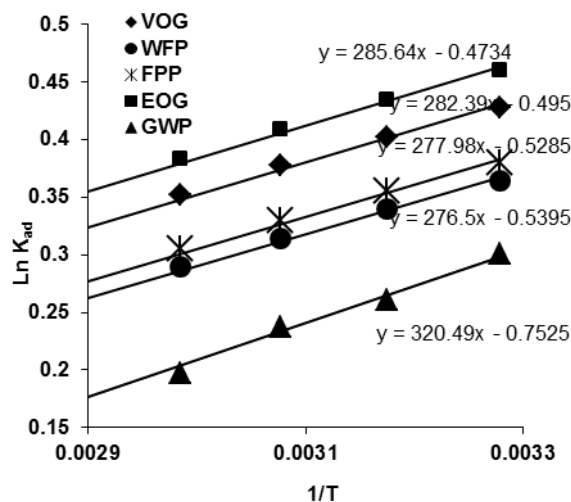


Figure 4 Plots of  $\ln K_{ad}$  vs  $1/T$  for Ni adsorption

## 5. CONCLUSIONS

Waste plastic materials can be used effectively as adsorbents for mopping up heavy metal pollutants like Cu and Ni from used lubrication oils and other related sources. Plastic gallons used for engine oil storage and transportation (EOG) proved very effective for removing such metals from such sources. This is followed closely by other plastic materials investigated in this work in the order of VOG > FPP > WFP > GWP. Physical adsorption mechanism prevailed in the mopping process, signifying dominance of electrostatic attractions. For all the materials, the adsorption capacity decreased as the temperature was raised and it increases when the pore size in increased. The neutral pH of the adsorbents used in the study was shown to favor the heavy metal adsorption. The negative low values of  $\Delta G^\circ$  indicate that the process was driven by electrostatic attractions onto the surface of adsorbent material physical adsorption.

## 6. ACKNOWLEDGMENTS

The authors of this work would like to acknowledge the Benue State University Makurdi, Nigeria particularly the Chemistry department for their support during the course of this work.

## 7. REFERENCES

- [1] Para, J. B., Ania, C. O., Arenillas, A., Rubiera, F., Palacios J. M., and Pis, J. J. (2004). Textural Development and Hydrogen Adsorption of Carbon Materials from PET waste. *Journal of Alloys and Compounds*, 379 (1-2), 280 – 289.
- [2] Kabata-Pendias, A., Pendias, H. (1984). *Trace Elements in Soils and Plants*, CRC Press, Boca Raton.
- [3] Train, R.E. (1979) *Quality Criteria for Water*, Castle House, London.
- [4] Bowen, H. J. M. (1979). *The Environmental Chemistry of the Elements*, Academic Press, London.
- [5] Davies, D. J. A., and Bennett, B. G. (1983). *Exposure Commitment Assessments of Environmental Pollutants*, vol. 3, Monitoring and Assessment Research Centre, London.

- [6] Manahan, S.E. (1991). *Environmental Chemistry*, Lewis, Chelsea, MI, 5th edition.
- [7] Murley, L. (1992). *Pollution Handbook*, National Society for Clean Air and Environmental Protection, Brighton.
- [8] Alloway, B. J., Ayres, D.C. (1981). *Chemical Principles of Environmental Pollution*, Chapman and Hall, Oxford.
- [9] Peters, W.C. (1978). *Exploration and Mining Geology*, Wiley, New York.
- [10] O'Neill, P. in: Alloway, B. J. (Ed.), (1990). *Heavy Metals in Soils*, Blackie and Son, Glasgow.
- [11] Griffin R.D. (1988). *Principles of Hazardous Materials and Management*, Lewis, Ann Arbor.
- [12] Davis, M. L and Cornwell, D. A. (1991). *Introduction to Environmental Engineering*, McGraw-Hill, New York, 2<sup>nd</sup> edition.
- [13] Fergusson, J. E. (1990). *The heavy elements: Chemistry, Environmental impact and Health Effects*, Pergamon, Oxford.
- [14] Zhan, F. and Itoh, H. (2003). Adsorbents made from Waste Ashes and Post-customer PET and their Potential Utilization in Waste Water Treatment. *Journal of Hazardous Materials*, 101 (3), 323 – 337.
- [15] Kumar, P. S. and Kirthika, K. (2009). Equilibrium and kinetic study of adsorption of nickel from aqueous solution onto bael tree leaf powder. *Journal of Engineering Science and Technology*, 4 (4), 351 – 361.
- [16] Bansal, M., Singh, D., Garg, V. K. and Pawan, R. (2009). Use of Agricultural Waste for the Removal of Ni Ions from Aqueous Solutions: Equilibrium and Kinetic Studies, *International Journal of Environmental Science and Engineering*, 1 (2), 108 – 114.
- [17] Itodo, A.U., Abdulrahman, F.W., Hassan, L.G., Maigandi, S.A., and Itodo, H.U. (2010). Physicochemical parameters of adsorbents from locally sorted  $H_3PO_4$  &  $ZnCl_2$  modified agricultural wastes, *New York science journal*, 3 (5), 17-24.
- [18] Demirbas, E., Kobya, M., Senturk E., and Ozkan, T. (2004). Adsorption kinetics for the removal of chromium (VI) from aqueous solutions on the activated carbons prepared from agricultural wastes, *Water SA* 30(4), 533-539.

- [19] Babel, S., Kurniawen, T. A., Hazrel J., and Mater, B. (2003). Maize Cob and Husk as Adsorbents for the removal of Cd, Pb, and Zn ions from Waste Water, *Journal of Soil Science*, 42, 403- 409.
- [20] Venkatraman, B.R., Parthasarathy, S., Kasthuri, A., Pandia P., and Arivoli, S. (2009). Adsorption of Cr ions by Acid Activated Low-cost Carbon-kinetic, thermodynamic and Equilibrium Studies, *E- Journal of Chemistry*. 6(S1), S1 –S11.
- [21] Radnia, H., Ghoreyshi, A. A., and Younesi, H. (2011). Isotherm and kinetics of Fe (II) adsorption onto chitosan in a batch process, *Iranica Journal of Energy & Environment*, 2 (3), 250 – 257.
- [22] Ali, S.M.W., Ripin A., and Ahmed, A. (2010). Adsorption of Heavy Metals from Recovered Base Oil using Zeolite, *Journal of Applied Sciences*, 10 (21), 2688-2692.
- [23] Kukwa, D.T., Ikyereve R.E., and Agbo, E.O. (2014). Removal of Cr and Pb from spent Engine Oil using Waste Plastic materials as Adsorbent, *International Journal of Scientific and Engineering Research*, 5 (5), 1162-1169.
- [24] Malik, R., Ramteke, D.S., Wate, S.R. (2006). Physicochemical and surface characterization of adsorbent prepared from groundnut shell by ZnCl<sub>2</sub> activation and its ability to adsorb colour, *Indian journal of chemical Technology*, 13, 319-328.
- [25] Toles, C.A., Marshall, W. E., Johns, M. M., Wartelle I. A. and McAloon, A. (2000). Acid Activated Carbons from Almond Shells; Physical, Chemical and Adsorptive Properties and Estimated Cost of Production, *Bioresource Technology*, 71, 87- 92.
- [26] Kandah, M.I., Allawzi M.A. and Allabonn, H. (2008). Improvement of Manure Adsorption Capacity for Co Removal by Chemical Treatment with Citric Acids, *Jordan Journal of Civil Engineering*, 2 (4), 344 – 354.
- [27] Jabar, J.M., Mojibola A.A. and Adetuyi, A.O. (2011). Adsorption Thermodynamic Studies of Indigo Adsorption on Some Activated Bio-solids from Dyeing Effluent, *Conference Proceedings of the 34th Annual International Conference of Chemical Society of Nigeria*.
- [28] Smith, J.M., Van Ness, H.C., and Abbott, M.M. (2005). *Introduction to Chemical Engineering Thermodynamics*, 7<sup>th</sup> ed. McGraw Hill, New York 492-497
- [29] Micheal, H. and Agebaemi, I.S. (2005). Effects of Temperature on the Sorption of Pb<sup>2+</sup> and Cd<sup>2+</sup> from Aqueous Solution by Caladium bicolor (wild cocoyam) biomass, *Electronic Journal of Biotechnology*, 8 (2), 163-169.
- [30] Chaudhari, A. and Lee, S.L. (2008). Effect of sticking probability on monomer-dimer reaction, *Bulletin of the Catalysis Society of India*, 7, 90-95.

# Sliding Window for Radial Basis Function Neural Network Face Detection

K.A.A Aziz  
 Faculty of Engineering  
 Technology  
 Universiti Teknikal Malaysia  
 Melaka  
 Melaka, Malaysia

N. Mohamood  
 Faculty of Engineering  
 Technology  
 Universiti Teknikal Malaysia  
 Melaka  
 Melaka, Malaysia

M.N.Z. Hashim  
 Faculty of Electronics and  
 Computer Engineering  
 Universiti Teknikal Malaysia  
 Melaka  
 Melaka, Malaysia

**Abstract:** This paper present a Radial Basis Function Neural Network (RBFNN) face detection using sliding windows. The system will detect faces in a large image where sliding window will run inside the image and identified whether there is a face inside the current window. Face detection is the first step in face recognition system. The purpose is to localize and extract the face region from the background that will be fed into the face recognition system for identification. General preprocessing approach was used for normalizing the image and a Radial Basis Function (RBF) Neural Network was used to distinguish between face and non-face images. RBFNN offer several advantages compared to other neural network architecture such as they can be trained using fast two stages training algorithm and the network possesses the property of best approximation. The output of the network can be optimized by setting suitable values of the center and spread of the RBF. In this paper, a uniform fixed spread value will be used. The performance of the system will be based on the rate of detection and also false negative rate.

**Keywords:** Face detection, Radial Basis Function Neural Network, Sliding Window.

## 1. INTRODUCTION

Biometrics deals with the identification of individuals based on their biological or behavioral characteristics [1]. By using that trait to obtain a biometric enrollment, we can say that with a degree of certainty that someone is the same person in future biometric authentications based on their previous enrollment authentications [2]. A number of biometrics have been proposed, researched and evaluated for identification applications. Face is one of the most acceptable biometrics because it is one of the most common methods of identification which humans use in their interactions [1]. Face detection is the first step in face recognition system. Face detection can be regarded as a more general case of face localization. In face localization, the task is to find the locations and sizes of a known number of faces. One of the methods for face detection is Neural Networks which lies under the category of image based approach. In this paper, we focus on optimizing the RBF Neural Network for face detection. RBFNN is used to distinguish face and non-face images. The output of the network can be optimized by setting suitable values of the center and the spread of the RBF. The system will detect many faces in a large image where sliding window will run inside the image and identified whether there is a face inside the current window.

## 2. RADIAL BASIS FUNCTION NEURAL NETWORK

RBFNN offers several advantages compared to the Multilayer Perceptrons. Two of these advantages are:

1. They can be trained using fast 2 stages training algorithm without the need for time consuming non-linear optimization techniques.
2. ANN RBF possesses the property of 'best approximation' [9]. This means that if in the set A of approximating functions (for instance the set  $F(x, w)$  spanned by parameters  $w$ ), then the RBFNN has the

minimum distance from any given function of a larger set, H.

RBFNN had been successfully used in face detection such as in Mikami, et. al., 2003[3]. Figure 1 illustrates the architecture of the RBFNN used in this work.

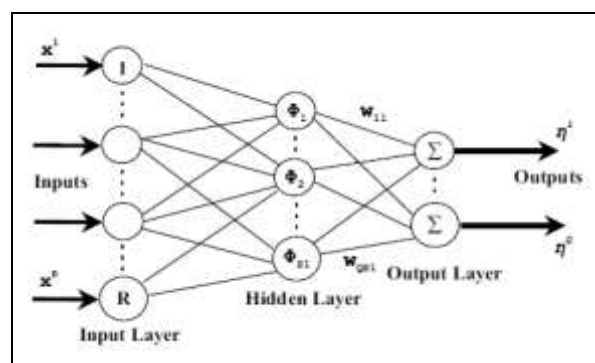


Figure 1: RBF Neural Network

The network consists of three layers: an input layer, a hidden layer and an output layer. Here, R denotes the number of inputs while Q the number of outputs. For  $Q = 1$ , the output of the RBFNN in Figure 1 is calculated according to

$$\eta(x, w) = \sum_{k=1}^{S1} w_{1k} \phi(\|x - c_k\|_2) \quad (1)$$

where  $x \in \mathcal{R}^{R \times 1}$  is an input vector,  $\phi(\cdot)$  is a basis function,  $\|\cdot\|$  denotes the Euclidean norm,  $w_{1k}$  are the weights in the output layer, S1 is the number of neurons ( and centers) in the

hidden layer and  $c_k \in \mathfrak{R}^{R \times 1}$  are the RBF centers in the input vector space. Equation (1) can also be written as

$$\eta(x, w) = \phi^T(x)w \quad (2)$$

where

$$\phi^T(x) = [\phi(\|x - c_1\|) \dots \phi_{S1}(\|x - c_{S1}\|)] \quad (3)$$

and

$$w^T = [w_{11}w_{12} \dots w_{1S1}] \quad (4)$$

The output of the neuron in a hidden layer is a nonlinear function of the distance given by:

$$\phi(x) = e^{-\frac{x^2}{\beta^2}} \quad (5)$$

where  $\beta$  is the spread parameter of the RBF. For training, the least squares formula was used to find the second layer weights while the centers are set using the available data samples.

### 3. NETWORK TRAINING

The image that to be fed into the network whether for training or testing will be normalized using a preprocessing step, adapted from [4].

In this project, image is first converted into double class in matrix form. The matrix is the converted into column matrix  $1 \times n$ . This input will be fed into the RBF network for the next process.

The network is trained using 2429 face data and 4548 non-face data from the CBCL (Center For Biological and Computation Learning) train datasets [5].

K-means clustering is one of the techniques that was used to find a set of centers where the technique is more accurately reflects the distribution of the data points [6]. It is used in research such as in [3] and [7]. In k-means clustering, the number of desired centers, K, must be decided in advance.

The simplest procedure for selecting the basis function centers  $c_k$  is to set the center equal to the input vectors or a random subset of the input vectors from the training set but this is not an optimal procedure since it leads to the use of unnecessarily large number of basis function [6]. Broomhead et al. [8] suggested strategies for selecting RBF centers randomly from the training data. The centers of RBF can either be distributed uniformly within the region of input space for which there is data.

For the training, supervised learning is used where training patterns are provided to the RBFNN together with a teaching signal or target. As for the input of face will be given the value of 1 while the input of non-face will be given the value of -1.

### 4. SLIDING WINDOWS

Sliding window can be described as a matrix of pixels ( $i \times j$ ) that moves through the entire pixels of an image. In this project, both the value of x and y are 19. The matrix is smaller compared to the matrix of the image. Therefore, the matrix

can be compared to many parts in the matrix of the image. The sliding window has a same size with the distribution-based model matrix. It is matched to the distribution-based model for looking the difference feature vectors. In this project, a window by the size of  $19 \times 19$  will be used. The program will first calculate the size of the large image. Then the window will moves through the entire pixels of an image.

For the image with the size of ( $x \times y$ ) the sliding window can be given by:

```
for i=1:1:x-19
    for j=1:1:y-19
        CurrentImage=Image(j:18+j,i:18+i,1);
    end
end
```

Most of the image-based approaches apply a window scanning technique for detecting faces. The window scanning algorithm is in essence just an exhaustive search of the input image for possible face locations at all scales, but there are variations in the implementation of this algorithm for almost all the image-based systems. Typically, the size of the scanning window, the sub sampling rate, the step size, and the number of iterations vary depending on the method proposed and the need for a computationally efficient system. [9]

### 5. TESTING

The system will detect many faces in a large image. The image for testing is taken from [10]. Sliding window will run inside the image and identified whether there is a face inside the current window. If a face is detected, the system will put a rectangular mark on the face. In [10] they are using new reduced set method for Support Vector Machines (SVMs).

### 6. RESULTS

For detecting many faces in an image, setting the system with center 2 as shown in Figure 2 gives the worst result as there are too many false accept. It is hard to see whether the system detect all faces as there are too many overlapped rectangular. Increasing the value of center improved the result as the false negative becomes less as in Figure 3. For the use of center 5 and spread 10, the system cannot detect two faces and yet have two false accept.

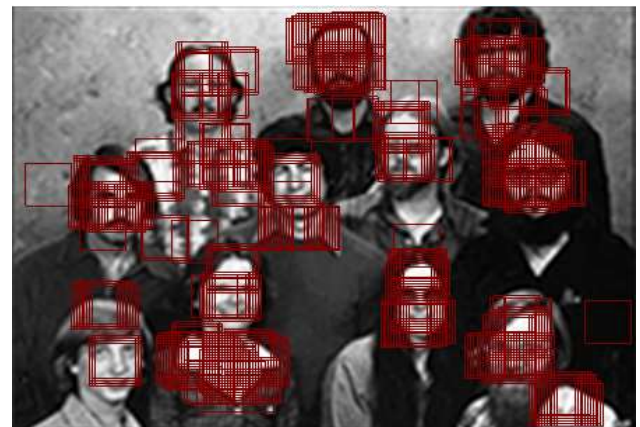


Figure 2: Using RBF with the value of Centre 2 and Spread 4

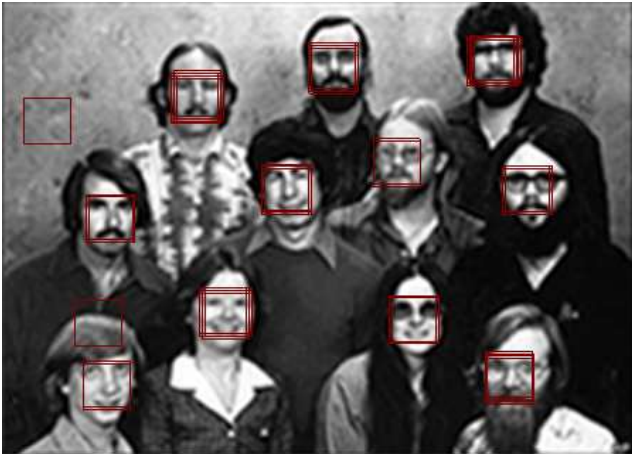


Figure 3: Using RBF with the value of Centre 5 and Spread 4

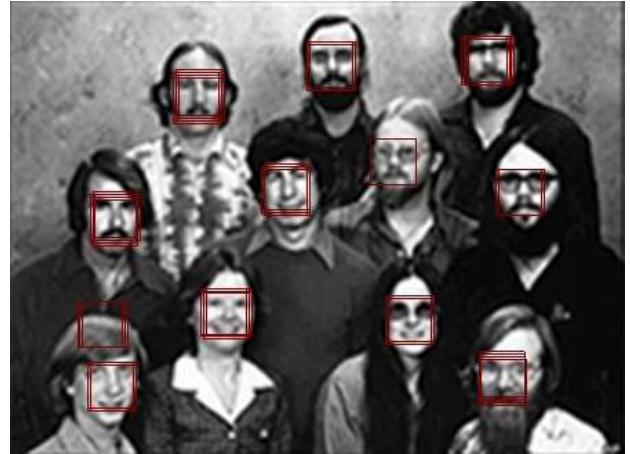


Figure 6: Using RBF with the value of Centre 25 and Spread 4



Figure 4: Using RBF with the value of Centre 5 and Spread 10

Starting with center 25 and above, the results are much better as the system can detect all faces in the picture without any false accept as we refer to Figure 5. But still the spread value is crucial where we can still get false accept as shown in Figure 6 and Figure 7 for center 25 and 200.



Figure 7: Using RBF with the value of Centre 200 and Spread 5

For Center 200, spread value of 5 will ensure that the system detect all faces in the image without false accept as shown in Figure 7. As for spread 4, the system can detect all faces but with 2 false accept.



Figure 5: Using RBF with the value of Centre 25 and Spread 5

## 7. CONCLUSION

In section 5, setting the center higher than 25 will ensure that all faces in the image will be detected. But still the value of spread is crucial. This can be seen in Figure 6 where there is one false accept. For 25 centers, spread equal to 4 is the best setting. But for center 200, using spread equal to 5 will ensure that the system detects all faces in the image.

## 8. ACKNOWLEDGMENTS

The authors would like to express their gratitude to the Universiti Teknikal Malaysia Melaka for providing the facilities and financial assistance to conduct this research.

## 9. REFERENCES

- [1] A. Jain, R. Bolle, and S. Pankanti, "Biometrics: Personal Identification in Networked Society", Springer Science+Business Media, Inc 2006.
- [2] P. Reid, "Biometrics for Network Security", Pearson Education, Inc 2004.
- [3] T. Mikami, M. Wada, "Example-based Face Detection Using Independent Component Analysis and RBF Network", SICE Annual Conference in Fukui, August 4-6, 2003.
- [4] H. A. Rowley, S. Baluja, and T. Kanade. "Neural Network-Based Face Detection", IEEE Trans. Pattern Analysis and Machine Intelligence, vol. 20, no. 1, pp. 23-38. 1998.
- [5] CBCL Face Database #1 MIT Center For Biological and Computation Learning  
<http://www.ai.mit.edu/projects/cbcl>
- [6] S. S. Abdullah, M. M. Idris, "A Short Course In Artificial Neural Networks" 2008.
- [7] M. J. Er, S. Wu, J. Lu, and H. L. Toh, Face Recognition With Radial Basis Function (RBF) Neural Networks, IEEE Transaction On Neural Networks, Vol. 13, No. 3, May 2002.
- [8] D. S. Broomhead and D. Lowe, Multivariable functional interpolation and adaptive networks, Complex Systems, vol. 2, pp 321-355.
- [9] E. Hjelmas, and B. K. Low, "Face Detection: A Survey" Academic Press, 2001.
- [10] W. Kienzle, G. Bakir, M. Franz and B. Scholkopf: Face Detection - Efficient and Rank Deficient. In: Advances in Neural Information Processing Systems 17, pg. 673-680, 2005.
- [11] K.A.A. Aziz, S.S. Abdullah, R.A. Ramlee and A.N. Jahari. "Face Detection Using Radial Basis Function Neural Networks With Variance Spread Value", The International Conference of Soft Computing and Pattern Recognition (SoCPaR 2009) Malacca, Malaysia, December 4-7, 2009.
- [12] K.A.A. Aziz, R.A. Hamzah, S.D.I Damni, A.N.M. Johari and S.S. Abdullah. "Face Recognition Using Fixed Spread Radial Basis Function Neural Network For Security System," Journal of Telecommunication, Electronic And Computer Engineering, 2011.
- [13] K.A.A. Aziz, R.A. Ramlee, S.I Samsudin and A.N.M. Johari. "The Effect Of Overlapping Spread Value For Radial Basis Function Neural Network In Face Detection", Journal of Telecommunication, Electronic And Computer Engineering, 2010.
- [14] R.A Hamzah, S.F.A. Ghani, A. Din and K.A.A. Aziz. "Visualization of image distortion on camera calibration for stereo vision application", Control System, Computing and Engineering (ICCSCE), 2012.
- [15] R.A. Ramlee, K. Azha and R.S.S. Singh. "Detecting Cholesterol Presence with Iris Recognition Algorithm", Universiti Teknikal Malaysia Melaka (UTeM), Malaysia.
- [16] R.A. Hamzah, S.F. Abd Ghani, A.F. Kadmin and K.A.A. Aziz. "A practical method for camera calibration in stereo vision mobile robot navigation", Research and Development (SCORED), 2012.
- [17] R.A. Hamzah, K.A.A. Aziz, A.S.M. Shokri. "A pixel to pixel correspondence and region of interest in stereo vision application", Computers & Informatics (ISCI), 2012.
- [18] K.A.A. Aziz, S.S. Abdullah and A.N.M. Johari. "Face Detection Using Radial Basis Functions Neural Networks With Fixed Spread", International Journal of Computer Sciences and Engineering Systems, 2011.

# Mineralization in Granitic intrusive Of Kanigiri area in Andhra Pradesh: A root cause for Fluoride Dominance in Ground Water – A Case Study

M.R.S.Sampath Kumar  
Department of Geo-Physics  
Andhra University  
Visakhapatnam-530046  
India

G. Swathi  
Department of Geo-Physics  
Andhra University,  
Visakhapatnam-530046  
India

---

## Abstract:

The Kanigiri-Podili tract of Nellore and Prakasam districts of Andhra Pradesh were known for abnormal fluoride content and interesting mineralogy. Kanigiri town in Topo-Sheet No.57M/11 of Survey of India is surrounded by granitic intrusive. Alkaline magmatism was widespread in the granulite terrain of southern peninsular India during the proterozoic. The forty seven alkaline to mildly alkaline plutons and carbonatite complexes of varying dimensions and shapes cover a total area of approximately 450sq.Km and define an alkaline belt along the east coast of India. The rocks of the area are holocrystalline-hypidiomorphic texture and composed mainly of orthoclase, microcline, albite, and zircon as chief accessory minerals fluorite, topaz, apatite are the other accessories as served in the rock.

The present work focuses on the origin of fluoride in waters around Kanigiri area. In general the dissociation of granitic rocks exposed to prolonged sun and runoff results apatites in to water. This in turn enriches the Fluoride content. But here the mechanism is different. Endemic fluorosis is prevalent amongst the habitants of the high fluorine content in ground water. Streaks and Lenses of fluorite are common feathers in these granites. The earlier workers attributed the origin to the replacement of the existing rocks by “granitic juice” having a high volatile content. Small patches of Sodalite-Cancrinite-Fluorite-Nepheline bearing syenites hosted within the fluorite bearing grey granite near Podili. Detailed water sampling around Kanigiri and Podili has been made. They are analyzed to their complete major-ion analysis.

**Keywords:** fluoride enrichment, ground water, kanigiri, granite

---

## 1. INTRODUCTION

Groundwater chemistry is largely a function of the mineral composition of the aquifer through which it flows. The hydro chemical processes and hydro geochemistry of the groundwater vary spatially and temporally, depending on the geology and chemical characteristics of th aquifer. Hydro geochemical processes such as dissolution, precipitation, ion exchange processes and the residence time along the flow path control the chemical composition of groundwater.

In recent years, monitoring of Fluoride (F-) concentrations in the groundwater has become a great interest to the scientific and research community as this problem is universal. According to the Bureau of Indian Standard (BIS) the maximum tolerable limit of fluoride in Groundwater (GW) is 1.5 ppm.

## 2. MATERIALS AND METHODS

### 2.1. Geology

Prakasam district is surrounded by granitic intrusives. Alkaline magmatism was widespread in the granulite terrain of southern peninsular India during the Proterozoic. The forty seven alkaline to mildly alkaline plutons and carbonatite complexes of varying dimensions and shapes cover a total area of approximately 450 sq.Km

and define an alkaline belt along the east coast of India. The rocks of the area are holocrystalline- hypidiomorphic texture and composed mainly of orthoclase, microcline, albite, and zircon as chief accessory minerals fluorite, topaz, and apatite are the other accessories as served in the rock. The district is underlain by hard rock's 80% followed by alluvium 19% and soft rocks 1%. Geological formations in the study area are covered with pink colored granite rock with red, black cotton and clay soils. The major water source of irrigation in district is Nagarjuna Sagar, Right Bank Canal and Gundlakamma River.

### 2.2 Regional geology of the Study area

The eastern margin of Cuddapah basin, a number of granitic bodies of mesoproterozoic age occur intermittently over a stretch of about 300 Km from Vinukonda in the north to SriKalahasthi in the south. Notable among them are the Vinukonda granite, Darsi granite, Podili granite and Anumonakonda granite. Available trace element data along with the presence of fluorite in all these granites indicate that these granites have crystallized from the partial melting of dehydrated lower continental crust (Sarvothaman and Sesha Sai2010).

The Kanigiri pluton which is located between latitudes The Kanigiri is located between latitude  $15^{\circ}24'30''N$  to  $15^{\circ}24'35''N$  and longitudes  $79^{\circ}30'00''E$  to  $79^{\circ}30'06''E$  and is about 86km WSW of Ongole,

Prakasam district, Andhra Pradesh. Fig1 showing the location of the area. The Kanigiri pluton is elliptical, with NE-SW trending longer axis. It is intrusive into the Dharwar schists of the Nellore- Khammam schist Belt(NSB), and has been dated at 995Ma(Gupta et al 1984). Structural, petrological and petrochemical investigations suggest that the origin of the columbite-bearing granite near Kanigiri, is due to the alteration of the original metasediments by injection of fluids rich in volatiles. The increase in the columbite content in the derived soils adjacent to the Mekeru River suggests that the Mekeru fault served as a conduit for their influx.

The study area covers Kanigiri mandel. Fig1 showing the location of the area. Water sampling was carried out at random covering at least one sample in a square kilometer area. Wherever wells and ponds exist in the study area, samples were collected. The drinking water from bore wells were extracted using hand pumps and well water. Samples were collected in clean and sterile one-litre polythene cans and stored in an icebox. Analysis was carried out for pH, electrical conductivity (EC), total dissolved solids(TDS), total hardness (TH), total alkalinity (TA), chlorides (Cl<sup>-</sup>), sulfates (SO<sub>4</sub><sup>2-</sup>), nitrates (NO<sub>3</sub><sup>-</sup>) and fluorides (F<sup>-</sup>). The analysis for physico-chemical parameters and fluoride in ground and surface water samples was carried out according to the procedure outlined in standard methods. Fluoride (F<sup>-</sup>) was determined by SPANDS reagent method.



Fig1: Location map

### 3. RESULTS AND DISCUSSIONS

#### 3.1. Geochemistry of Fluorine

Fluorine, the lightest of the halogen elements, belongs to group 17 of the periodic table along with F, Cl, Br and I, and is one of most reactive of all elements. It is known that fluorine is an element widely distributed in ore deposits and in accessory minerals in igneous rocks. As a mineralizer fluorine accompanies a large number of metals and it is this property fluorine that makes it a useful indicator in mineral exploration.

Fluorine occurs in many common rock forming minerals, including fluorite CaF<sub>2</sub>, which occurs in both igneous and sedimentary rocks, apatite Ca<sub>5</sub>[PO<sub>4</sub>]<sub>3</sub>(Cl,F,OH), topaz Al<sub>2</sub>F<sub>2</sub>[SiO<sub>4</sub>], simple halides such as carobbite KF, silicates such as muscovite KAl<sub>2</sub>(OH,F)<sub>2</sub>[AlSi<sub>3</sub>O<sub>10</sub>] and a range of amphibole and mica minerals. Substitution of the F-ion for the isoelectronic hydroxyl OH<sup>-</sup> ion is commonplace, because of the similarity in ionic radii, although substitution will not occur if the OH<sup>-</sup> ion is acting as a donor in hydrogen bonding. (Wedephol,1978). Fig 2 illustrates the geochemical mobility of fluorine with respect to the other elements such as As, Ag, U, Cu and Th are in the same range of geochemical mobility as shown by F. The average fluorine contents for granite (800ppm) have limited value as contents range from tens of ppm to several percent and vary greatly within and between different granite types. Fluorine may be concentrated or released by both alkaline and calc-alkaline series.

Extensive research has been carried out on the fluoride-hydroxyl exchange in geological material (Gillberg,1964; Stormer and Carmichael,1971; Ekstrom,1972; Munoz and Ludington,1974). The presence of higher concentrations of fluoride in areas of fluorine-rich rocks is therefore explained on the basis of F<sup>-</sup> = OH<sup>-</sup> interchange between minerals and water. This phenomenon enhances the detection of fluoride anomalies in water in mineralized terrains.

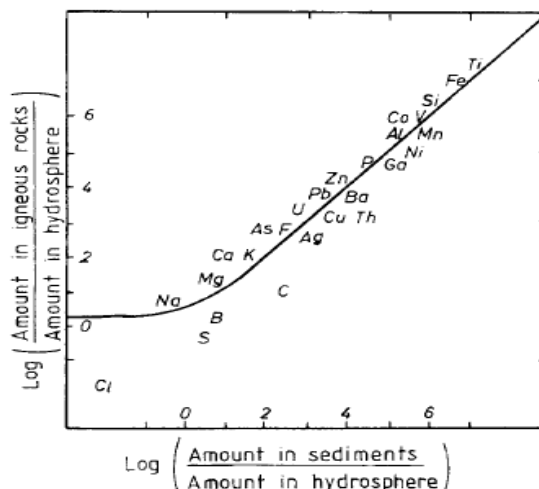


Fig2: showing relative geochemical mobility of Fluorine(after Dissanayake,1986).

#### 3.2. Hydrochemistry of fluorine

Fig 3 shows the distribution of fluoride in ground water of Kanigiri. The obtained fluoride concentrations levels are showing in fig3 corresponding to each water sample of Kanigiri mandel. It is very clear that the highest concentrations of fluoride in the groundwater is recorded upto 14ppm.

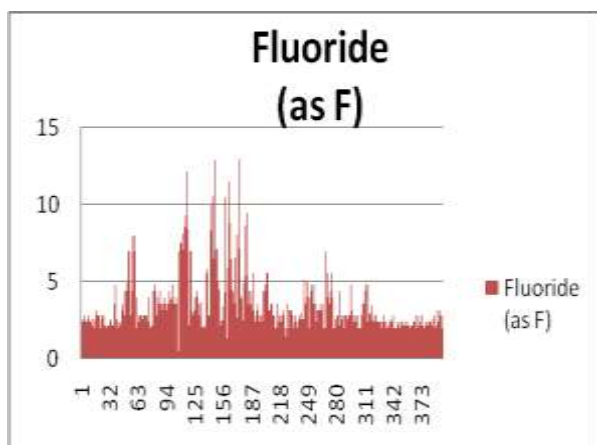


Fig3: Fluoride distribution in groundwater

#### 4. CONCLUSION

The boundary of Kanigiri is associated with plutons is a mineralized belt as evidenced by the discovery of many mineralisations along this granite. Recently people from AMD(Atomic Mineral Division), Hyderabad reported bastnaesite and hydroxyl bastnaesite(lanthum cerium fluoro- carbonate) from the kanigiri granite.Rare metal and rare earth bearing minerals identifies by X-ray diffraction(XRD)studies in Kanigiri granite are bastnaesite

#### 5. REFERENCES

- [1] Sarvothaman,H. and Sessa Sai,V.V.(2010) Global correlations of A-type granites and related rocks, their mineralization and significance in lithospheric evolution.IGCP-510,pp.2-14.
- [2] Gupta,J.N., Pandey,B.K., Chabria,T., Banerjee,D.C. and Jayaram,K.M.V(1984)Rb-Sr geochronological studies on the granites of Vinukonda and Kanigiri,Prakasam district, Andhra Pradesh, India.Pecambrian Res.,v.26,pp. 105 – 109.
- [3] Hand book of Geochemistry Wedephol(1978)
- [4] Gillberg,M., (1964) Halogens and hydroxyl contents of micas and amphiboles in Swedish granitic rocks Geochim.Cosmochim. Acta, 28 : 495-516.
- [5] Stormer.J.C. and Carmichael, I.S.E., (1971) Fluorine-hydroxyl exchange in apatite and biotite: a potential igneous geothermometer. Contrib Mineral. Petrol.,31: 121-131.
- [6] Ekstrom, T.K., (1972) The distribution of fluorine among some coexisting minerals. Contrib. Mineral Petrol., 34: 192-200.
- [7] Munoz and Ludington., (1974) Fluoride – hydroxyl exchange in biotite Am . J. Sci., 274 : 396-413.
- [8] Banerjee,D.C., Maithani,P.B., Ranganth,N. and Jayaram,K.M.V.(1983) Rare metal mineralization in granite rocks of the Kanigiri area in the Prakasam district,Andhrapradesh,India.Chemical geol.,v.39,pp.319-334
- [9] G.Nagendra Babu,M.Sai Baba, Mary K.Kumar, Yamuna Singh(2013) Bastnaesite from Kanigiri granite, Prakasam district, Andhra Pradesh, Journal Geological Society of India, Vol.81, April 2013, pp, 447-450.

and hydroxyl bastnaesite, besides columbite-tantalite, monazite, fergusonite, thorite and euxenite.

The hydrochemistry of fluorine in the region shows a marked increase of fluoride in the ground water at the mineralized belt. It is postulated that the boundary is a deep-seated rift or miniplate boundary along which there was considerable exhalation of fluorine. This process would in all probability have been a result of granite magmatism associated with continental collision. Fluorine appears to have acted as a mineralizes for many metals including Nb,Ta,Sn,U Th, and Rbas shown by the enrichment of these minerals in the Kanigiri Pluton.

Controls on the distribution of water qualities in the study area reflect water-rock interactions (affecting geochemistry); As groundwater flows through the strata of different mineralogical composition, the water composition undergoes adjustments caused by imposition of new mineralogically controlled thermodynamic constraints. The ground water existing in the Prakasam District of Andhra Pradesh State in South India is significantly affected by the excess concentrations of fluoride. The results revealed this alarming concentration of the fluoride in the study area of Prakasam District. The excess fluoride concentration in the study area may be attributed to the geological formation of that particular area and rapid ground water depletion. The water in the study area is not suitable for domestic consumption without prior treatment.

# A Secure Multi-Service Network Connectivity in Cloud Technology

Jayanthi Vagini K  
James College of Engineering  
and Technology  
Kanyakumari, T.N., India

Hemalatha M  
Hindustan College of Arts and  
Science  
Coimbatore, T.N., India

Amarnath C.T.K  
James College of Engineering  
and Technology  
Kanyakumari, T.N., India

---

**Abstract:** Cloud computing transforms the way of information technology (IT) by consuming, managing, promising improved cost efficiencies, accelerated innovation, faster time-to-market, and the ability to scale applications on demand. Here the Secure service is considering a key requirement for cloud computing consolidation as a robust and feasible multipurpose solution. In this paper, we propose secure multi-service network connectivity between on-premises and cloud through various services in cloud environment. To provide dynamic scalability for various applications, there has been an increasing trend in business organizations to outsourcing their data to remote cloud at Cloud Service Provider (CSP). In addition, in order to provide cloud-centric building blocks and infrastructure in the areas of secure application connectivity used by Service Bus and Access Control services, designed specifically to the cloud. All external connections come through a load balancer, which is a key to Cloud computing. Here the two main areas of compute and storage functionality as a cloud service.

**Keywords:** Storage, Service Bus, Access Control, Load Balancer, Cloud Computing;

---

## 1. INTRODUCTION

Cloud computing is one of the most emerging technology trends today. Cloud Computing is often described as “resources accessed via a browser over the Internet.” However, this definition has become increasingly insufficient to characterize the breadth of applications and use cases for the cloud, and the networks that must support them. The US National Institute of Standards and Technology (NIST, <http://csrc.nist.gov>) defines it as follows: Cloud computing is a model for enabling convenient, on-demand network access to a shared pool of configurable computing resources (e.g., networks, servers, storage, applications, and services) that can be rapidly provisioned and released with minimal management effort or service provider interaction. This cloud model promotes availability and is composed of five essential characteristics, three delivery models, and four deployment models. The five key characteristics of cloud computing include on-demand self-service, ubiquitous network access, location-independent resource pooling, rapid elasticity, and measured service [1, 2]. Security, reliability, confidentiality, liability, privacy etc are the main concerns on the topic of cloud computing technique. There are two types of securities threats that arise in cloud and these can be defined as: Internal Threats: These are caused internally in the cloud where the CSP can leak the information of the user or may modify it for its own purpose. The users require that their data remain secure over the CSP and they need to have a strong assurance from the cloud servers that CSP store their data correctly without tampering or partially deleting because the internal operation details of service providers may not be known to the cloud users. External Threats: These are caused by some external agents and outside party who can use the stored data of the user for some wrong purpose or leak or modify and delete the data to fulfill his own requirements. Integrity: It facilitates in the recognition of any alteration that has been occurred in the data stored in cloud. It refers to the protection of data from unauthorized deletion, modification or fabrication or we can say in general it refers to the security of the data from malicious parties. Confidentiality: This ensures that the data has been accessed by the authenticated or authorized parties [3]. **Packaged Software** - With packaged software a customer would be responsible for managing the

entire stack – ranging from the network connectivity to the applications, as shown in Fig. 1. The industry has defined three categories of Cloud Services which are also called as cloud delivery models are software as a service (SaaS), platform as a service (PaaS), and infrastructure as a service (IaaS). The relationship between IaaS, PaaS, and SaaS in cloud services maps to the components in an IT infrastructure, as shown in Fig. 2. **IaaS** - With Infrastructure as a Service, the lower levels of the stack are managed by a vendor. Some of these components can be provided by traditional hosters – in fact most of them have moved to having a virtualized offering. Very few actually provide an OS. The customer is still responsible for managing the OS through the Applications. For the developer, an obvious benefit with IaaS is that it frees the developer from many concerns when provisioning physical or virtual machines. This was one of the earliest and primary use cases for Amazon Web Services Elastic Cloud Compute (EC2). Developers were able to readily provision virtual machines (AMIs) on EC2, develop and test solutions and, often, run the results ‘in production’. The only requirement was a credit card to pay for the services. IaaS – a set of infrastructure level capabilities such as an operating system, network connectivity, etc. that is delivered as pay for use services and can be used to host applications. In IaaS, the cloud provider supplies a set of virtualized infrastructural components such as virtual machines (VMs) and storage on which customers can build and run applications. The application will eventually reside on the VM and the virtual operating system. Issues such as trusting the VM image, hardening hosts, and securing inter-host communications are critical areas in IaaS. **PaaS** - With Platform as a Service, everything from the network connectivity through the runtime is provided and managed by the platform vendor. In fact because we don’t provide access to the underlying virtualization or operating system today, we’re often referred to as not providing IaaS. PaaS offerings further reduce the developer burden by additionally supporting the platform runtime and related application services. With PaaS, the developer can, almost immediately, begin creating the business logic for an application. Potentially, the increases in productivity are considerable and, because the hardware and operational aspects of the cloud platform are also managed by the cloud platform provider,

applications can quickly be taken from an idea to reality very quickly. PaaS – higher level sets of functionality that are delivered as consumable services for developers who are building applications. PaaS is about abstracting developers from the underlying infrastructure to enable applications to quickly be composed. PaaS enables programming environments to access and utilize additional application building blocks. Such programming environments have a visible impact on the application architecture, such as constraints on which services the application can request from an OS. For example, a PaaS environment might limit access to well-defined parts of the file system, thus requiring a fine-grained authorization service. **SaaS** - With Software as a Service, a vendor provides the application and abstracts you from all of the underlying components. SaaS

– Applications that are delivered using a service delivery model where organizations can simply consume and use the application. Typically an organization would pay for the use of the application or the application could be monetized through ad revenue. Finally, in SaaS, the cloud providers enable and provide application software as on-demand services. Because clients acquire and use software components from different providers, crucial issues include securely composing them and ensuring that information handled by these composed services is well protected [4,5].

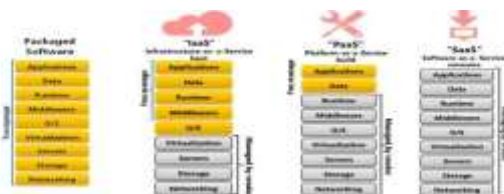


Fig. 1 Packaged software Fig.2 Cloud deliver models as IaaS, PaaS and SaaS

The rest of the paper is organized as follows. Section 2 describes the research background and related work. Section 3 addresses our cloud service architecture and surveys conventional connectivity techniques, and the construction of firewall and load balancing, respectively. In Section 4, we present the security roles and tasks. Finally, we conclude this paper in Section 5.

## 2. BACKGROUND AND RELATED TOOLS

Cloud Platform is a comprehensive PaaS offering including: Cloud OS, Extending Relational Database to the Cloud, and Cloud Service. The Windows Azure platform provides an Internet-based cloud computing environment for running applications and storing data in Microsoft data centers on the world. You can browse to it at <http://windowsazure.com> portal for the Windows Azure platform.

A) The Windows Azure platform consists of the Windows Azure cloud-based operating system, which provides the core compute and storage capabilities required by cloud-based applications as well as some constituent services – specifically the Service Bus and Access Control – that provide other key connectivity and security-related features. Cloud OS computes applications in the cloud and provides storage

application management through Virtual Network, as shown in Fig. 3. The storage services provide storage for binary and text data, messages, and structured data. The storage services include: The Blob service, for storing binary and text data. The Queue service, for storing messages that may be accessed by a client. The Table service, for structured storage for non-relational data. The drives, for mounting an NTFS volume accessible to code running in your Cloud service, Programmatic access to the Blob, Queue, and Table services is available via the Cloud Managed Library and the Cloud storage services REST API. Blobs, tables, and queues hosted in the cloud, close to your computation. Authenticated access and triple replication to help keep your data safe. Easy access to data with simple REST interfaces, available remotely and from the data center, Access is via a storage account – you can have multiple storage accounts per live id.

B) The Windows Azure platform also comes with a cloud-based relational database called SQL Azure™, allowing you to move your on-premises relational databases and logic to the cloud. Relational database model delivered as a service which appears to be a Database server to the client, and deployment of multiple databases across multiple datacenters. Cloud-based relational database provides logical server in the portal that is a Gateway server that understands TDS protocol, execute a create DB Command to create a new database, Looks like Database server to TDS Client, Can add and remove DBs easily from application to scale up and down based on business needs, Actual data stored on multiple backend data node. Logical optimizations supported by Indexes, Query plans etc. Physical optimizations not supported because of File Groups, Partitions etc... and finally transparently manage physical storage.

**Reporting** provided as a service, reports authored using existing tools (BIDS) and uploaded to the cloud, reports can have rich Data Visualizations (Maps, Charts, Tables) and be exported to variety of rendering formats (Excel, Word, PDF), reports can be rendered as part of an app using the Report Viewer control, Directly view the reports in the browse, Web Service interface to render and manage reports.



Fig. 3 Cloud-based OS Service



Fig. 4 Cloud-based relational database

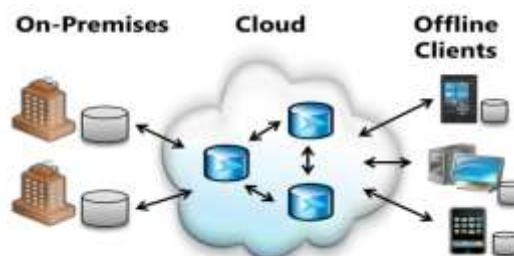


Fig.5 On-premises with cloud and Offline

C) Cloud Service provides services that can be used by any apps – hosted in Cloud OS, on-premises, or hosted in another environment, as shown in Fig. 6.



Fig. 6 Cloud service

These services are really key components you would need for building distributed, connected applications. we talk about connecting to your existing on-premises applications and enabling the composition of hybrid (Cloud + on-premises) applications.

There are currently two Services: the Service Bus & the Access Control Service. The Service Bus and Access Control Services that were once collectively known as the .NET Services now run directly within Windows Azure.

Windows Azure now provides secure connectivity natively via Service Bus and Access Control, in much the same way that it also provides compute and storage as a cloud service.

Windows Azure is an operating system as a service – you can think of it as Windows in the cloud. It provides a cloud computing fabric, hosted within Microsoft data centers, for creating, deploying, managing, and distributing applications and services on the Internet, as shown in Fig. 7.

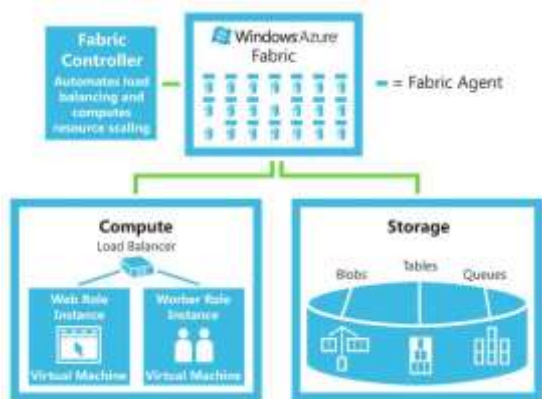


Fig. 7 Windows Azure Fabric

The Windows Azure fabric provides two main areas of functionality: compute (e.g., executing an application) and storage (e.g., storing data on disk), the foundational building blocks for all cloud applications.

In addition to these core services, Windows Azure also comes with Service Bus and Access Control capabilities, which make it easier to extend your .NET applications into the cloud.

**Compute:** The compute service offered by Windows Azure makes it possible to “execute” your applications in the cloud. The compute service provides you with a way to run your applications on a Windows Server running in a virtual machine hosted in Microsoft data center. When you deploy and application to Windows Azure, you’re deploying it to execute within this type of highly-scalable environment. It’s important to note that the Windows Azure storage services are designed to be very simple and highly scalable.

**Storage:** They provide fundamental services for BLOB storage, queue storage, and simple table storage. You interact with these services through a simple REST API based on HTTP requests. You manipulate data in the storage services through traditional POST, PUT, and DELETE requests, and your retrieve information from the storage services using simple GET requests. This approach makes it possible for anyone to integrate with the storage services, regardless of their platform.

Today the Service Bus and Access Control provide core functionality related to secure application connectivity and federated access control as described here:

**Service Bus** provides network infrastructure for connecting applications over the Internet, using a variety of different messaging patterns, in a way that’s capable of traversing firewalls and NAT devices without forfeiting the security afforded by these devices, shown in Fig. 8.

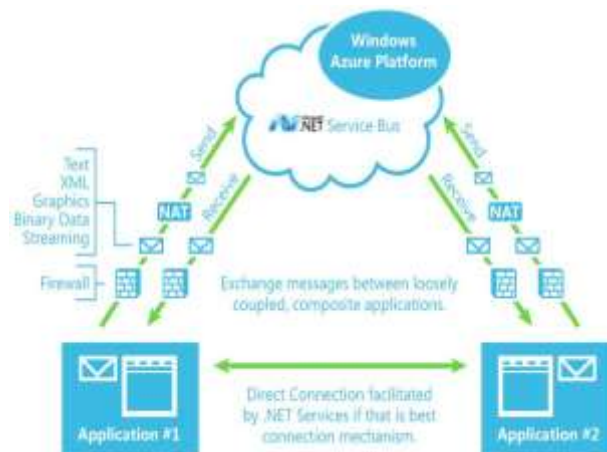


Fig. 8 Service Bus Access Control

**Access Control** provides claims-based access control in the cloud. It includes a claims transformation engine that federates with identity providers like ADFS v2 (Active Directory Federation Services), as shown in Fig. 9.



Fig. 9 Access Control

**Cache** is a distributed, in-memory application cache for cloud applications. There are two primary use cases for the Cache. First a session state provider for cloud applications. Secondly

a data cache layer for Cloud Applications that use Relational Databases or Cloud Storage. It's important to understand that Cache is provided as a service. Instead of having to install or manage software on machines or instances, you simply provision, configure, and use the service. This service abstraction also provides more flexibility – so you can dynamically increase or decrease the cache size as needed. Finally, with Cache is uses the same programming model for both the cloud and on-premises. Each of these services is available using open protocols and standards, including REST, SOAP, Atom/Atom Pub, which means developers on any platform can easily integrate with them, referred from [6, 7, 8, and 9].

### 3. ARCHITECTURE AND TECHNIQUES

This section explores a strong security assurance to the users based on secure multi-service network connectivity in the cloud computing environments. The work mainly used for Identity and Access control services in cloud servers from untrusted and outsourced storages.

We introduce cloud service architecture for key points here is that all external connections come through a load balancer, this includes storage. Inter-role communication (notice there is no load balancer) and TCP ports directly to Worker Roles (or Web Roles). We will still use the storage to communicate async and reliably via queues for a lot of options. However, inter-role communication fills in when you need direct synchronous communication. The load balancers are a key to Cloud computing, as shown in Fig. 10.

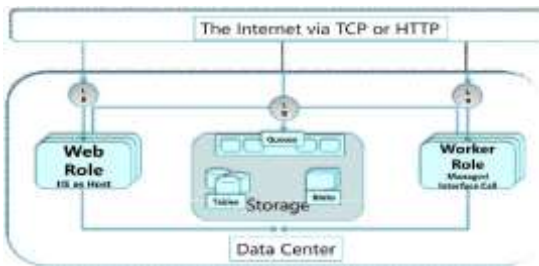


Fig. 10 Cloud Service Architecture.

For example, User uploads large image file, Image inserted into blob storage, Message placed on queue incl BLOB URI and metadata, Worker role is polling queue. Reads message from queue, Worker role processes message, reads from BLOB storage, generates thumbnail, Thumbnail and metadata stored in Table storage, Message deleted from queue. Finally, Cloud Service supports standard IP protocols. Enables hybrid apps access to on-premises servers. Allows remote administration of cloud apps. Simple setup and management. Integrated with cloud Service Model. And also Web, Worker and VM Roles supported. In order to improve secure multi-service network connectivity between on-premises and cloud, we make use of following techniques to construct new applications and challenges.

**Service Bus:** One of the most common needs in large-scale distributed applications is application connectivity. In fact, application integration is usually one of the most costly and

troublesome areas of IT. Today it's common for many organizations to use an enterprise service bus (ESB) solution to address these challenges, as shown in Fig. 11.

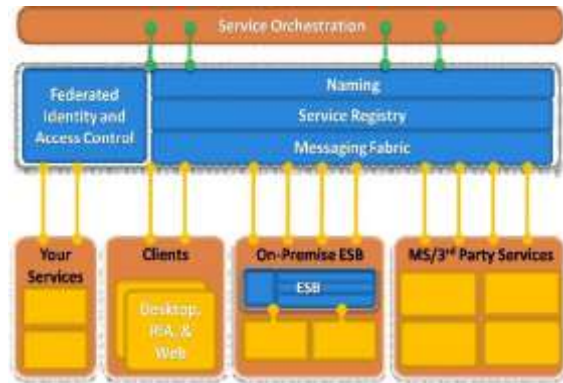
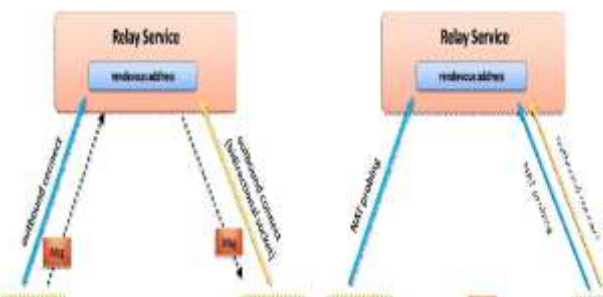


Fig. 11 Internet Service Bus

Tackling bidirectional communication at Internet scope is not trivial due to some of today's networking realities. The Service Bus is designed to provide a general purpose application bus, available on the internet at internet scale. You can really thin of the Service Bus as being similar to an Enterprise Service Bus that many enterprise organizations have today. However, we believe that when providing a Service Bus as a programmable service on the internet, there are a wider range of scenarios for many more types of organizations. Fundamentally, the .NET Service Bus is about connecting applications across network and application boundaries and making key message exchange patterns such as publish and subscribe messaging very simple.

The Access Control service is designed to provide rules-driven, claims-based access control for applications. Essentially, this allows you to define authorization rules for your applications using the claims-based approach that we are adopting within many Microsoft products and technologies and that is becoming adopted in the industry. Here's how it works: the on-premises service connects to the relay service through an outbound port and creates a bidirectional socket for communication tied to a particular rendezvous address. Network policy managed through cloud portal. Granular control of connectivity between cloud roles and external machines. Automatic setup of IPsec through Tunnel firewalls/NAT's through hosted SSL-based relay. Network policies enforced & traffic secured via end-to-end certificate-based IPsec. DNS name resolution based on endpoint machine names.

**Relayed Connectivity:** Despite these connectivity challenges, some of today's most popular Internet applications are inherently bidirectional. Consider things like instant messaging, online multiplayer games, and peer-to-peer file sharing applications that use protocols such as Bit Torrent, which accounts for a large percentage of all Internet traffic today. These applications have written the low-level networking logic to traverse firewalls and NAT devices, and to create direct peer-to-peer connections when possible. They typically accomplish this through a central relay service that provides the connectivity logic, as shown in Fig. 12.



Role and Web/Worker Role.

#### 4. SECURITY ROLES AND TASKS

Roles are defined in a Service Model, may define one or more Roles per Service. A role definition specifies VM size, Communication Endpoints, Local storage resources, etc. At runtime each Role will execute on one or more instances (up to 20 per subscription). A role instance is a set of code, configuration, and local data, deployed in a dedicated VM. The Service model defines the shape of a service- the roles it will have, endpoints it will listen on and types of VMs that will be run. At runtime each role will run at a given scale. Specifically each role will be deployed onto and executed on one or more VMs. A VM runs a single role. The various security roles involved in running a cloud account.

Cloud OS currently supports the following two types of roles: A web role is a role that is customized for web application programming as supported by IIS 7 and ASP.NET. A worker role is an executable (you can create your own web server, host a database, etc.). Inbound on any TCP Port, HTTP/HTTPS. A worker role is a role that is useful for generalized development, and may perform background processing for a web role. A web role is hosted on IIS, HTTP/HTTPS, ASP.NET, Fast CGI + PHP. A service must include at least one role of either type, but may consist of any number of web roles or worker roles.

A worker role is started by a call to a well know managed code interface RoleEntryPoint. A worker role must extend this class and override the Start() method.

**Role Lifecycle:** All roles may extend RoleEntryPoint, Roles report status via RoleEnvironment. The fabric calls RoleEntryPoint methods as it starts and stops a role. CloudWorkerHost process is started. Worker Role assembly is loaded and surfed for a class that derives from RoleEntryPoint. This class is instantiated. RoleEntryPoint.OnStart() method is called. Called by Fabric on startup, allows you to perform initialization tasks. Reports Busy status to load balancer until you return true. RoleEntryPoint.Run() method is called. Main logic is here – can do anything, typically infinite loop. Should never exit. If the RoleEntryPoint.Run() method exits, the RoleEntryPoint.OnStop() method is called when role is to be shutdown, graceful exit. 30 Seconds to tidy up. CloudWorkerHost process is stopped. The role will recycle and startup again. As a role changes state it will raise the Status Check event. A status of Busy will mean the load balancer will not route requests to the instance, as shown in above Fig. 15.



Fig. 15 Role Lifecycle

**Virtual Machine Role:** The role is the VM. Use Windows services, scheduled tasks, etc. You configure and maintain the OS. Provided to help you move applications to Cloud OS, it enables you to have full control over the OS image, create

Fig. 12 Establishing a Relay Connection

Fig.13 Establishing a Direct Connection

**Direct Connectivity:** In addition to relayed communications, the Service Bus also provides a capability for establishing direct connectivity between clients and services in order to improve performance and throughput. Clients and services still communicate with the relay through a common rendezvous address but then the relay tries to help them connect directly to one another in order to avoid future relayed transmissions, as shown in above Fig. 13.

**The High Scale Application Archetype:** High scale applications often follow this sort of a pattern as Inbound connectivity comes through a load balancer(LB), Requests are round robin routed, Load balancer is typically aware of the state of the web servers (i.e. are they up). There are one or more tiers or groups of stateless web or app servers; by stateless we mean that they do not hold state between client requests. Stateless means that simple load balancing works. Stateless means that the failure of a web server does not cause major issues for application- it is simply removed from the load balancer. Applications will often perform processing in the background. Improves response time for users, Allows load peaks to be buffered in queues, as shown in Fig. 14.

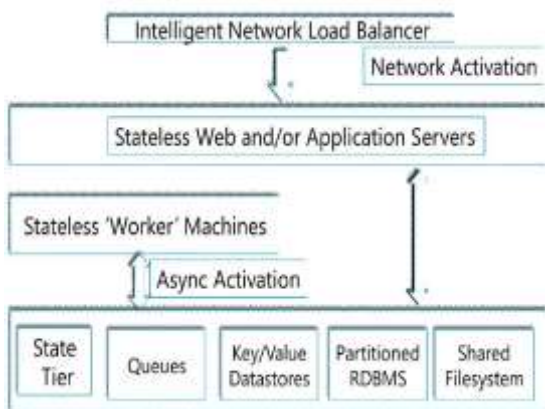


Fig. 14 Inbound Connectivity with Load Balancer

To realize these functions, our cloud service is comprised of four roles: Web Role, Worker Role, Admin Role, and also VM Role. The above techniques involving some procedures based on roles. Moving Applications to the Cloud with VM

your VHD locally, upload the VHD to storage, deploy a service package that uses the custom OS image, Specify `<OsImage href="20101020BaseVM.vhd" />` in the .csfzg., as shown in Fig. 16.



Fig. 16 VM Role with Web/Worker Role

#### Admin Access & Startup Tasks:

**Task Types:** Simple [Default] – System waits for the task to exit before any other tasks are launched. Background – System does not wait for the task to exit. Foreground – Similar to background, except role is not restarted until all foreground tasks exit.

## 5. CONCLUSION

In this paper, we presented a construction of secure multi-service network connectivity through a various services for cloud applications to avoid security risks. We also focused on how cloud delivery models helps to provide dynamic scalability to outsourcing their data to remote cloud and surveys connectivity between cloud roles and external machines, and the construction of firewall and load balancing in the areas of secure application connectivity and federated access control via Service Bus and Access Control services. The contribution of the paper is to understand how the on-premises service connects to the relay service through an outbound port and creates a bidirectional socket for communication tied to a particular assignation address, the two main areas of compute and storage functionality as a cloud service and cloud computing platform, respectively.

## 6. REFERENCES

1. Cloud Security Alliance, "Security Guidance for Critical Areas of Focus in Cloud Computing V3.0," released in 2009, permanent archives at <http://www.cloudsecurityalliance.org/guidance/csaguide.v.0.pdf> D. Catteddu and G. Hogben, "Cloud Computing: Benefits, Risks and Recommendations for Information Security," ENISA, 2009; [http://www.enisa.europa.eu/act/rm/files/deliverables/cloud-computing-risk-assessment/at\\_download/fullReport](http://www.enisa.europa.eu/act/rm/files/deliverables/cloud-computing-risk-assessment/at_download/fullReport).
2. "Architecture and Applications of a Versatile Small- Cell, Multi-Service Cloud Radio Access Network Using Radio-over-Fiber Technologies" Liang Zhang is currently with the State Key Lab of Advanced Optical Communication Systems and Networks, Shanghai Jiao Tong University, Shanghai, China 200240.
3. Kartik Sharma, Renuka Sharma, Gitesh Dalal, "A Secure Protocol for Data storage Security in cloud computing"- International Journal of Scientific & Engineering Research, Volume 4, Issue 6, June-2013 2348 ISSN 2229-5518.
4. Hassan Takabi and James B.D. Joshi, University of Pittsburgh , Gail-Joon Ahn, Arizona State University, "Security and Privacy Challenges in Cloud Computing Environments"- THE IEEE COMPUTER AND

RELIABILITY SOCIETIES, Nov/Dec 2010, pp.24-31,1540-7993/10.

5. A Developer's Guide to Service Bus in Windows Azure AppFabric..<http://go.microsoft.com/fwlink/?LinkID=1504>
6. A Developer's Guide to Access Control in Windows Azure AppFabric<http://go.microsoft.com/fwlink/?LinkID=150835>, <http://www.windowsazure.com>
7. Hung-Chang Hsiao, Tainan, Hsueh-Yi Chung, National Cheng Kung University, Tainan, Haiying Shen, Clemson University, Clemson, Yu-Chang Chao, Industrial Technology Research Institute South, Tainan, " Load Rebalancing for Distributed File Systems in Clouds"- IEEE Transactions on Parallel and Distributed Systems (TPDS) , May 2013, Volume 24, Issue 5, pp. 951-962, ISSN : 1045-9219
8. David Chappell is Principal of Chappell & Associates ([www.davidchappell.com](http://www.davidchappell.com)) in San Francisco, California, Windows%20SSO%20v1%200-- Chappell.pdf.
9. "Network Implications of Cloud Computing" 2011 Technical Symposium at ITU Telecom World.

# Formulating the Data-Flow Modeling and Verification for Workflow: A Petri Net based Approach

Cong LIU

Department of Computer  
Science, Shandong University  
of Science and Technology,  
Qingdao 266590, China

Qingtian ZENG\*

Department of Computer  
Science, Shandong University  
of Science and Technology,  
Qingdao 266590, China

Hua DUAN

Department of Mathematics,  
Shandong University of  
Science and Technology,  
Qingdao 266590, China

---

**Abstract:** Control-flow and data-flow modeling and verification are two important challenges for traditional workflow management. To formulate the data-flow modeling and verification, a Petri Net based approach is proposed in this paper. More specifically, the WFIO-net, which is a kind of WF-net by extending each activity with its read and write data sets, is first presented to model both the control-flow and data-flow information in a workflow process. Moreover, the firing rule of WFIO-net which is different from traditional Petri net is discussed in detail. Then the formal definitions of three basic types of data-flow errors, including missing data, redundant data and conflicting data are formulated using WFIO-net. Next, a polynomial complexity algorithm which is capable of detecting the above-mentioned three kinds of basic data-flow anomalies is proposed based on the activity-data incidence matrix of the WFIO-net. A running case of a property loan approval business process is given to validate the proposed method.

**Keywords:** workflow data-flow modeling and verification; Petri net, WFIO-net and its firing rule, activity-data incidence matrix

---

## 1. INTRODUCTION

Workflow Management, which focuses on the automation of business processes, has received considerable attention in recent years due to its potential for significantly increasing productivity and saving costs. A workflow is a representation of a given process that is made up of well-defined collection of activities, also referred to as tasks. In recent days, workflow structural correctness verification (also refers to as control-flow perspective) [1]-[2] has received much more attention than the other aspects. However, a complete workflow description requires to characteristic the other perspectives, including time, resource, data and etc. Time management [3]-[4] is an important aspect for workflow modeling, analysis and verification. In addition to structural and temporal constraints, resource constraints are also of vital importance in workflow management, because activities in a workflow usually need to access some resources during their execution [5]-[6]. Similarly, the role of data is also important, e.g. routing choices in a process are typically determined by certain data element, which indicates that the control-flow, to some extent, is data-dependent. Unfortunately, the data-flow can be erroneous itself. Towards this issue, data-flow modeling and correctness verification are highly intensified in [7]-[12].

As a tool to model and analyze physical systems, Petri nets [13]-[16] have shown great power in dealing with concurrences and conflicts. As mentioned by Aalst [1] there are at least three reasons for using Petri nets to model and analyze workflows: (1) Graphical nature and formal semantics have been defined for Petri nets; (2) Petri nets are state-based instead of event-based, so the state of the case can be modeled explicitly in Petri nets; and (3) Petri nets are characterized by the availability of many analysis techniques. In this paper, we formulate the data-flow modeling and verification for workflows based on a kind of extended Petri net with data elements. More specifically, our research goal is to develop a systemic formal methodology for characterizing the data-flow modeling and verification. The contribution of this paper is two-fold. In the first place, Petri net-based model for workflow in terms of control-flow and data-flow are presented

to formulate the workflow execution semantic. Secondly, formal specifications of three kinds of data-flow errors and corresponding detection algorithm are given, based on which their correctness verification is conducted.

The remainder of this paper is organized as follows. Section 2 discusses the related work. Section 3 introduces a typical scenario of a property loan approval business process. In Section 4, the WFIO-net, which is a WF-net by extending each activity with its read and write data sets, is proposed to model the data-flow aspect. Section 5 addresses the verification of three kinds of data-flow errors using the activity-data incidence matrix of the WFIO-net. Finally, Section 6 draws conclusions and points our future research scope.

## 2. RELATED WORK

The importance of data-flow verification in workflow is first mentioned in [7]. There several potential data-flow problems are identified. However, no formal models as well as modeling approaches are presented and only basic data errors are defined, however, no formal validation methods are involved. Another idea is to integrate data-flow into process models. The idea behind this approach is to define an extension for a workflow model so that data-flow can be shown with the control-flow. Based on Petri Net formalism containing three building blocks, storage, reactive and transformational units, an extended version of Dual Workflow Nets is proposed in [8]. Unfortunately, this model is complex even for small running-examples and no indication about how this model can be created. Du et al. proposed an approach called Data-Flow Skeleton Filled with Activities (DFSFA) in [9]. Basically, the workflow process is derived from the data-flow skeleton and then is filled with activities. More specifically, a data-flow dependency tree is first generated based on the data dependency. Next step is to generate the data-flow skeleton and then fills it with activities. A more complete approach is provided in [10], where a data-flow matrix and various relations between data and activities are defined. Then, some data-flow errors are conceptualized using UML diagrams and supporting verification algorithms are discussed. This work was further extended and generalized in

[11]. More recently, a survey on data-flow modeling of business processes is presented by DOLEAN and PETRUSEL [12]. They pointed that (1) data is essential in a process and activities need data; (2) without data or without data available on time, the control-flow cannot be executed; (3) there is no model showing a clear data-flow perspective focusing on how data changes during a process executing.

According to these literature reviews, it is easy to conclude that existing researches on data-flow modeling and verification suffer at least the following limitations: (1) no formal model with executing semantic is addressed. Although the model in [8] is proposed by extending Petri net, the firing rule is destroyed; and (2) no formal verification is investigated based on formal models.

### 3. A RUNNING EXAMPLE

A typical scenario of a property loan approval business process mainly includes the following steps: (1) To start the application, an application is received; (2) Then, the completeness of the application is verified; (3) To determine the applicant's qualifications, the financial service company first verifies the applicant's employment status; (4) To qualify the applicant, the financial service company checks the applicant's credit history; (5) At the same time, the financial company also checks the applicant's liquid assets; (6) If the applicant is qualified, the interest rate is determined in for a certain period; (7) The loan application is then evaluated; (8)

If the applicant agrees with everything, the applicant signs the application; (9) The loan officer for signature.

According to the abovementioned steps, we can distil the activity information, including their name, meaning, connection relation and read/write data set is shown in Table 1. Table 2 gives the meaning of each data elements.

### 4. MODELING APPROACHES BASED WFIO-NET

Modeling approaches of business processes have been studied for decades, and some excellent models such as, WF-net, XPDL, BPMN and etc. [18], have been widely applied. Our work is based on Petri net, WF-net to be more precise. We assumed that readers are familiar with the basic concepts of WF-net [1]-[2] and Petri nets [13]-[18]. Some of the essential terminologies and notations are listed as follows.

A tuple  $N=(P, T; F)$  is named a net if the following conditions are satisfied: (1)  $P \cap T = \emptyset$  and  $P \cup T \neq \emptyset$ ; (2)  $F \subseteq (P \times T) \cup (T \times P)$ ; (3)  $Dom(F) \cup Cod(F) = P \cup T$ ; where  $Dom(F) = \{x \in P \cup T \mid \exists y \in P \cup T: (y, x) \in F\}$  and  $Cod(F) = \{x \in P \cup T \mid \exists y \in P \cup T: (x, y) \in F\}$ . For all  $x \in P \cup T$ , the set  ${}^*x = \{y \mid y \in P \cup T \wedge (y, x) \in F\}$  is the pre-set of  $x$ , and  $x^* = \{y \mid y \in P \cup T \wedge (x, y) \in F\}$  is the post-set of  $x$ .

*Definition 4.1* A Petri net is a 4-tuple  $\Sigma=(P, T; F, M_0)$ , where

**Table 1 Activity Information of this Property Loan Approval Process**

Activity Name	Meaning	Pre-activities	Write Date	Read Data
$A_1$	Receive application	$\emptyset$	$\{D_1, D_2, D_3\}$	$\emptyset$
$A_2$	Verify completeness of the application	$\{A_1\}$	$\{D_4\}$	$\{D_1, D_2, D_3\}$
$A_3$	Verify employment status	$\{A_2\}$	$\emptyset$	$\{D_5\}$
$A_4$	Check credit history	$\{A_2\}$	$\emptyset$	$\{D_5\}$
$A_5$	Verify liquid asset	$\{A_2\}$	$\emptyset$	$\{D_5\}$
$A_6$	Determine interest rate	$\{A_3, A_4, A_5\}$	$\{D_5\}$	$\{D_6\}$
$A_7$	Evaluate loan application	$\{A_6\}$	$\{D_6, D_7\}$	$\{D_8\}$
$A_8$	Contact applicant for agreement	$\{A_7\}$	$\{D_8\}$	$\{D_9\}$
$A_9$	Forward to loan officer for signature	$\{A_8\}$	$\{D_9\}$	$\{D_{10}\}$

**Table 2 Data Information of this Property Loan Approval Process**

Data Name	Meaning	Data Name	Meaning
$D_1$	Applicant name	$D_6$	Interest rate
$D_2$	Loan amount	$D_7$	Current owner of property
$D_3$	Annual income	$D_8$	Evaluation result
$D_4$	Application complete	$D_9$	Signed by applicant
$D_5$	Applicant qualified	$D_{10}$	Signed by loan officer

$N=(P, T; F)$  is a net, and  $M_0: P \rightarrow Z^+$  is the initial marking of  $\Sigma$  where  $M(p)$  represents the number of tokens in place  $p$  and  $Z^+$  is a non-negative integer set.

We usually use a rectangle to represent a transition, a circle to represent a place, and a dot to represent a token. An initial marking is denoted by  $M_0$ .  $p$  is marked by  $M$  iff  $M(p) > 0$ . A transition  $t \in T$  is enabled under  $M$ , if and only if  $\forall p \in \bullet t: M(p) > 0$ , denoted as  $M[t >]$ . If  $M[t >]$  holds,  $t$  may fire, resulting in a new marking  $M'$ , denoted as  $M[t > M']$ , such that  $M'(p) = M(p) - 1$  if  $\forall p \in \bullet t \setminus \overset{\circ}{t}$ ,  $M'(p) = M(p) + 1$  if  $\forall p \in \overset{\circ}{t} \setminus \bullet t$ , and otherwise  $M'(p) = M(p)$ .

A Petri net which models a workflow process is called the workflow net (WF-net) whose definition is summarized following [1]-[2].

**Definition 4.2** A Petri net  $\Sigma=(P, T; F, M_0)$  is a WF-net if: (1) There is one source place  $p_s \in P$  such that  $\bullet p_s = \emptyset$ ; (2) There is one sink place  $p_e \in P$  such that  $p_e \bullet = \emptyset$ ; (3) Each node  $x \in P \cup T$  is on a path from  $p_s$  to  $p_e$ ; and (4)  $\forall p \in P, M_0(p) = 1$  if  $p = p_s$ , and otherwise  $M_0(p) = 0$ .

The WF-net is capable to model the control of business where the transition set  $T$  is used to represent the activities, and source place and sink place represent the start and end of the process respectively. The WF-net model of the property loan approval business process in Section 3 is shown in Figure 1. This workflow is composed of nine activities, denoted by  $t_{A_i} = \{i/i \in Z_9\}$  where  $Z_9 = \{1, 2, \dots, 9\}$ .

However, the WF-net can only represent the logic relation of workflow, i.e. the control-flow aspect. To model the data-flow elements of a workflow, we propose the WFIO-net, which is a WF-net by extending each activity with its input and output data sets.

**Definition 4.3**  $\Sigma_{IO}=(P, T; F, I, O, M_0)$  is a WFIO-net if the following conditions are satisfied:

- (1)  $P = P_D \cup P_L$  and  $P_D \cap P_L = \emptyset$  where  $P_D$  is a data place set and  $P_L$  is a logic place set;
- (2)  $T = T_A \cup T_L$  and  $T_A \cap T_L = \emptyset$  where  $T_A$  is an activity transition

set and  $T_L$  is a logic transition set;

(3)  $F = F_L \cup F_D$  where  $F_L \subseteq (P_L \times T_L) \cup (T_L \times P_L)$  is the logic flow and  $F_D \subseteq (P_D \times T_D) \cup (T_D \times P_D)$  is the data flow;

(4)  $I: T_A \rightarrow P_D, \forall t_a \in T_A, I(t_a)$  is the input data set of activity  $t_a$ ; and

(5)  $O: T_A \rightarrow P_D, \forall t_a \in T_A, O(t_a)$  is the output data set of activity  $t_a$ ; and (6)  $\forall p \in P, M_0(p) = 1$  if  $p = p_s$ , otherwise  $M_0(p) = 0$ .

Control-flow structure can be represented by the  $(P_L, T_L; F_L, M_{0|L})$  which is same with the traditional WF-net. The main differences between WFIO-net and WF-net lie in: (1) Two components are involved in the place set, i.e.,  $P = P_L \cup P_D$ , data place set ( $P_D$ ) which is drawn in double circles is separated from the logic place set ( $P_L$ ); and (2) The firing rule of the transition is different from that of a standard one. All data elements are initially undefined, thereby each data place does not contain any token in the model before execution.

There two kinds of flow relation in a WFIO-net, one kind to represent token flow ( $F_L$ ) which is same with the classical one and the other kind is used to represent the data flow ( $F_D$ ). Graphically, a token flow is drawn by direct arc end with arrow while the data flow is represented with direct arc end with small circle. The pre-set of a transition  $t$  contains two parts, formally denoted as  $\bullet t = \overset{\circ}{t} \cup \overset{\circ}{t}$  where  $\overset{\circ}{t}$  is the logic pre-set of  $t$  while  $\overset{\circ}{t}$  is its data pre-set of  $t$  (or read place set). Similarly, the post-set of a transition  $t$  also contains two parts, formally denoted as  $t \bullet = \overset{\circ}{t} \cup \overset{\circ}{t}$  where  $\overset{\circ}{t}$  is the logic post-set of  $t$  while  $\overset{\circ}{t}$  is its data post-set (or write place set). For example, the Figure 2 (a) gives a simple transition model of WFIO-net, we have its pre-set is  $\bullet t_a = \{p_1, p_{read}\}$ , logic pre-set  $\overset{\circ}{t}_a = \{p_1\}$  and read place  $\overset{\circ}{t}_a = \{p_{read}\}$ . The post-set of  $t_a$ , denoted as  $t_a \bullet = \{p_2, p_{write}\}$ , logic post-set  $\overset{\circ}{t}_a = \{p_2\}$  and write place  $\overset{\circ}{t}_a = \{p_{write}\}$ .

A transition  $t \in T$  in a WFIO-net is enabled under  $M$ , if and only if  $\forall p \in \bullet t: M(p) > 0$ , denoted as  $M[t >]$ . If  $M[t >]$  holds,  $t$  may fire, resulting in a new marking  $M'$ , denoted as  $M[t > M']$ , such that  $M'(p) = M(p) - 1$  if  $\forall p \in \overset{\circ}{t} \setminus \bullet t$ ,  $M'(p) = M(p) + 1$  if  $\forall p \in \bullet t \setminus \overset{\circ}{t}$ , and otherwise  $M'(p) = M(p)$ .

A WFIO-net model for single activity is drawn in Figure 2 and the following explanations are given: (1)  $p_{read}$  and  $p_{write}$

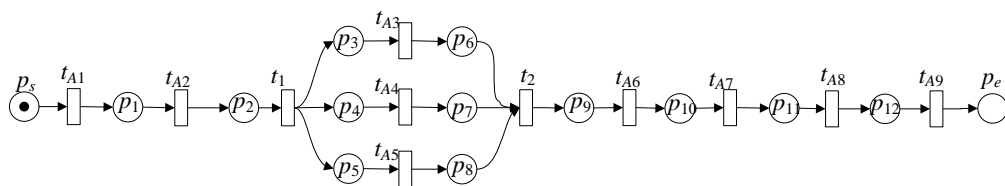


Figure 1 WF-net of the Property Loan Approval Business Process

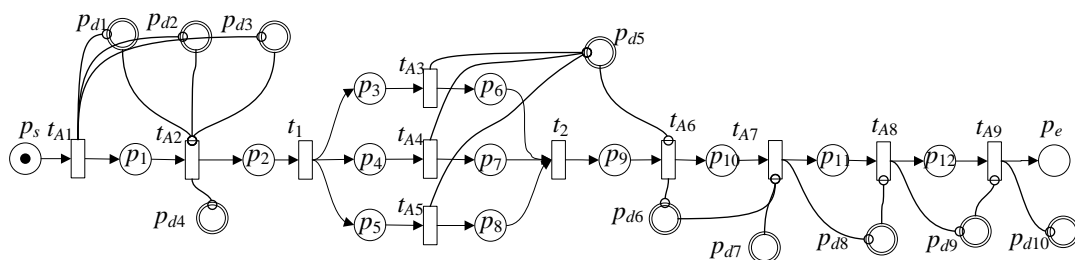


Figure 3 WFIO-net of the Property Loan Approval Business Process

are used to represent the data places and  $p_1$  and  $p_2$  are used to represent the logic places; (2)  $t_a$  is enabled in Figure 2 (a) as both  $p_1$  and  $p_{read}$  has token; and (3) Figure 2 (b) shows the state after firing  $t_a$  where the token in  $p_1$  is removed to  $p_2$  and  $p_{write}$  obtains one token without removing the token in  $p_{ready}$ .

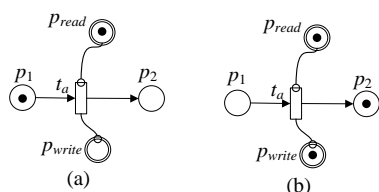


Figure 2 WFIO-net of Single Activity (a) Enabled State, (b) Fired State

The WFIO-net model of the property loan approval business process in Section 3 is demonstrated in Figure 3. The involved data elements are denoted by  $p_{dj}=\{j \mid j \in Z_{10}\}$ , where  $Z_{10}=\{1,2,\dots,10\}$ .

## 5. VERIFICATION OF DATA-FLOW BASED ON WFIO-NET

In this section, data-flow verification of workflow is performed on the basis of WFIO-net. As proved by Sun *et al.* [10], missing data, redundant data and conflicting data are defined as the basic data-flow anomalies. Other types of data-flow errors that are proposed by Sadiq *et al.* [7] can be represented by these three basic ones. Therefore, we restrict our verification scope to these three basic data-flow errors.

### (1) Missing Data

When a data element is accessed without initialization, in this case a missing data anomaly occurs, which is the same as the variable use without definition and initialization in programming. Its formal definition is given in Definition 5.1.

**Definition 5.1** Let  $\Sigma_{IO}=(P, T; F, I, O, M_0)$  be a WFIO-net,  $\forall p_d \in P_D, p_d$  is a missing data if (1)  ${}^{\circ}p_d = \emptyset$ ; and (2)  $p_d^{\circ} \neq \emptyset$ .

In Definition 5.1, the first criterion means that the data element is not initialized by an activity, and the second criterion shows this data will be used by an activity. Missing data can cause system exception and dangling and therefore should be detected before system enactment.

### (2) Redundant Data

If an activity produces data items that do not contribute to the production of the final output data, then there is a redundant data anomaly, i.e. a data element is produced by one activity but never used by other activities. This is same as the variable defined but never used in programming.

**Definition 5.2** Let  $\Sigma_{IO}=(P, T; F, I, O, M_0)$  be a WFIO-net,  $\forall p_d \in P_D, p_d$  is a redundant data if (1)  ${}^{\circ}p_d \neq \emptyset$ ; and (2)  $p_d^{\circ} = \emptyset$ .

In Definition 5.2, the first criterion means that the data element is initialized by an activity, and the second criterion shows this data will never be used by an activity. Redundant data can cause system inefficiency and therefore should be detected before system enactment.

### (3) Conflicting Data

In a workflow instance, if there exist different versions of the same data element, conflicting data anomalies occur. For example, more than one activity attempts to initialize (write) the same data element in one workflow instance.

**Definition 5.3** Let  $\Sigma_{IO}=(P, T; F, I, O, M_0)$  be a WFIO-net,  $\forall p_d \in P_D, p_d$  is a conflicting data if (1)  ${}^{\circ}p_d \neq \emptyset$ ; (2)  $p_d^{\circ} \neq \emptyset$ ; and (3)  ${}^{\circ}p_d \geq 2$ .

In Definition 5.3, the first and third criteria show that the data element is initialized by more than one activity, and the second criterion shows this data will be used by an activity. Conflicting data can cause uncertainty or even confusion and therefore should be detected before system enactment.

In the following, we propose an approach to detect these three basic kinds of data-flow errors. Before rendering our specific detection algorithm, we would like to introduce the activity-task incidence matrix of a WFIO-net.

According to [13], any Petri net can be represented as an incidence matrix. Traditional incidence matrix shows the control-flow relation but no data-flow informal is reflected.

**Definition 5.4** Assume that  $M$  is an  $m \times n$  ( $m$  rows,  $n$  columns) matrix, where  $m$  is the number of transitions (activities) and  $n$  is the number of data places in a WFIO-net. For each position  $[i, j]$  in the matrix, place a “1” in the position if transition  $i$  has input to position  $j$ , and place a “-1” in the position if transition  $i$  has output from position  $j$ , and A “0” is placed in the position if position  $i$  does not have input from position  $j$ . In this way,  $M$  is defined as the *Activity-Data Incidence Matrix* of WFIO-net.

According to Definition 5.4, if “1” is placed at position  $[i, j]$ , it represents that the  $i$ th activity writes a data to the  $j$ th data element. Similarly, if “-1” is placed at position  $[i, j]$ , it means that the  $i$ th activity reads a data from the  $j$ th data element. The activity-data incidence matrix of the WFIO-net in Fig. 3 is constructed in the following.

	$p_{d1}$	$p_{d2}$	$p_{d3}$	$p_{d4}$	$p_{d5}$	$p_{d6}$	$p_{d7}$	$p_{d8}$	$p_{d9}$	$p_{d10}$
$t_{A1}$	1	1	1	0	0	0	0	0	0	0
$t_{A2}$	-1	-1	-1	1	0	0	0	0	0	0
$t_{A3}$	0	0	0	0	1	0	0	0	0	0
$t_{A4}$	0	0	0	0	1	0	0	0	0	0
$t_{A5}$	0	0	0	0	1	0	0	0	0	0
$t_{A6}$	0	0	0	0	-1	1	0	0	0	0
$t_{A7}$	0	0	0	0	0	-1	-1	1	0	0
$t_{A8}$	0	0	0	0	0	0	0	-1	1	0
$t_{A9}$	0	0	0	0	0	0	0	0	-1	1

Figure 4 Activity-Data Incidence Matrix of WFIO-net in Figure 3

Here we propose Algorithm 1 to detect dataflow errors, including missing data error, redundant data error and conflicting data error in a WFIO-net based on the activity-data incidence matrix of the WFIO-net.

**Algorithm 1:** Detect Data-flow Errors in a WFIO-net.

INPUT: The activity-data incidence matrix  $M$  of a WFIO-net.

OUTPUT: *MisDataSet*, *RedDataSet* and *ConDataSet*.

Step 1: *MisDataSet*  $\leftarrow \emptyset$ , *RedDataSet*  $\leftarrow \emptyset$ , and *ConDataSet*  $\leftarrow \emptyset$ , *ReadNum*  $\leftarrow 0$  and *WriteNum*  $\leftarrow 0$ ;

```

Step 2: FOR  $j=0$  to  $j=|P_d|-1$  DO
  (1) FOR  $i=0$  to  $|T_a|-1$  DO
    IF  $p_{ij}=1$  THEN
      WriteNum++;
    ELSE IF  $p_{ij}=-1$  THEN
      ReadNum++;
    END IF
  END DO
  (2) IF WriteNum==0 and ReadNum>0 THEN
    MisDataSet ← MisDataSet ∪ { $p_{dj}$ };
  ELSE IF WriteNum>0 and ReadNum==0 THEN
    RedDataSet ← RedDataSet ∪ { $p_{dj}$ };
  ELSE IF WriteNum>1 and ReadNum>0 THEN
    ConDataSet ← ConDataSet ∪ { $p_{dj}$ };
  END IF
  (3) ReadNum ← 0 and WriteNum ← 0;
END DO
Step 3: Output MisDataSet, RedDataSet, and ConDataSet.

```

The complexity of Algorithm 1 is mainly determined by the second step whose complexity is  $O(|P_d| \times |T_a|)$ . Thus, the complexity of Algorithm 1 is  $O(|P_d| \times |T_a|)$ , where  $|P_d|$  is the number of data places and  $|T_a|$  is the number of activities. Take the property loan approval business process in Section 3 as an example. By executing Algorithm 1, we can obtain  $MisDataSet = \{p_{d7}\}$ ,  $RedDataSet = \{p_{d4}, p_{d10}\}$  and  $ConDataSet = \{p_{d5}\}$ .

## 6. CONCLUSIONS

To formulate the data-flow modeling and verification for workflow management, a Petri Net based approach is proposed. The contributions of this work are summarized as follows: (1) to model the data-flow elements of a workflow, we propose the WFIO-net, which is a WF-net by extending each activity with its read and write data sets; and (2) The formal definitions of three basic types of data-flow errors, including missing data, redundant data and conflicting data are given based on WFIO-net and their corresponding detection algorithm is also addressed using the activity-data incidence matrix of WFIO-net. However, this is our first work towards formal modeling and verification of data-flow anomalies. More efforts will be highly desired at least in the following two aspects: (1) Detailed taxonomy of each kind of data-flow error will be discussed. For example, the missing data error may contain several sub-classes such absolute missing and conditional missing as mentioned in [10]; and (2) Time factor will be introduced to our WFIO-net to give a more accurate verification manner, i.e. write operation to one data element is not permitted when it is reading/writing by the other activity.

## 7. ACKNOWLEDGEMENTS

This work was supported in part by NSFC (61170079 and 61202152), by the Special Fund for Agro-scientific Research in the Public Interest (201303107), by the special Fund for Fast Sharing of Science Paper in Net Era by CSTD (2013122), by the Sci. & Tech. Development Fund of Qingdao (13-1-4-153-jch), by the open project of the Key Laboratory of Embedded System and Service Computing, Ministry of Education, Tongji University (ESSCKF201403), the Excellent Young Scientist Foundation of Shandong Province (BS2012DX030 and ZR2013FQ030) and the Graduate Innovation Foundation Project of Shandong University of Science and Technology (YC140106).

## 8. REFERENCES

- [1] W. M. P. van der Aalst, "The application of Petri nets to workflow management," *Journal of Circuits, Systems and Computers*, vol. 8, no. 1, pp. 21–66, 1998.
- [2] W. M. P. van der Aalst, K. M. van Hee, A. H. M. ter Hofstede et al., "Soundness of workflow nets: classification, decidability, and analysis," *Formal Aspects of Computing*, vol. 23, no. 3, pp. 333–363, 2011.
- [3] Jianqiang Li, Yushun Fan, Mengchu Zhou, "Performance modeling and analysis of workflow", *IEEE Transactions on Systems, Man and Cybernetics, Part A: Systems and Humans*, vol.34, no.2, pp. 229- 242, March 2004.
- [4] Jianqiang Li, Yushun Fan, Mengchu Zhou, "Timing Constraint Workflow Nets for Workflow Analysis", *IEEE Transactions on Systems, Man, and Cybernetics-Part A: Systems and Humans*, Vol.33, No.2, March 2003, pp.179-193.
- [5] Huaqing Wang, Qingtian Zeng, "Modeling and Analysis for Workflow Constrained by Resources and Nondetermined Time: An Approach Based on Petri Nets", *IEEE Transactions on Systems, Man and Cybernetics, Part A: Systems and Humans*, vol.38, no.4, pp.802-817, July 2008.
- [6] Qingtian Zeng, Huaqing Wang, Dongming Xu, Hua Duan, Yanbo Han, "Conflict detection and resolution for workflows constrained by resources and non-determined durations", *Journal of Systems and Software*, 819: 1491-1504, 2008.
- [7] Shazia Sadiq, Maria Orlowska, Wasim Sadiq, and Cameron Foulger. 2004. Data flow and validation in workflow modelling. In *Proceedings of the 15th Australasian database conference - Volume 27 (ADC '04)*, Klaus-Dieter Schewe and Hugh Williams (Eds.), Vol. 27. Australian Computer Society, Inc., Darlinghurst, Australia, Australia, 207-214.
- [8] Shaokun Fan, Wanchun Dou, Jinjun Chen. Dual Workflow Nets: Mixed Control/Data-Flow Representation for Workflow Modeling and Verification, *Advances in Web and Network Technologies, and Information Management*, Lecture Notes in Computer Science Volume 4537, 2007, pp 433-444
- [9] Nanshan Du, Yiwen Liang, and Li Zhao. 2008. Data-flow skeleton filled with activities driven workflow design. In *Proceedings of the 2nd international conference on Ubiquitous information management and communication (ICUIMC '08)*. ACM, New York, NY, USA, 570-574.
- [10] Sun, S.X., Zhao, J.L., Nunamaker, J.F., Liu Sheng, O.R.: Formulating the Data Flow Perspective for Business Process Management. *Information Systems Research* 17(4), 374–391 (2006)
- [11] Sundari, M.H., Sen, A.K., Bagchi, A.: Detecting Data Flow Errors in Workflows: A Systematic Graph Traversal Approach. In: 17th Workshop on Information Technology & Systems (WITS 2007), Montreal (2007)
- [12] Cristina Claudia DOLEAN, Razvan PETRUSEL, Data-Flow Modeling: A Survey of Issues and Approaches. December 2012, *Informatica Economica*; 2012, Vol. 16 Issue 4, p117.

- [13] T. Murata, "Petri Nets: Properties, Analysis and Applications," *Proceedings of the IEEE*, vol. 77, no. 4, pp. 541-580, April, 1989.
- [14] W. Reisig, *Understanding Petri Nets: Modeling Techniques, Analysis Methods, Case Studies*, Springer, 2013.
- [15] Cong Liu, Qingtian Zeng, Jie Zou, Faming Lu and Qingxin Wu, "Invariant Decomposition Conditions for Petri Nets Based on the Index of Transitions," *Information Technology Journal*, vol. 11, pp. 768-774, 2012.
- [16] Cong Liu, Qingtian Zeng, Hua Duan, Mengchu Zhou, Faming Lu, and Jiujun Cheng, "E-Net modeling, analysis and resource management for emergency response processes", *IEEE Transaction on System, Man and Cybernetics: Systems*, forthcoming in 2014.
- [17] Jiujun Cheng, Cong Liu, Mengchu Zhou, Qingtian Zeng, and Antti Ylä-Jääski, "Automatic Composition of Semantic Web Services Based on Fuzzy Predicate Petri Nets", *IEEE Transaction on Automation Science and Engineering*, forthcoming in 2014.
- [18] Qingtian Zeng, Faming Lu, Cong Liu, Hua Duan, and Changhong Zhou, "Modeling and Verification for Cross-department Collaborative Medical Business Processes Using Extended Petri Nets", *IEEE Transaction on System, Man and Cybernetics: Systems*, forth coming in 2014.
- [19] Hua Duan, Qingtian Zeng, Huaiqing Wang, Sherry X. Sun, Dongming Xu. Classification and Evaluation of Timed Running Logs of Workflows based on Process Mining, *Journal of Systems and Software*, Volume 82, Issue 3, March 2009, Pages 400-410.
- [20] Sherry X. Sun, Qingtian Zeng, Huaiqing Wang, Process-Mining-Based Workflow Model Fragmentation for Distributed Execution, *IEEE Transactions on Systems, Man and Cybernetics, Part A: Systems and Humans*, March 2011, Volume: 41 Issue:2, On page(s): 294 – 310.
- [21] Qingtian Zeng, Hua Duan. Behavior Description for Complex Flexible Manufacturing System Based on Decomposition of Petri Net, *International Journal of Computer Systems Science and Engineering*, Vol. 22, No.6, pp. 359-363, 2007.
- [22] Qingtian Zeng. Two Symmetrical Decomposition Methods for Structure-complex Petri Net and Their Applications, Eighth ACIS International Conference on Software Engineering, Artificial Intelligence, Networking, and Parallel/Distributed Computing, 2007. SNPD 2007. Volume: 3, On page(s): 1101-1106.
- [23] Qingtian Zeng, Xiaowen Hu, Jun Zhu, Hua Duan. A Polynomial-time Decomposition Algorithm for a Petri Net based on Indexes of Places, *Journal of Applied Science*, Volume: 8, Issue: 24, Pages: 4668-4673, 2008.
- [24] Qingtian Zeng. A Polynomial-time Decomposition Algorithm for a Petri Net based on Indexes of Transitions, *Information Technology Journal*, 10(4):856-862. 2011.
- [25] Qingtian Zeng. A Construction Method for the Process Expression of Petri Net Based on Decomposition, *Information Technology Journal*, Volume 7, Issue 3, Pages 420-429, 2008.
- [26] Rong Hua, You Fu, Jianzhi, CongLiu, "Petri Net-based modeling and verification of automatic train speed control system", *Applied Mechanics and Materials*, 2014, Vols. 571(1):395-399.
- [27] Jun Zhu, Qingtian Zeng. Property analysis of Petri Nets Based on Decomposition according to indexes of Transitions [J]. *Journal of Frontiers of computer science and technology*, 4(08):1673-9418, 2010.
- [28] Zhehui Wu. An introduction to Petri Net [M]. Beijing: Publishing House of China Machine, 2006.
- [29] Qingtian Zeng, Zhehui Wu. Decomposition method of Petri net based on index of places [J]. *Journal of Computer Science*, 29 (4): 15-17, 2002.
- [30] Qingtian Zeng, Faming Lu, Cong Liu, and Decun Meng, "Modeling and Analysis for Cross-organizational Emergency Response Systems, *Journal of Computers in Chinese*, 2013, 36(11): 2290-2302.

# Performance and Emission Characteristics of Zirconia Coating on I.C Engine Using Callophyllum Biodiesel as a Fuel for Varying Injection pressure

Raghavendra P.M  
Department Of Thermal Power  
Engineering  
VTU PG Centre  
Mysore, India

Krishnamurthy K.N  
Department of Thermal Power  
Engineering  
VTU PG Centre  
Mysore, India

Akashdeep B.N  
Department of Mechanical  
Engineering, KSSEM,  
Bangalore, India

---

**Abstract:** In this present world, the realization of the available of fossil fuels [diesel] is limited and hence it is necessary for the efficient use of the fuel. The increasingly environmental regulations also make it necessary to improve the functioning of the diesel engine in terms of their durability and efficiency. Thus, there is a high scope in engine technology to increase the engine ratings and reduce fuel consumption.

For this purpose, the Thermal Barrier Coating (TBC) has been extensively used in engine technology. The T.B.C technology has been applied on some parts of Diesel engine (piston crown and cylinder head) Plasma Spray technique was used for spraying process. The piston crown and Cylinder head of the diesel engine were coated for a thickness of 0.25mm. Callophyllum oil was converted into biodiesel by two stage Transesterification process using NaOH as a catalyst.

Several tests have been carried out to examine properties, performance and emission characteristics for different blends such as [B100, B20, B30, B40 and B100] in comparison with pure diesel for varying injection pressures like 160 bar, 180 bar and 200 bar pressure. These tests were conducted on a single cylinder, 4 stroke, water cooled, direct injection computerized compression ignition engine.

**Keywords:** TBC, Callophyllum oil, Transesterification.

## 1. INTRODUCTION

Thermal barrier coatings (TBC) have been successfully applied to the internal combustion engine, in particular the combustion chamber, to simulate adiabatic engines. The objectives are not only for reduced in-cylinder heat rejection and thermal fatigue protection of underlying metallic surfaces, but also for possible reduction of engine emissions. The application of TBC reduces the heat loss to the engine cooling jacket through the surfaces exposed to the heat transfer such as cylinder head, liner, piston crown and piston rings. The insulation of the combustion chamber with ceramic coating affects the combustion process and hence the performance and exhaust emissions characteristics of the engines.

A typical TBC system consists of (i) the top coat (TC), a porous ceramic layer that acts as the insulator, (ii) the bond coat (BC), an oxidation-resistant metallic layer between the substrate and the TC and (iii) the super alloy or other material substrate that carries the structural load.

The top coat provides thermal insulation for the underlying substrate. The specifications for this coating require a material that combines low thermal conductivity and a coefficient of thermal expansion (CTE) that it is as similar as possible to that of the substrate, so that generation of stresses during

thermal cycling can be minimized. The preferred material for this application is Zirconia.

The bond coat protects the underlying substrate from oxidation and improves adhesion between the ceramic and the metal. Oxidation occurs due to oxygen reaching the bond coat by diffusion through the lattice of the top coat and permeation through the pores.

## 2. THERMAL BARRIER COATING

Thermal barrier coatings (TBC) have been successfully applied to the internal combustion engine, in particular the combustion chamber, to simulate adiabatic engines. The objectives are not only for reduced in-cylinder heat rejection and thermal fatigue protection of underlying metallic surfaces, but also for possible reduction of engine emissions. The application of TBC reduces the heat loss to the engine cooling jacket through the surfaces exposed to the heat transfer such as cylinder head, liner, piston crown and piston rings. The insulation of the combustion chamber with Ytria partially stabilized Zirconia coating affects the combustion process and hence the performance and exhaust emissions characteristics of the engines.

Thermal barrier coatings (TBC) are used to protect substrate materials from high temperatures and oxidation. They are usually ceramic, due to the high oxidation resistance

and low thermal conductivity of this material class a large number of ceramic materials have been tried and are used to some extent. The most widely used material for TBC applications is without doubt Yttria-partially stabilized Zirconia (YSZ), i.e.  $ZrO_2$  doped with 7-8 wt. %  $Y_2O_3$ . There are some ceramics which are used for thermal barrier coating as shown below. [5]

1. Zirconates
2. Yttria Stabilized Zirconia
3. Yttria
4. Alumina
5. Spinel
6. Forsterite.

### 3. PLASMA SPRAY COATING

It is one of the widely used methods for coating of the engine parts. In this method, the surface of the cylinder head and piston crown are insulated by using Yttria Stabilized Zirconia for a thickness of 0.25mm using plasma spray technique.

The surface to be coated such as piston rings, cylinder heads, was first cleaned and degreased with a chemical solvent. A special adhesive bonding material was first coated. The material to be coated Yttria stabilized Zirconia,  $ZrO$  which is in the form of powder was fed to the melting zone. The molten material was further heated to a very high temperature leading to plasma stage. Then the plasma jet was impinged on the surface to be coated, the coating material flattened and sticks to the surface. It becomes very hard surface when it was cooled in inert gas atmosphere and sticks to the surface.



Figure 1: Coated piston crown and Cylinder head



Figure 2: UnCoated piston crown and Cylinder head

## 4. BIODIESEL PRODUCTION

Biodiesel can be produced from straight vegetable oil, animal oil/fats and waste oils. There are three basic routes to biodiesel production from oils and fats:

- Base catalyzed transesterification of the oil.
- Direct acid catalyzed transesterification of the oil.
- Conversion of the oil to its fatty acids and then to biodiesel.

### 4.1 Transesterification Process of Callophyllum oil



Figure 3: Transesterification Set Up

Figure 3 shows the transesterification set up, in which a 2000 ml three necked round bottom flask, was used as a reactor. The flask was placed in heating mantle whose temperature could be controlled within  $\pm 2$  °C. One of the two side necks was equipped with a condenser and the other was used as a thermo well. A thermometer was placed in the thermo well containing little glycerol for temperature measurement inside the reactor. A blade stirrer was passed through the central neck, which was connected to a motor along with speed regulator for adjusting and controlling the stirrer speed. 1000ml of esterified Callophyllum oil was measured and poured into a 2000 ml three necked round bottom flask. This oil was heated upto 600 °C. In 250ml beaker a solution of potassium meth oxide was prepared using 0.5 wt% sodium hydroxide pellets with 1:6 molar ratio of oil to methanol. The solution was properly stirred until the potassium hydroxide pellet was completely dissolved. The solution was then heated upto 60 °C and slowly poured into preheated oil. The mixture was stirred vigorously for one and half hour. Finally FFA was checked and mixture was allowed to settle for 24 hours in a separating funnel. Thereafter, upper layer biodiesel was decanted into a separate beaker while the lower layer which comprised glycerol and soap was collected from the bottom of separating funnel. To remove any excess glycerol and soap from the biodiesel, hot water was used to wash it and then allowed it to remain in separating funnel until clear water was seen below the biodiesel in the separating funnel. The PH of biodiesel was then checked. The washed biodiesel sample was then dried by placing it on a hot plate and excess water still in the biodiesel removed.

Table 1 shows the fuel properties of biodiesel determined as per ASTM standards.

**Table 1: Properties of Callophyllum biodiesel**

Parameter	Callophyllum biodiesel(Methyl Ester)
Density (kg/m <sup>3</sup> )	900
Kinematic viscosity (Cst)	7.1
Flash Point °C	165
Fire Point °C	175
Calorific value (kJ/kg)	36957.2

## 5. ENGINE TEST PROCEDURE

A four stroke, single cylinder water cooled diesel engine is employed for the performance study.

Five gas analyzer was used to measure the concentration of gaseous emissions such as Oxides of nitrogen, unburned hydrocarbon, carbon monoxide, carbon dioxide and oxygen level. The performance and emission tests are carried out on the C.I. engine using various blends of diesel-biodiesel blends as fuels. The tests are conducted at the constant speed of 1500rpm at various torque and at different injection pressure such as at 160 bar, 180 bar and 200 bar for normal standard engine as well as coated engine. In this experiment, engine parameters related to thermal performance of engine such as brake thermal efficiency, brake specific fuel consumption, brake specific energy consumption, exhaust gas temperature are measured. In addition to that the engine emission parameters such as Oxides of nitrogen, unburned hydrocarbon, carbon monoxide, carbon dioxide and oxygen level.



**Figure 4: The photograph of diesel engine with pressure thermocouple for sensing exhaust gas temperature as shown in figure**

## 6. RESULTS AND DISCUSSION

The studies were therefore, conducted on methyl esters transesterification process for Callophyllum biodiesel B100 and blends of different percent volumes of Biodiesel B20, B30, and B40 were carried out. The fuel consumption

test and rating test of a constant speed CI engine was also conducted to evaluate the performance of the engine on diesel and methyl esters of Callophyllum biodiesel B100 and blends of different percent volumes of Biodiesel B20, B30, and B40.

In this chapter the characterization of fuel is analyzed by drawing different graphs, some of the important properties like kinematic viscosity, the density and calorific value of different blends on the addition of biodiesel, was also studied with comparing with the diesel and 100% biodiesels.

Also the engine performance and emission characteristics were also discussed and different Graphs of showing the performance and emission characteristics were drawn and those graphs were analyzed in detailed.

### 6.1 Performance Characteristics

#### 1. Brake Specific Fuel Consumption

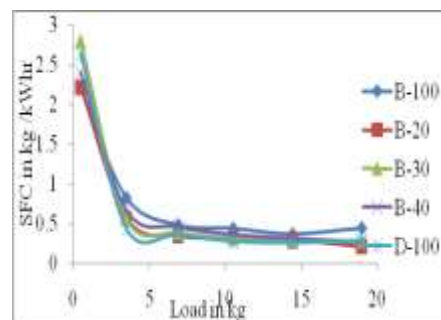


**Figure 5: Variation of Brake Specific Fuel Consumption with Load at 200 bar pressure before coating**

The variation in BSFC with load for different fuels at 200 bar pressure for before coating of the engine is presented in Figure 5 Brake-specific fuel consumption (BSFC) is the ratio between mass fuel consumption and brake effective power, and for a given fuel, it is inversely proportional to thermal efficiency. BSFC decreased sharply with increase in load for all fuels. The main reason for this could be that the percent increase in fuel required to operate the engine is less than the percent increase in brake power, because relatively less portion of the heat is lost at higher loads. The maximum BSFC was found in B30 and it is higher than the diesel. As the BSFC was calculated on a weight basis, higher densities resulted in higher values for BSFC.

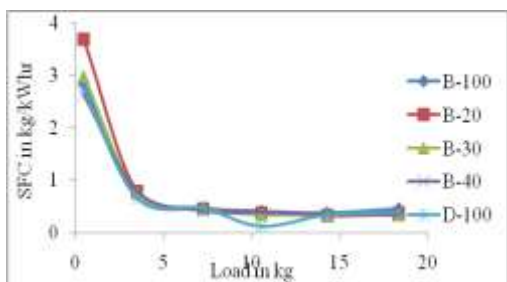


**Figure 6: Variation of Brake Specific Fuel Consumption with Load at 200 bar pressure after coating**

The variation in BSFC with load for different fuels at 200 bar pressure for after coating of the engine is presented in Figure 6. In this graph also BSFC decreased sharply with increase in load for all fuels. The maximum BSFC was found in B20 and it is much higher than the diesel and biodiesel.

2. Brake Specific Fuel Consumption at 180 bar pressure

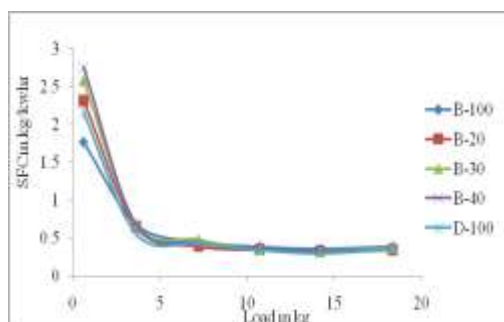


**Figure 7: Variation of Brake Specific Fuel Consumption with Load at 180 bar pressure before coating**

The variation in BSFC with load for different fuels at 180 bar pressure before coating of the engine is presented in Figure 7. In this graph also BSFC decreased sharply with increase in load for all fuels. The maximum BSFC was found in B40 and it is much higher than the diesel and biodiesel.

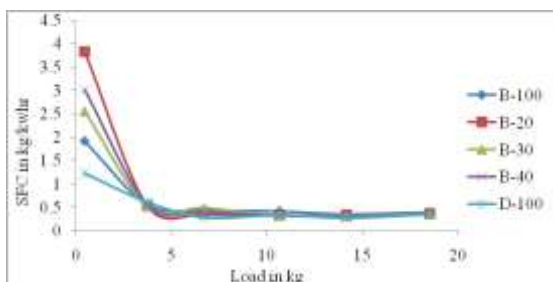


**Figure 8: Variation of Brake Specific Fuel Consumption with Load at 180 bar pressure after coating**

The variation in BSFC with load for different fuels at 180 bar pressure after coating of the engine is presented in Figure 8. In this graph also BSFC decreased sharply with increase in load for all fuels. The maximum BSFC was found in B20 and it is much higher than the diesel and biodiesel.

3. Brake Specific Fuel Consumption at 160 bar pressure

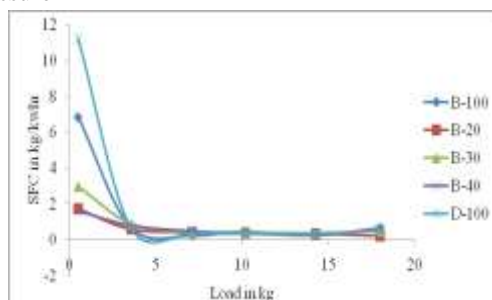


**Figure 9: Variation of Brake Specific Fuel Consumption with Load at 160 bar pressure before coating**

The variation in BSFC with load for different fuels at 160 bar pressure before coating of the engine is presented in Figure 9. In this graph also BSFC decreased sharply with increase in load for all fuels. The maximum BSFC was found in D100 and it is much higher than the biodiesel and blends.

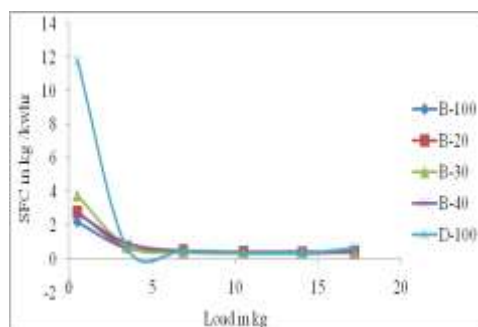


**Figure 10: Variation of Brake Specific Fuel Consumption with Load at 160 bar pressure after coating**

The variation in BSFC with load for different fuels at 160 bar pressure after coating of the engine is presented in Figure 10. In this graph also BSFC decreased sharply with increase in load for all fuels. The maximum BSFC was found in D100 and it is much higher than the biodiesel and blends.

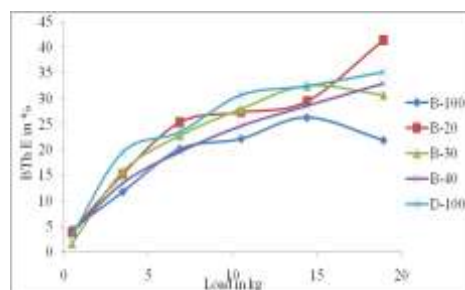


**Figure 11: Variation of brake thermal efficiency with Load at 200 bar pressure before coating**

The variation of brake thermal efficiency with load for different fuels at 200 bar pressure before coating is presented in Fig 11. In all cases, it increased with increase in load. This was due to reduction in heat loss and increase in power with increase in load. The maximum thermal efficiency for B20

was higher than that of diesel. The brake thermal efficiency obtained for B30, B10, and B100 were less than that of diesel. This lower brake thermal efficiency obtained could be due to reduction in calorific value and increase in fuel consumption as compared to B20.

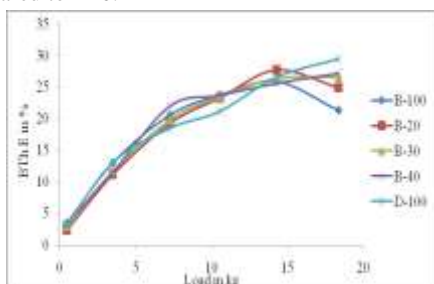


**Figure 12: Variation of brake thermal efficiency with Load at 200 bar pressure after coating**

The variation of brake thermal efficiency with load for different fuels at 200 bar pressure after coating is presented in Fig 12. In all cases, it increased with increase in load. This was due to reduction in heat loss and increase in power with increase in load. The maximum thermal efficiency is for D100 and was higher than that of biodiesel and blends.

2. Brake Thermal Efficiency at 180 bar pressure:

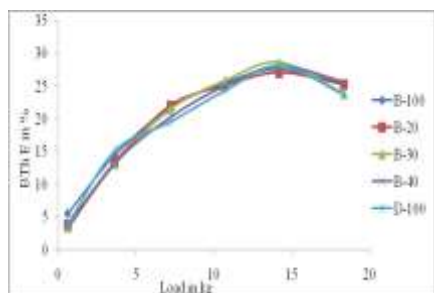


**Figure 13: Variation of brake thermal efficiency with Load at 180 bar pressure before coating**

The variation of brake thermal efficiency with load for different fuels at 180 bar pressure before coating is presented in Fig 13. In all cases, it increased with increase in load, except for B-100 where the break thermal efficiency decreases for maximum load. The maximum thermal efficiency is obtained in B30.

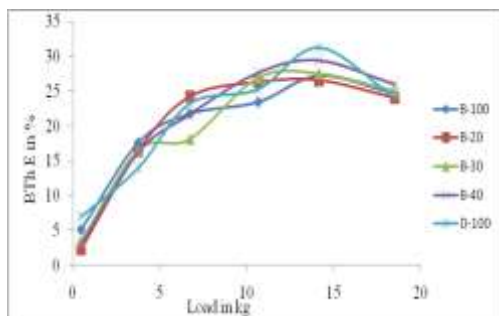


**Figure 14: Variation of brake thermal efficiency with Load at 180 bar pressure after coating**

The variation of brake thermal efficiency with load for different fuels at 180 bar pressure after coating is presented in Fig 14. In all cases, it increased with increase in load, except for B-100 where the break thermal efficiency decreases for maximum load. The maximum thermal efficiency is obtained in B40

3. Brake Thermal Efficiency at 160 bar pressure:

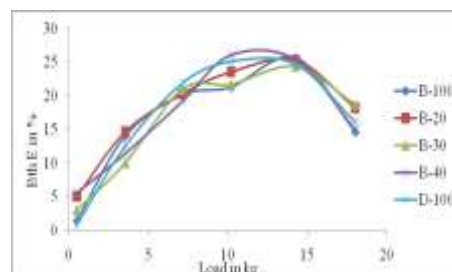


**Figure 15: Variation of brake thermal efficiency with Load at 160 bar pressure before coating**

The variation of brake thermal efficiency with load for different fuels at 160 bar pressure before coating is presented in Fig 15. In all cases, it increased with increase in load, except for B-100 where the break thermal efficiency decreases for maximum load. The maximum thermal efficiency is obtained in B40.

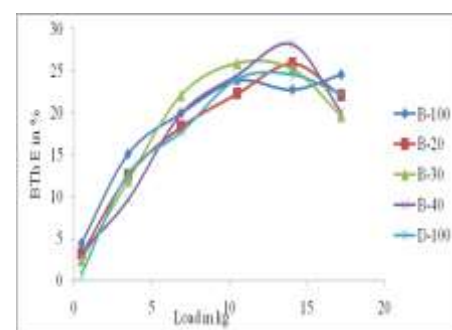


**Figure 16: Variation of brake thermal efficiency with Load at 160 bar pressure after coating**

The variation of brake thermal efficiency with load for different fuels at 160 bar pressure after coating is presented in Fig 16. In all cases, it increased with increase in load, except for B-100 where the break thermal efficiency decreases for maximum load. The maximum thermal efficiency is obtained in B40

1. Brake power at 200 bar pressure:

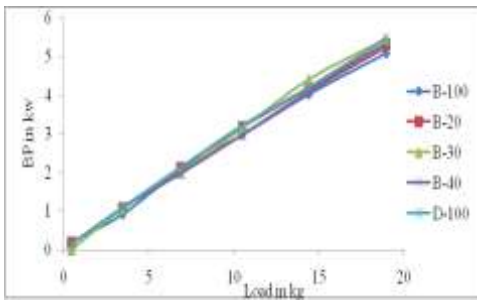


Figure 17: Variation of Brake power with Load at 200 bar pressure before coating

The variation of brake power with load for different fuels at 200 bar pressure before coating is presented in Fig 17. In all cases, it increased with increase in load. The maximum brake power is for D100 at maximum load and was higher than that of Biodiesel. The brake power obtained for B20, B30, B40 and B100 were less than that of diesel

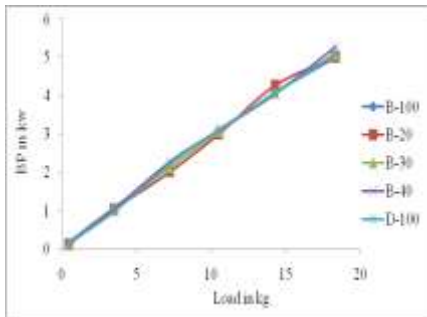


Figure 18: Variation of Brake power with Load at 200 bar pressure after coating

The variation of brake power with load for different fuels at 200 bar pressure after coating is presented in Fig 18. In all cases, it increased with increase in load. The maximum brake power is for B40 at maximum load and was higher than that of diesel. The brake power obtained for B20, B30, B100 and D100 were less than that of B40

2. Brake power at 180 bar pressure

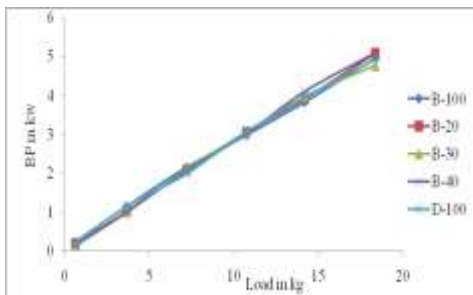


Figure 19: Variation of Brake power with Load at 180 bar pressure before coating

The variation of brake power with load for different fuels at 180 bar pressure before coating is presented in Fig 19. In all cases, it increased with increase in load. The maximum brake power is for B40 at maximum load and was higher than that of diesel. The brake power obtained for B20, B30, B100 and D100 were less than that of B40.

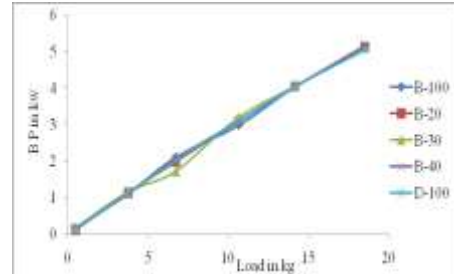


Figure 20: Variation of Brake power with Load at 180 bar pressure after coating

The variation of brake power with load for different fuels at 180 bar pressure after coating is presented in Fig 20. In all cases, it increased with increase in load. The maximum brake power is for B40 at maximum load and was higher than that of diesel. The brake power obtained for B20, B30, B100 and D100 were less than that of B40

3. Brake power at 160 bar pressure:

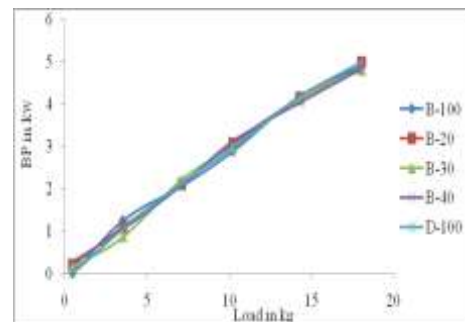
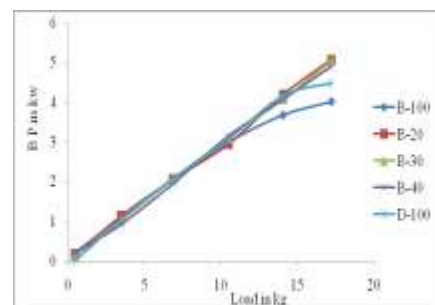


Figure 21: Variation of Brake power with Load at 160 bar pressure before coating

The variation of brake power with load for different fuels at 160 bar pressure before coating is presented in Fig 21. In all cases, it increased with increase in load. The maximum brake power is for D100 at maximum load and was higher than that of Biodiesel. The brake power obtained for B20, B30, B40 and B100 were less than that of diesel



**Figure 22: Variation of Brake power with Load at 160 bar pressure after coating**

The variation of brake power with load for different fuels at 160 bar pressure after coating is presented in Fig 22. In all cases, it increased with increase in load. The maximum brake power is for B20 at maximum load and was higher than that of diesel. The brake power obtained for B30, B40, B100 and D100 were less than that of B20.

## 6.2 Emission characteristics

### 1. Carbon monoxide Emissions at 200 bar pressure:

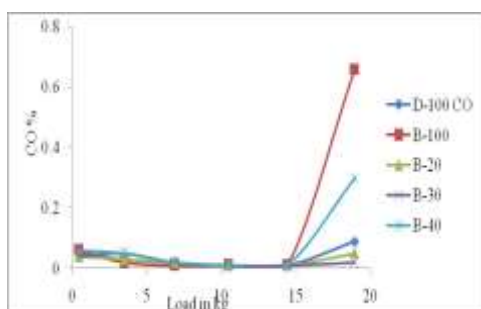


**Figure 23: Variation of CO with Load at 200 bar pressure before coating**

Variation of CO emissions with engine loading for different fuels at 200 bar pressure before coating is compared in Fig 23. The minimum CO produced was found in B30 and it was observed that a reduction of 50%, as compared to diesel. Also it is observed that the CO emissions for diesel and the blends are lower than the biodiesel fuel. These lower CO emissions of diesel and the blends may be due to their more complete oxidation as compared to biodiesel. Some of the CO produced during combustion of biodiesel might have converted into CO<sub>2</sub> by taking up the extra oxygen molecules present in the biodiesel chain and thus reduced CO formation. It can be observed from Fig. that the CO initially decreased with load and later increased sharply up to full load.

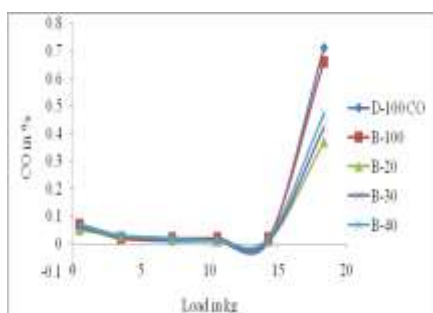


**Figure 24: Variation of CO with Load at 200 bar pressure after coating**

Variation of CO emissions with engine loading for different fuels at 200 bar pressure after coating is compared in Fig 24. The minimum CO produced was found in B20 and it was observed that a reduction of

30%, as compared to diesel. The maximum CO emission was for Diesel. It can be observed from Fig. that the CO initially decreased with load and later increased sharply up to full load.

### 2. Hydro carbon Emissions at 200 bar pressure:

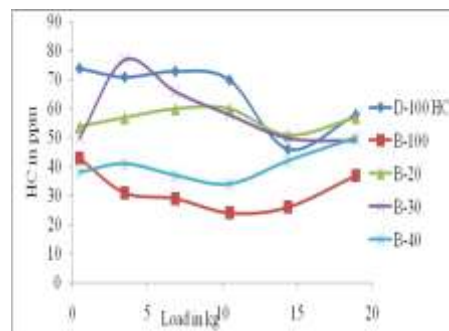


**Figure 25: Variation of Hydro-carbon with Load at 200 bar pressure before coating**

The hydrocarbons (HC) emission trends for blends of methyl esters and oil and diesel at 200 bar pressure before coating are shown in Fig 25. The reduction in HC was linear with the addition of biodiesel for the blends tested. The minimum HC emission was for biodiesel i.e. B100. There is a reduction from 58 ppm to 37 ppm was obtained resulting in B100 and it is 30%, as compared to diesel at the maximum load.

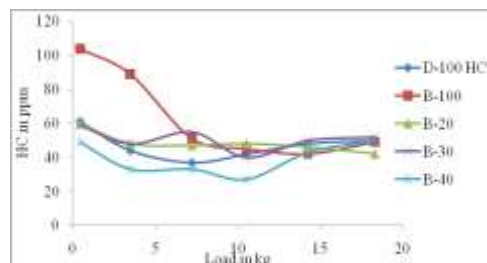


**Figure 26: Variation of Hydro-carbon with Load at 200 bar pressure after coating**

Variation of HC emissions with engine loading for different fuels at 200 bar pressure after coating is compared in Fig 26. From the fig it can be observed that at initial load HC is maximum for biodiesel B100 and as the load is increased the emission reduces drastically. After coating the HC emission of biodiesel and its blends are less when compared to that of diesel

3. Hydro carbon Emissions at 180 bar pressure:

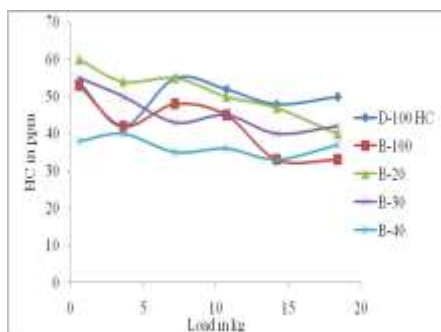


**Figure 27: Variation of Hydro-carbon with Load at 180 bar pressure before and after coating**

The hydrocarbons (HC) emission trends for blends of methyl esters and oil and diesel for 180 bar pressure before coating are shown in Fig 27. The reduction in HC was linear with the addition of biodiesel for the blends tested. The minimum HC emission was for biodiesel i.e B100. There is a reduction from 50 ppm to 33 ppm was obtained resulting in B100 and it is 25%, as compared to diesel at the maximum load.

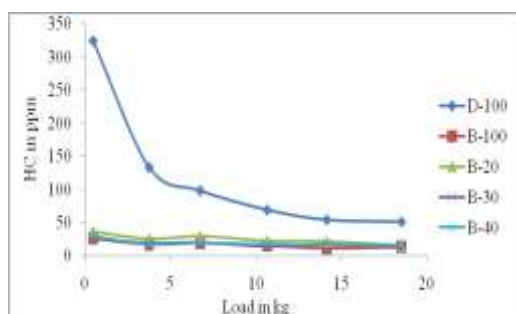


**Figure 28: Variation of Hydro-carbon with Load at 180 bar pressure after coating**

The hydrocarbons (HC) emission trends for blends of methyl esters and oil and diesel at 180 bar pressure after coating are shown in Fig 28. The reduction in HC was linear with the addition of biodiesel for the blends tested. From the fig it can be observed that at initial load HC is maximum for diesel D100 and as the load is increased the emission reduces drastically. After coating the HC emission of biodiesel and its blends are less when compared to that of diesel.

4. Hydro carbon Emissions at 160 bar pressure:

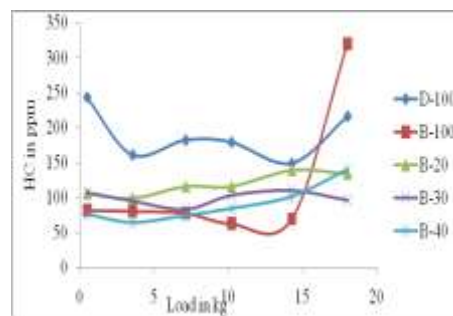


**Figure 29: Variation of Hydro-carbon with Load at 160 bar pressure before coating**

The hydrocarbons (HC) emission trends for blends of methyl esters and oil and diesel at 160 bar pressure before coating is shown in Fig 29. The reduction in HC was linear with the addition of biodiesel for the blends tested. The minimum HC emission was for biodiesel i.e B30. The HC emission for diesel and biodiesel is much higher than the blends of biodiesel.

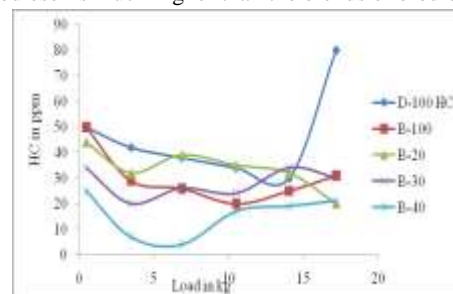


**Figure 30: Variation of Hydro-carbon with Load at 160 bar pressure after coating**

The hydrocarbons (HC) emission trends for blends of methyl esters and oil and diesel at 160 bar pressure for after coating are shown in Fig 30. The reduction in HC was linear with the addition of biodiesel for the blends tested. From the fig it can be observed that at initial load HC is maximum for diesel D100 and as the load is increased the emission reduces drastically. After coating the HC emission of biodiesel and its blends are less when compared to that of diesel.

**7. CONCLUSIONS**

1. The production of Callophyllum biodiesel is obtained by two stage transesterification process using NaOH as a catalyst.
2. The Performance and Emission test was carried out for different pressures [160 bar, 180 bar and 200 bar pressures]
3. The C.V of biodiesel (B100) was found to be 36957 kJ/kg and C.V of different blends were also determined according to ASTM standards .The C.V of blends was found to be less than the diesel (42500 kJ/kg)
4. From the experimental investigation the C.V, Viscosity, and Density of B20 is 41,391kJ/kg, 3.1 Cst and 852 kg/m<sup>3</sup> respectively which is approximately same when compared to diesel.

5. From the experimental study, the result shows that Brake Thermal Efficiency for B20 is 41.33% and for diesel 35.21%. There is an increase in 6.12% of Brake Thermal efficiency at 200 bar pressure for uncoated engine when compared to diesel.
6. For coated engine, at 180 bar pressure for B40 blend the B.S.F.C decreases by 0.08 kg/kWhr and B.P increases by 0.2 kW with respect to diesel. So, the performance of engine increases for coated engine when compared to uncoated engine.
7. From the emission characteristics graphs, it can be seen that there is a decrease in CO and HC emission for 200 bar pressure after coating. The CO emission of B100 is reduced by 2 % when compared to diesel and HC emission is reduced partially from 45 ppm to 50 ppm.
8. At 180 bar pressure HC emission of B100 reduces considerably for both before and after coating of the engine. Before coating, B100 emits 33 ppm NO<sub>x</sub> emission and diesel 50 ppm. After coating, B100 13 ppm and diesel 51 ppm.
9. The CO<sub>2</sub> emission of biodiesel and its blends are much higher than that of diesel for all injection pressure.
10. The performance and emission characteristics of 160 bar pressure are determined. The results obtained are not to the standard values with respect to diesel because the fuel atomization is incomplete due to which incomplete combustion of fuel takes place.
11. From the obtained results, we can conclude that the blend B40 at 180 bar pressure has better performance and Emission characteristics when compared to all other blends with respect to diesel for all varying pressures for TBC engine.

International Journal of Research in Engineering and Technology, 2013.

- [7] Vinay Kumar Domakonda and Ravi Kumar Puli - *Application of Thermal Barrier Coatings in Diesel Engines: a Review* Energy and power, vol. 2(1), 2012
- [8] Palaniswamy E and Manoharan N - *Ceramic Coated Combustion Chamber for Improving IC Engine Performance*, International journal on design and Manufacturing Technologies, vol 2(1), 2008.
- [9] Willard W. Pulkrabek - *Engineering Fundamentals of the Internal Combustion Engine*
- [10] P.N.Shrirao and A.N.Pawar - *Evaluation of Performance and Emission characteristics of Turbocharged Diesel Engine with Yttria as Thermal Barrier Coating*, International Journal of Engineering and Technology, vol 3(3), 2011.

## 8. REFERENCES

- [1] Murat Ciniviz, et.al - *Ceramic Coating Applications and Research Fields for Internal Combustion Engines* – 2012.
- [2] Karuppasamy, et.al – *The Effect of Thermal Barrier Coatings on Diesel Engine Performance*, ARPJN journal of science and Technology, vol 3, 2013.
- [3] Chavan S.B, et.al – *Callophyllum Inophyllum Linn (“honne”) Oil, A Source for Biodiesel production*, Research journal of chemical sciences, vol 3(11), 2013.
- [4] Daniel Eriksson - *Advanced Thermal Barrier Coatings of Yttria-Partially Stabilized Zirconia*, Karlstad University.
- [5] Ilker Turgut Yilmaz, et.al - *Thermal Barrier Coatings for Diesel Engines*, International Scientific Conference, 2010
- [6] J.Rajasekaran, et.al – *Effect of Thermal Barrier Coating for the improvement of SI engine performance & Emission characteristics*, IJRET –